

# **On the use of Layered Double Hydroxides on Lithium and Post-lithium Batteries**

Zur Erlangung des akademischen Grades eines  
DOKTORS DER NATURWISSENSCHAFTEN

(Dr. rer. nat.)

von der KIT-Fakultät für Chemie und Biowissenschaften des  
Karlsruher Instituts für Technologie (KIT)

angenommene

DISSERTATION

von

M. Sc. Xinyue Li

aus Hunan, China

Referent: Prof. Dr. rer. nat. Helmut Ehrenberg

Korreferent: T.T.-Prof. Dr.-Ing. Helge S. Stein

Tag der mündlichen Prüfung: 12.12.2022







## **Selbständigkeitserklärung**

Hiermit versichere ich, dass ich die vorliegende Arbeit selbstständig verfasst habe, dass ich keine anderen als die angegebenen Quellen und Hilfsmittel benutzt habe, dass ich die wörtlich oder inhaltlich übernommenen Stellen als solche gekennzeichnet habe und dass ich die Satzung des KIT zur Sicherung guter wissenschaftlicher Praxis in der jeweils gültigen Fassung beachtet habe.

Karlsruhe, den 02.11.2022

Xinyue Li



## Acknowledgments

It was since 10/2019 when I officially started my PhD work in the Institute for Applied Materials–Energy Storage Systems (IAM-ESS) at Karlsruhe Institute of Technology. Three years of rich experience brought me from a freshman in science to the full stop of PhD journey. Without those people who kept offering help and conduct, I wouldn't reach where I am.

Firstly, it is my great honor to work in a highly scientific environment at the IAM-ESS where I carried out my doctoral thesis in an exciting field of materials for applications in energy storage.

My grateful acknowledgment would be made to my supervisor and referee, Prof. Dr. rer. nat. Helmut Ehrenberg, who offered me a chance to work in his group and gave me considerable help with suggestions, comments, and invaluable guidance throughout my PhD study. I would also like to thank T.T. Prof. Dr.–Ing. Helge Sören Stein for his warm willingness to be my second supervisor.

I want to express my sincere and profound thanks to my group leader Dr. Sonia Dsoke, for guiding me to gain insights and learn rich scientific knowledge. She keeps shaping a role model to me as a disciplined female scientist. These invaluable influences from her will continue to serve me as a reference for the time to come.

I sincerely appreciate the cooperation in the research project with Dr. Anna Maria Cardinale from the University of Genoa. During my abroad research stay at the University of Genoa, Anna offered me her enthusiastic guidance and abundant technical discussions and a tremendous help to my stay in Italy. She and her group kindly supported me with the materials synthesis in the present work and helped me gain knowledge of synthesis methods. I want to thank my colleague Marco Fortunato from Dr. Anna Maria Cardinale's group at the University of Genoa for his patient help with my materials synthesis experiment and insightful discussion on our projects.

I am grateful to Dr. Angelina Sarapulova, who contributed constructive suggestions, and feedback on my XRD and XAS experiments, and for her incredible patience and thoughtful discussion of my thesis. I would also like to thank Dr. Qiang Fu, who generously took the time to help me with general lab work and advise me on my thesis writing with high-skilled scientific suggestions.

I want to thank Dr. Christian Njel for his support on XPS measurements and thoughtful suggestions from our many discussions. I also want to thank Dr. Björn Schwarz for helping with

magnetic measurement. In addition, I want to express my thank to my previous master student Ms. Camilla Rieker, M.Sc, and bachelor student, Mr. Kevin Xia, B. Sc, for the excellent work they contributed to this thesis.

My gratitude goes out to Mr. Eugen Zemlyanushin, M.Sc, for his exhaustive review and suggestions on my thesis and German correction. My respect also gives to him for showing his high discipline and responsibility for lab and equipment supporting in highly experienced skills. My sincere thank also goes to our previous technician Mr. Julian Hansen, Julian shows extraordinary patience and professionalism in offering lab support.

I appreciate all the previous and present members of the IAM-ESS group for their support and help. It was a great pleasure to work with them. In particular, Ms. Jiali Peng, M. Sc, Dr. Tianzhu Liu, Dr. Marina Bauer (TGA), Mrs. Almut Kriese (administrative support), Mrs. Liuda Mereacre (FT-IR), Mr. Udo Geckle (SEM), M. Sc Fatemehsadat Rahide (SEM, electrolyte measurements), Mrs. Bettina Hunzinger (technique support), Dr. Oleksandr Dolotko (XRD), T.T-Prof. Dr. Julia Maibach (XPS), Dr. Xianlin Luo (XPS), Mr. Heinz-Robert Goebel (equipment support), and Mr. Luis Martin Sanchez Neudeck (IT support). Additionally, the kind help from my colleagues from campus south at IAM-ESS, Dr. Noha Sabi, Mrs. Mahla Talari, M.Sc, Mr. Kun Tang, M.Sc, are highly appreciated. In addition, I acknowledge the beamline scientists Edmund Welter and Morgane Desmau from beamline P65, DESY (Hamburg, Germany), for providing the experimental facilities and giving instructions. I thank the financial support from the China Scholarship Council (CSC No. 201807565019, [2018] 3101).

Lastly, my special and deep appreciation to the best friend in my life, Mr. Meng Li, M.Sc. Without his inexhaustible encouragement, solid support and wise enlightenment, I would not philosophize those up and down moments during my PhD life. My most profound gratitude and love go to my selfless parents and my brother Mr. Zhizhang Li, M.Sc, for their unconditional support and endless love. With them, my existence is valuable.

I would like to draw a full stop to my PhD journey with a Chinese philosophic motto from Confucius,

朝闻道，夕死可矣。

“If one is able to attain the TRUTH at sunrise, one could die at sunset without regrets.”



## Abbreviations

[BMIM][BF <sub>4</sub> ]	1-butyl-3-methylimidazolium tetrafluoroborate
[OMIM][Cl]	1-methyl-3-octyl imidazolium chloride
BE	Binding energy
BiOCl	Bismuth oxychloride
Bpy <sub>14</sub> Cl	Butyl-1-methylpyrrolidinium chloride
CB	Carbon black
Cc	cobaltocene
CE	Counter electrode
CIBs	Chloride-ion batteries
CV	Cyclic voltammetry
DIBs	Dual-ion batteries
DMC	Dimethyl carbonate
DME	Dimethoxyethane
EC	Ethylene carbonate
ESW	Electrochemical stability window
FC	Field-cooled
FeOCl	Iron oxychloride
FE-SEM	Field emission scanning electron microscope
FT-IR	Fourier-transform infrared spectroscopy
GCD	Galvanostatic charge-discharge
ICE	Initial Coulombic efficiency

IL	Ionic liquid
LDHs	Layered double hydroxides
LED	Light-emitting diode
LIBs	Lithium-ion batteries
LiTFSI	Lithium bis(trifluoromethane sulfonyl) imide
LSV	Linear sweep voltammetry
LTO	Lithium titanium oxide, $\text{Li}_4\text{Ti}_5\text{O}_{12}$
$\text{M}_a\text{X}_b$	Transition metal compounds
MCl	Metal chlorides
$\text{N}_{1114}\text{TFSI}$	Butyltrimethylammoniumbis(trifluoromethylsulfonyl)imide
$\text{N}_{116(14)}\text{Cl}$	Benzyltrimethyltetradecylammonium chloride
NiAl LDH	Nickel aluminum layered double hydroxide
NMP	N-methyl pyrrolidone
PANI	Polyaniline
PC	Propylene carbonate
PP	Polypropylene (membrane)
PPMS	Physical Property Measurement System
PPy	Polypyrrole
PVDF	Polyvinylidene fluoride
QRE	Quasi reference electrode
RE	Reference electrode
ROLi	Lithium alkylates

## Abbreviations

SA	Sodium alginate
SEI	Solid-electrolyte interphase
SEM	Scanning electron microscopy
SHE	Standard hydrogen electrode
SS	Stainless steel
TGA	Thermogravimetric analysis
WE	Working electrode
XAS	X-ray absorption spectroscopy
XPS	X-ray photoelectron spectroscopy
XRD	X-ray diffraction
ZFC	Zero-field cooled



## Figures

- Figure 2.1.** Schema of a rechargeable LIB. Lithium ions flow to the positive electrode through the electrolyte, and electrons flow from the external circuit during the discharge process. The flow directions are reversed during charging process. .... 14
- Figure 2.2.** Representative crystal structures of positive electrode materials for LIBs: (a) layered  $\text{LiCoO}_2$ , (b) spinel-structured LMO, and (c) olivine-structured  $\text{LiFePO}_4$ . Copyright of The Royal Society of Chemistry 2014 [51]. .... 16
- Figure 2.3.** Negative electrode design for LIBs. Copyright from Journal of Energy Chemistry 2015 [57]. .... 17
- Figure 2.4.** Negative electrode materials categories based on different reaction mechanisms for LIBs. Black circles: voids in the crystal structure, blue circles: metal, yellow circles: lithium. Reproduced with permission. Copyright from Royal Society of Chemistry 2009 [58]. .... 18
- Figure 2.5.** Unit cells of the a)  $\text{Li}_4\text{Ti}_5\text{O}_{12}$  and b)  $\text{Li}_7\text{Ti}_5\text{O}_{12}$ . During the phase transition, the Li-ions are transferred among the tetrahedral 8a sites (spinel  $[\text{Li}_3]^{8a}[\text{Li}_1\text{Ti}_5]^{16d}[\text{O}_{12}]^{32e}$ ) and the octahedral 16c sites (rock-salt  $[\text{Li}_6]^{16c}[\text{Li}_1\text{Ti}_5]^{16d}[\text{O}_{12}]^{32e}$ ). Constructed by Vesta software. .... 19
- Figure 2.6.** Schematic illustration of the local chemistry transformation during the conversion reaction, transition-metal compounds as an example. Copyright from Chem 2018 [73]. .... 21
- Figure 2.7.** Schematic diagram of the working mechanism of a DIB. .... 23
- Figure 2.8.** Working principle of a CIB. .... 26
- Figure 2.9.** The structure of nitrate-intercalated LDHs with the metal hydroxide octahedra stacked along the crystallographic *c*-axis. .... 31
- Figure 4.1.** a) Crystal structure of NiAl LDH (one unit cell, constructed by Vesta software) and b) Observed and calculated diffraction patterns after Rietveld refinement of the hydrotalcite structure model. .... 44
- Figure 4.2** FE-SEM micrographs of NiAl LDH. a) overview; b) low magnification image; c) and d) high magnification images. .... 46

**Figure 4.3.** XPS spectra: a) survey of NiAl LDH; b) Ni2p<sub>3/2</sub>; c) Al2s, d) O1s; e) N1s and f) C1s. .... 47

**Figure 4.4.** Electrochemical characterization of NiAl LDH based on different binders at the potential window of 0.01-3.0 V *vs.* Li<sup>+</sup>/Li. a) CV curves at 0.1 mV s<sup>-1</sup> on the NiAl LDH-SA electrode; b) GCD profiles at 0.05 A g<sup>-1</sup> of NiAl LDH-SA electrode; c) CV curves at 0.1 mV s<sup>-1</sup> on the NiAl LDH-PVDF electrode; d) GCD profiles at 0.05 A g<sup>-1</sup> of the NiAl LDH-PVDF electrode..... 48

**Figure 4.5.** Electrochemical performance of NiAl LDH with different binders at a potential window of 0.01–3.0 V for a) rate performance, and b) cycle performance and Coulombic efficiency at a current density of 0.5 A g<sup>-1</sup>..... 50

**Figure 4.6.** a) C1s, b) O1s, c) F1s and d) P2p X-ray photoelectron spectra of NiAl LDH-PVDF electrode discharged to 0.59 V, 0.22 V and charged to 3.0 V (1 cycle) respectively; e) C1s, f) O1s, g) F1s and h) P2p XPS spectra of NiAl LDH-SA electrode discharged to 0.65 V, 0.34 V and charged to 3.0 V (1 cycle), respectively. .... 52

**Figure 4.7.** Electrochemical performance of NiAl LDH with different binders in the potential range of 0.4-3.0 V (*vs.* Li<sup>+</sup>/Li). a) CV curves at a scan rate of 0.1 mV s<sup>-1</sup> for NiAl LDH-SA electrode; b) GCD curves at a current density of 0.05 A g<sup>-1</sup> for NiAl LDH-SA electrode; c) CV curves at a scan rate of 0.1 mV s<sup>-1</sup> for NiAl LDH-PVDF electrode and, d) GCD curves at a current density of 0.05 A g<sup>-1</sup> for NiAl LDH-PVDF electrode..... 55

**Figure 4.8.** Electrochemical performance with different binders in the potential range of 0.4-3.0 V (*vs.* Li<sup>+</sup>/Li). a) rate capacity at different current densities of SA and PVDF-based electrodes and; b) cycle performance and Coulombic efficiency at a current density of 0.5 A g<sup>-1</sup> of NiAl LDH-SA and NiAl LDH-PVDF electrodes..... 56

**Figure 4.9.** a) Normalized XANES spectra at Ni K-edge and, b) Fourier transform of the recorded EXAFS-spectra collected on *ex-situ* samples. .... 58

**Figure 5.1.** CV curves at 0.1 mV s<sup>-1</sup> and GCD curves at the current density of 20 mA g<sup>-1</sup> in 1.0 M LiTFSI/LiNO<sub>3</sub> electrolyte of NiAl LDH electrode at different potential windows of 0.7–4.0 V (a, b), 0.7-3.0 V (c, d), and 0.7-4.5 V (e, f) (*vs.* Li<sup>+</sup>/Li). .... 62

**Figure 5.2.** CV curves at  $0.1 \text{ mV s}^{-1}$  and GCD profiles at the current density of  $20 \text{ mA g}^{-1}$  of NiAl LDH electrodes in  $\text{LiNO}_3$ -free LiTFSI electrolyte at different potential windows of: (a and b) 0.7–4.0 V (*vs.*  $\text{Li}^+/\text{Li}$ ) and, (c and d) at 0.7-3.0 V (*vs.*  $\text{Li}^+/\text{Li}$ ). ..... 65

**Figure 5.3.** *Ex-situ* FT-IR spectra of NiAl LDH electrodes: a) in LiTFSI electrolyte, and b) in LiTFSI/ $\text{LiNO}_3$  electrolyte during the first discharge-charge cycle..... 67

**Figure 5.4.** EDX images of NiAl LDH electrodes in LiTFSI/ $\text{LiNO}_3$  electrolyte: a) pristine electrode, b) after discharging to 0.7 V, and c) after charging to 4.0 V. .... 69

**Figure 5.5.** NiAl LDH electrode in different electrolytes at 0.7–4.0 V (*vs.*  $\text{Li}^+/\text{Li}$ ) for a) rate performance at different current densities, and b) cycling stability at a current density of  $0.05 \text{ A g}^{-1}$ ..... 70

**Figure 5.6.** *Ex-situ* (a) C1s and (b) N1s XPS spectra conducted in LiTFSI/ $\text{LiNO}_3$  electrolyte of NiAl LDH electrodes of pristine, discharged to 0.7 V, charged to 3.0 V, and charged to 4.0 V (*vs.*  $\text{Li}^+/\text{Li}$ ) on the first cycle, respectively. .... 71

**Figure 5.7.** *In-situ* normalized XANES spectra at Ni K-edge and Fourier transform of the recorded EXAFS spectra of the discharge process (a) and (b) and, the charging process (c) and (d)..... 74

**Figure 5.8** The schema illustrates the working mechanism of the NiAl LDH electrode with  $\text{Li}^+/\text{NO}_3^-$  shuttle in the LiTFSI/ $\text{LiNO}_3$  electrolyte during the first cycle: a) first discharging process (OCV-discharge plateau), b) first discharging process (discharge plateau-0.7 V), c) first charging process (0.7-charging plateau and, d) first charging process (charge plateau-4.0 V)..... 76

**Figure 6.1.** CV curves in 0.5 M  $\text{Bpy}_{14}\text{Cl}/\text{PC}$  with 0.02 M  $\text{Cc}^+$  at  $10 \text{ mV s}^{-1}$ : a). *vs.* Li QRE, b) *vs.* Ag QRE, and c) evolutions of  $\phi_{\text{Cc}/\text{Cc}^+}$  *vs.* two QREs measured *vs.* time..... 78

**Figure 6.2** CV curves of NiAl LDH electrode in 0.5 M  $\text{Bpy}_{14}\text{Cl}/\text{PC}$  electrolyte: a) at  $0.02 \text{ mV s}^{-1}$  and, (b) at different scan rates of 0.02, 0.1, 0.5 and  $1.0 \text{ mV s}^{-1}$  for the first cycle within 1.0-3.0 V (*vs.* Li). ..... 81

**Figure 6.3** a) Galvanostatic charge-discharge curves; and b) cycling performance of NiAl LDH electrode in  $\text{Bpy}_{14}\text{Cl}/\text{PC}$  electrolyte within 1.0–3.0 V (*vs.* Li) at  $10 \text{ mA g}^{-1}$ . ..... 82

**Figure 6.4.** SEM (a,b) and EDX mapping (c) of the pristine NiAl LDH electrode. .... 83

**Figure 6.5.** SEM and EDX mapping of NiAl LDH electrode: (a) discharged to 1.0 V (vs. Li); and (b) charged to 3.0 V (vs. Li)..... 84

**Figure 6.6.** *Ex-situ* FT-IR of the NiAl LDH electrode for pristine, discharged to 1.2 V, discharged to 1.0 V, and charged to 3.0 V vs. Li, respectively..... 85

**Figure 6.7.** XPS spectra of: a) N1s and b) Cl2p for pristine and soaked NiAl LDH electrodes.. 86

**Figure 6.8.** *Ex-situ* XPS spectra of (a) C1s, (b) N1s, (c) Cl2p, (d) F1s and (e) Li1s of the NiAl LDH electrodes after the discharge and charge process at 10 mA g<sup>-1</sup> within 1.0–3.0 V (vs. Li). 88

## Appendix

<b>Figure A 1.</b> a) FT IR spectra, and b) the thermogravimetric curve of NiAl LDH with NO <sub>3</sub> <sup>-</sup> as the interlayer. ....	105
<b>Figure A 2.</b> Nitrogen adsorption and desorption isotherms of NiAl LDH. ....	105
<b>Figure A 3.</b> Long cycling performance of NiAl LDH electrode with SA and PVDF binders at a potential window of 0.01–3.0 V ( <i>vs.</i> Li <sup>+</sup> /Li) at a current density of 1.0 A g <sup>-1</sup> .....	106
<b>Figure A 4.</b> Amount variation of fluorine from LiF and oxygen from oxidized lithium (ROLi, LiOH and Li <sub>2</sub> O) species on the electrode with a) PVDF binder, and b) SA binder. ....	109
<b>Figure A 5.</b> Comparison of two potential ranges for NiAl LDH-SA and NiAl LDH-PVDF electrodes. ....	110
<b>Figure A 6.</b> Kinetic investigation of the NiAl LDH electrode at a potential window of 0.4–3.0 V ( <i>vs.</i> Li <sup>+</sup> /Li). CV curves at various scan rates of that a) with SA binder, and b) with PVDF binder; <i>b</i> -value determined by the slopes of the logarithm relationship of scan rates and peak current for the electrode c) with SA binder, and d) with PVDF binder.....	111
<b>Figure A 7.</b> Magnetic measurement. a). ZFC/FC susceptibility <i>vs.</i> temperature curves for Ni <sub>0.66</sub> Al <sub>0.33</sub> (OH) <sub>2</sub> (NO <sub>3</sub> ) <sub>0.33</sub> ·0.16 H <sub>2</sub> O obtained at a field of 500 Oe, and the inserted fit: with the Curie constant <i>C</i> , temperature <i>T</i> and Curie-Weiss temperature. b). Inverse susceptibility <i>vs.</i> temperature curve as derived from the FC susceptibility curve. The solid line shows the Curie-Weiss fit from 200 to 300 K and its extrapolation (dashed line). c). Magnetic moment <i>vs.</i> magnetic field for various temperatures. The saturation magnetization as predicted from the Curie-Weiss fit is almost reached at 2 K and 7 T.....	112
<b>Figure A 8.</b> Electrochemical stability of the LiTFSI/LiNO <sub>3</sub> electrolyte on CV curves at 1.0 mV s <sup>-1</sup> at different potential windows ( <i>vs.</i> Li).....	112
<b>Figure A 9.</b> SEM images of NiAl LDH electrodes in LiTFSI/LiNO <sub>3</sub> electrolyte: a) pristine electrode, b) discharge to 0.7 V and, c) charge to 4.0 V.....	113
<b>Figure A 10</b> The concentration of compositions during the discharge-charge process of the NiAl LDH electrodes: a) carbon, b) nitrogen. ....	113

- Figure A 11** *In-situ* normalized XANES spectra at Ni K-edge and Fourier transform of the recorded EXAFS spectra of the discharge process of NiAl LDH on LP30 at a potential window of 0.01-3.0 V (vs. Li<sup>+</sup>/Li)..... 114
- Figure A 12.** The electrochemical stability window of different cell configurations based on Ag QRE in glass cell..... 114
- Figure A 13.** XPS survey of the NiAl LDH electrode and the electrode soaked in Bpy<sub>14</sub>Cl/PC electrolyte..... 115

## Table

**Table 2.1** Battery components and main research results on CIBs..... 27

**Table A 1.** Binding energies (BE) and atomic concentrations (at%) of the different chemical environments identified by XPS at the surface of the NiAl LDH-PVDF electrode cycled for the full cycle (only P2p<sub>3/2</sub> binding energies are specified). ..... 107

**Table A 2.** Binding energies (BE) and atomic concentrations (at%) of the different chemical environments identified by XPS at the surface of the NiAl LDH-SA electrode cycled until the full cycle (only P2p<sub>3/2</sub> binding energies are specified)..... 108





## Abstract

Realizing a future based on safe, clean, sustainable, and economically viable energy technologies is one of modern society's grand challenges. As one alternative energy conversion strategy, electrochemical energy storage technology underpins the potential success of diverting energy sources away from fossil fuels. The application of lithium-ion batteries (LIBs) has seen an increasing expansion in recent years. Graphite is the most conventional LIBs negative electrode material; however, its low specific energy calls for more exploration of alternatives. In addition to developing electrode materials for LIBs with high energy density, investigations on post-lithium ion batteries, such as dual-ion batteries (DIBs) and chloride-ion batteries (CIBs), are also drawing research attention.

Layered double hydroxides (LDHs), with a typical expression of  $[M1_{1-x}M2_x(OH)_2]^{x+}(A^{n-})_{x/n} \cdot mH_2O$ , are structurally constituted by hydrotalcite-like host layers that consist of divalent (M1) and trivalent (M2) metal cations, and charge-balancing interlayer anions ( $A^{n-}$ ) with water molecules. Because of their large interlayer space, the abundance of anions choices, rich combinations of metal ions and low cost, LDHs emerged as prominent electrode alternatives in the energy storage field. This thesis systematically focuses on the study of NiAl LDH material applied as electrode material on LIBs, DIBs, and CIBs from electrochemical performance investigation to mechanism elucidation.

These three main topics, objects of this thesis, are summarized below:

(I) NiAl LDH on LIBs (**Chapter 4**): NiAl LDH with nitrate as its interlayer is investigated as a negative electrode material for LIB. The effect of the potential range (*i.e.*, 0.01–3.0 V and 0.4–3.0 V *vs.* Li<sup>+</sup>/Li) and the influence of the binder on the performance of the material is investigated in 1.0 M LiPF<sub>6</sub> in EC/DMC electrolyte. The NiAl LDH electrode based on sodium alginate (SA) binder shows a high initial discharge capacity of 2586 mAh g<sup>-1</sup> at 0.05 A g<sup>-1</sup> and good stability in the potential range of 0.01–3.0 V (*vs.* Li<sup>+</sup>/Li), which is better than what obtained with a polyvinylidene fluoride (PVDF) binder-based electrode. The NiAl LDH electrode with SA binder shows a retention of 27.6% with a capacity of 388 mAh g<sup>-1</sup> after 1400 cycles at a high current density of 1.0 A g<sup>-1</sup>. Under the same conditions, the PVDF-based electrode shows a retention of 8.5% with a capacity of 121 mAh g<sup>-1</sup>. *Ex-situ* X-ray photoelectron spectroscopy (XPS) and *ex-situ* X-ray

absorption spectroscopy (XAS) reveal a conversion reaction mechanism during  $\text{Li}^+$  insertion into the NiAl LDH material at the potential window of 0.01-3.0 V (*vs.*  $\text{Li}^+/\text{Li}$ ). XAS and XPS have been combined with the electrochemical study to understand the effect of different cut-off potentials on the Li-ion storage mechanism.

(II) NiAl LDH on DIBs (**Chapter 5**): Herein, a novel DIB is designed by a multi-ion intercalation strategy, in which the NiAl LDH is used as a positive electrode in a formulated electrolyte based on 1.0 M LiTFSI/LiNO<sub>3</sub> bisalt. The NiAl LDH positive electrode delivers a maximum discharge capacity of 589 mAh g<sup>-1</sup> (at 20 mA g<sup>-1</sup>) with a capacity retention of 26.0% after 100 cycles (at 50 mA g<sup>-1</sup>) at a broad potential window of 0.7-4.0 V (*vs.*  $\text{Li}^+/\text{Li}$ ). *Ex-situ* Fourier-transform infrared spectroscopy (FT-IR) and *ex-situ* XPS measurements disclose the  $\text{Li}^+/\text{NO}_3^-$  multi-ion shuttle chemistry of the NiAl LDH electrode on DIB, that is, based on the simultaneous de-intercalation of  $\text{NO}_3^-$  with the intercalation of  $\text{Li}^+$  from/into the LDH structure during discharging (de-intercalation of  $\text{Li}^+$  along with intercalation of  $\text{NO}_3^-$  during charging). *In-situ* XAS characterization illustrates that no active redox chemistry of Ni occurs from the NiAl LDH electrode during the first charge-discharge cycle, indicating that the charge balance during the Li-intercalation/de-intercalation is achieved by compensating  $\text{NO}_3^-$  anions, which exchange between the interlayer of NiAl LDH and the LiTFSI/LiNO<sub>3</sub> electrolyte. The addition of LiNO<sub>3</sub> on the electrolyte not only provides an additional source of  $\text{NO}_3^-$  but also boosts the shuttle kinetic of  $\text{NO}_3^-$  during the electrode operation at a broad potential window of 0.7-4.0 V (*vs.*  $\text{Li}^+/\text{Li}$ ), resulting in improved cyclic stability.

(III) NiAl LDH on CIBs (**Chapter 6**): NiAl LDH was proposed and investigated as the positive electrode on Cl-ion batteries. A compatible configuration with a suitable silver (Ag) reference electrode and a stable potential window for the electrolyte was screened out by electrochemical methods. With the as-screened configuration, a CIB system was established using NiAl LDH (with  $\text{NO}_3^-$  as the interlayer anion) as a positive electrode. The electrochemical performance and the anion shuttle mechanism of the NiAl LDH electrode are illustrated. The NiAl LDH electrode achieves a maximum discharge capacity of 695 mAh g<sup>-1</sup> (*vs.* Li), showing feasibility as positive electrode material for CIBs. Furthermore, *ex-situ* FT-IR, SEM/EDX and XPS measurements reveal the anions ( $\text{NO}_3^-$  and  $\text{Cl}^-$ ) shuttle mechanism in CIBs during the first charge-discharge cycle; which is based on a stepwise anions ( $\text{NO}_3^-/\text{Cl}^-$ ) extraction/insertion mechanism.

## Zusammenfassung

Die Verwirklichung einer sicheren, sauberen, nachhaltigen und wirtschaftlich profitablen zukünftigen Energietechnologie stellt eine der großen Herausforderungen der modernen Gesellschaft dar. Die elektrochemische Energiespeicherung liefert einen wichtigen Beitrag zur Energiewende, also hin zu unterschiedlichen primären Energiequellen und weg von den fossilen Brennstoffen. Dabei hat die Anwendung von Lithium-Ionen Batterien (LIBs) in den letzten Jahren ein zunehmendes Wachstum erfahren. Graphit ist das am häufigsten verwendete negative Elektrodenmaterial für LIBs; jedoch begrenzen dessen Eigenschaften die spezifische Energiedichte, so dass intensiv an Alternativen geforscht wird. Neben der Entwicklung von Elektrodenmaterialien für LIBs mit hoher Energiedichte, rücken auch Untersuchungen von Post-Lithium-Ionen Batterien, wie Dual-Ionen Batterien (DIBs) und Chlorid-Ionen Batterien (CIBs) in den Fokus der Forschung.

„Layered double hydroxides“ (LDHs; zu deutsch: schichtartig aufgebaute Doppelhydroxide) der allgemeinen Zusammensetzung  $[M_{1-x}M_2_x(OH)_2]^{x+}(A^{n-})_{x/n} \cdot mH_2O$  haben eine Wirtsstruktur, die aus Schichten von zweiwertigen (M1) und dreiwertigen (M2) Metallkationen ähnlich zum Mineral Hydrotalkit aufgebaut sind und bei denen sich Anionen ( $A^{n-}$ ) zum Ladungsausgleich zusammen mit Wassermolekülen in den Zwischenschichten befinden. Aufgrund der großen Abstände zwischen den Schichten, der großen Auswahl von verschiedenen Anionen, der zahlreichen Kombination an Metallionen und deren geringen Kosten, haben sich LDHs zu hervorragenden alternativen Elektrodenmaterial im Bereich der Energiespeicherung entwickelt. In dieser Arbeit liegt der Fokus auf der Untersuchung von NiAl LDH Material, welches als Elektrodenmaterial für LIBs, DIBs und CIBs verwendet wurde. Hierfür wurde die elektrochemische Leistung und der Funktionsmechanismus untersucht.

Die drei Hauptthemen, die Gegenstand dieser Arbeit sind, werden im folgendem zusammengefasst:

(I) NiAl LDH in LIBs (**Kapitel 4**): NiAl LDH mit Nitrat als Zwischenschicht wird als negatives Elektrodenmaterial für Lithium-Ionen Batterien untersucht. Die Auswirkung des Potentialbereichs (d.h. 0,01-3,0 V und 0,4-3,0 V vs.  $Li^+/Li$ ) und der Einfluss des Bindemittels auf die Leistungsdaten des Materials wird in Kombination mit einem Elektrolyten aus 1 M  $LiPF_6$  in EC/DMC untersucht. Die NiAl LDH Elektrode auf Basis von Natriumalginat (SA) Bindemittel

zeigt eine hohe anfängliche Entladekapazität von  $2586 \text{ mAh g}^{-1}$  bei  $0,05 \text{ A g}^{-1}$  und eine gute Stabilität im Potentialbereich von  $0,01\text{-}3,0 \text{ V vs. Li}^+/\text{Li}$ , besser als Elektroden mit einem auf Polyvinylidendifluorid (PVDF) basierten Bindemittel. Die mit SA-Bindemittel hergestellte NiAl-LDH Elektrode zeigt nach über 1400 Zyklen bei einer hohen Stromdichte von  $1,0 \text{ A g}^{-1}$  noch eine Kapazität von  $388 \text{ mAh g}^{-1}$ , was 27,6% der Anfangskapazität bei dieser Stromdichte entspricht. Unter den gleichen Bedingungen liefert die Elektrode auf PVDF-Basis lediglich eine Restkapazität von  $121 \text{ mAh g}^{-1}$ , also nur noch 8,5% des anfänglichen Wertes. *Ex-situ* Röntgenphotoelektronenspektroskopie (X-ray photoelectron spectroscopy (XPS)) und *ex-situ* Röntgenabsorptionsspektroskopie (X-ray absorption spectroscopy (XAS)) weisen auf einen Konversions-Reaktionsmechanismus während der  $\text{Li}^+$ -Einlagerung in das NiAl LDH Material hin. Röntgenbeugung (X-ray diffraction (XRD)) und XPS wurden mit den elektrochemischen Untersuchungen kombiniert, um die Wirkung unterschiedlicher Potentialgrenzen auf den wirksamen Mechanismus zur Speicherung der Li-Ionen zu verstehen.

(II) NiAl LDH in DIBs (**Kapitel 5**): In diesem Abschnitt wird eine neuartige DIB dargestellt, welche auf einer Multiionen-Interkalationsstrategie basiert. Dabei wird die NiAl LDH als positive Elektrode in einem formulierten Elektrolyten mit LiTFSI und  $\text{LiNO}_3$  Salzen verwendet. Die NiAl LDH positive Elektrode liefert eine maximale Entladekapazität von  $589 \text{ mAh g}^{-1}$  (bei  $20 \text{ mA g}^{-1}$ ) bei einer Kapazitätserhaltung von 26,0% nach 100 Zyklen (bei  $50 \text{ mA g}^{-1}$ ) über den Potentialbereich von  $0,7\text{-}4,0 \text{ V vs. Li}^+/\text{Li}$ . *Ex-situ* Fourier-Transformations-Infrarotspektroskopie (FT-IR) und *ex-situ* XPS Messungen veranschaulichen einen Multiionen-Wanderungsmechanismus von  $\text{Li}^+$  und  $\text{NO}_3^-$ -Ionen für diese NiAl LDH Elektroden in einer DIB, d.h. basierend auf gleichzeitiger Deinterkalation von  $\text{NO}_3^-$  und der Interkalation von  $\text{Li}^+$  aus bzw. in die LDH-Struktur während des Entladevorganges (bzw. umgekehrt Deinterkalation von  $\text{Li}^+$  zusammen mit der Interkalation von  $\text{NO}_3^-$  beim Ladevorgang). Die *in-situ* XAS Charakterisierung zeigt, dass während des ersten Lade-/Entladezyklus keine aktive Redoxreaktion von Ni in der NiAl LDH Elektrode auftritt. Dies weist darauf hin, dass der Ladungsausgleich durch  $\text{NO}_3^-$ -Anionen während der Li-Interkalation/Deinterkalation zwischen der NiAl-LDH Zwischenschicht und dem LiTFSI/ $\text{LiNO}_3$  Elektrolyten erfolgt. Die Zugabe von  $\text{LiNO}_3$  zum Elektrolyten stellt nicht nur eine zusätzliche  $\text{NO}_3^-$ -Quelle dar, sondern begünstigt auch die Kinetik der  $\text{NO}_3^-$ -Wanderung während des elektrochemischen Betriebs der Elektrode in einem breiten Potentialfenster von  $0,7\text{-}4,0 \text{ V vs. Li}^+/\text{Li}$ , was wiederum zu einer verbesserten Zyklenstabilität führt.

(III) NiAl LDH in CIBs (**Kapitel 6**): Das NiAl-LDH wurde als positive Elektrode für Chlorid-Ionen Batterien vorgeschlagen und untersucht. Eine kompatible Konfiguration mit einer geeigneten Silber (Ag)-Referenzelektrode, die über das gesamte Potentialfenster stabil ist, wurde mit Hilfe elektrochemischer Methoden ausgewählt. Mit der so ausgewählten Konfigurationen wurde dann ein CIB-System unter Verwendung von NiAl LDH (mit  $\text{NO}_3^-$  als Zwischenschichtanion) als positive Elektrode etabliert. Für dieses Zellkonzept wurden die elektrochemischen Leistungskenndaten und der Mechanismus der zugrundeliegenden Anionenbewegung in der NiAl LDH Elektrode bestimmt. Diese NiAl LDH Elektrode liefert eine maximale Entladekapazität von  $695 \text{ mAh g}^{-1}$  gegen Lithiummetall, was ihre potenzielle Eignung als positives Elektrodenmaterial für CIBs unterstreicht. Darüber hinaus zeigen *ex-situ* FT-IR, Rasterelektronenmikroskop (scanning electron microscope (SEM) / energiedispersive Röntgenspektroskopie (energy-dispersive X-ray spectroscopy (EDX) und XPS-Messungen den Ionenwanderungsmechanismus der Anionen ( $\text{NO}_3^-$  und  $\text{Cl}^-$ ) in CIBs beim ersten Lade-/Entladezyklus.



# Contents

Selbständigkeitserklärung.....	I
Acknowledgments .....	III
Abbreviations .....	VI
Figures .....	X
Abstract.....	1
Zusammenfassung .....	3
Contents.....	7
1 Motivation and aim of the thesis.....	11
2 Introduction.....	13
2.1 Background.....	13
2.2 Lithium-ion batteries.....	14
2.2.1 Working principle .....	14
2.2.2 Negative electrode materials for LIBs .....	16
2.2.3 Challenges for LIBs negative electrodes .....	21
2.3 Dual-ion batteries.....	22
2.3.1 Working principle of DIBs .....	22
2.3.2 Recent advances for DIBs.....	23
2.3.3 Challenges for DIBs.....	25
2.4 Chloride-ion batteries.....	25
2.4.1 Working principle of CIBs.....	26
2.4.2 Positive electrode materials for CIBs .....	27
2.4.3 Challenges for CIBs.....	29

2.5	Layered Double Hydroxides .....	29
2.5.1	Structure of LDHs .....	30
2.5.2	Recent advances for LDHs in electrode application.....	32
3	Battery and experimental .....	34
3.1	Battery components .....	34
3.1.1	Working principle .....	34
3.1.2	Electrode material .....	34
3.1.3	Binder.....	34
3.1.4	Conductive additives.....	36
3.1.5	Electrolyte .....	36
3.1.6	Current collector .....	37
3.1.7	Quasi reference electrode.....	38
3.1.8	Separator .....	38
3.2	Experimental .....	38
3.2.1	NiAl LDH electrode on LIBs.....	38
3.2.2	NiAl LDH electrodes on DIBs.....	40
3.2.3	NiAl LDH electrode on CIBs .....	42
4	Electrochemical study of NiAl LDH as negative electrode material for LIBs .....	44
4.1	Morphology and structure characterization .....	44
4.2	Electrochemical characterization .....	48
4.3	Li-ion storage mechanism in NiAl LDH electrode.....	52
4.4	Conclusive aspects: Li-ion storage of NiAl LDH electrode .....	59
5	Multi-ion intercalation enables NiAl LDH a positive electrode for dual-ion battery.....	61

5.1	Morphology and structure of NiAl LDH .....	61
5.2	Electrochemical performance of NiAl LDH electrode on DIB .....	62
5.3	Multi-ion storage mechanism in NiAl LDH electrode .....	67
5.4	Conclusive aspects: multi-ion storage of NiAl LDH electrode .....	77
6	Elucidation of the anion shuttle mechanism for NiAl LDH as Cl-storage electrode.....	78
6.1	Cell configuration on CIB.....	78
6.1.1	Reference electrodes .....	78
6.1.2	Electrochemical stability of the Cl-based electrolyte .....	79
6.2	Electrochemical performance of NiAl LDH electrode on CIB .....	80
6.3	Cl-ion storage mechanism in NiAl LDH electrode.....	82
6.4	Conclusive aspects: anions storage of NiAl LDH electrode.....	90
7	Conclusion .....	91
8	Outlook .....	94
9	References.....	96
10	Appendix.....	105



# 1 Motivation and aim of the thesis

The soar in global energy consumption and the limitation of conventional sources require the development of renewable energy sources, during which the research on energy storage systems is of great importance [1]. The Sony Corporation firstly commercialized carbon-based negative electrodes on lithium-ion batteries in 1991 [2]. Due to their high-voltage and lightweight storage systems, LIBs are primarily used in portable devices such as cellphones and laptops [3]. Although commercialized LIBs have achieved great success, the low theoretical capacity of graphite, which is the most widely-used negative electrode in LIBs, limits the energy density of commercial LIBs. It is imperative to develop suitable negative electrode materials to achieve high specific capacity at very negative potential.

As alternatives to LIBs, dual-ion batteries are drawing research attention for large-scale energy storage due to their cost-efficiency, inherent safety features, and high working voltages ( $> 4.5$  V). Most commonly, graphite serves as both positive and negative electrodes in the DIBs system, while the maximum anion-hosting capacities of graphite are limited (not exceeding  $150 \text{ mAh g}^{-1}$ ) due to limited active crystallographic sites in graphite electrodes [4]. Thus exploring novel cathode alternatives to improve the performance of DIBs is urgently needed.

Chlorine has higher electronegativity in the Periodic Table, and Cl ions offer higher ionic mobility and reversibility in the electrolyte, which ease the reaction kinetics and potentially facilitate mass transfer, making them prominent to be implemented as a charge transfer ion in batteries [5]. However, as many metal chlorides, which are commonly used as CIBs positive electrodes, tend to dissolve in a selection of aqueous and non-aqueous solvents [6], finding a suitable and stable cathode material for CIBs is currently a primary challenge.

Layered double hydroxides are two-dimensional ionic compounds consisting of a layered structure with alternating packed positive and negative ions [7]. Favored by their many merits such as the lamellar structure, high flexibility of ions accommodation, low cost and eco-friendly, this class of materials has found application in a variety of fields. However, to date, the application of LDHs in battery storage is significantly limited, and the storage mechanism of LDHs electrodes on different ion batteries is not clearly uncovered. With this background, this thesis focuses on the application and in-depth mechanism understanding of LDHs electrodes in energy storage, specifically on LIBs, DIBs, and CIBs.



## 2 Introduction

### 2.1 Background

The process of human civilization has rapidly changed under the continuous progress of science and technology, where energy innovations play the role of "locomotive" [8][9]. Conventional energy sources such as coal, oil, and natural gas provide most of the energy supply [10]. However, the massive combustion of fossil fuels raises many environmental and safety concerns, such as the greenhouse effect, acid rain, haze, *etc.* [11][12]. Since the global population and the demand for energy supply is growing, the energy issue is expected to be overcome by exploring the replacement of environmental-friendly and sustainable energy [13]. Renewable non-fuel energy, such as wind, solar, and tidal energy, is a popular choice to ease the energy supply shortage and reduce the consumption of fossil fuels [14][15]. Nevertheless, for instance, non-fuel renewable energy supply, solar and wind energy, face some intermittency and randomness uncertainties [16][17]. Energy storage and conversion devices are drawing increasing attention, especially in large-scale applications of non-fossil energy, to address these problems under the circumstances. Rechargeable secondary batteries and electro-catalysis are two essential categories of energy storage and conversion systems [18]. In recent decades, owing to the prominent advantages of economical operation cost and environmental friendliness, rechargeable secondary batteries are widely used in electric vehicles, hybrid electric vehicles, portable electronic devices, and other related fields [19][20][21]. Specifically, rechargeable LIBs have played an important role in energy storage systems since their first commercialization in the 1990s with superior electrochemical performance, such as high power/energy density, high output voltage, and long cycle life [22][23][24]. To meet the growing demands of energy storage systems, improving the overall electrochemical performance and reducing the manufacturing costs of the electrode materials on LIBs are the main goals [25][26][27].

In addition to LIBs, post-lithium-ion batteries, such as dual-ion batteries and anionic batteries, have been increasingly developed as alternatives to LIBs, which offer the alternative possibility for broad application in large-scale energy storage. Electrode materials play a crucial role in constructing high-performance Li-ion and post-Li-ion batteries. Developing large-capacity, long-cycle, inexpensive, and safe electrode materials are the focus of current rechargeable secondary batteries' research.

## 2.2 Lithium-ion batteries

### 2.2.1 Working principle

The charge carriers of rechargeable batteries currently mainly focus on light cations (such as  $\text{Li}^+$ ,  $\text{Na}^+$  and  $\text{K}^+$ ); amongst all elements, lithium is the lightest metal in nature and has the lowest  $\text{Li}^+/\text{Li}$  redox potential ( $-3.04\text{ V}$  vs. standard hydrogen electrode (SHE)), which endues the highest voltage when coupled with cathodes [28]. Besides, LIBs possess high energy density, which is 1.6 times that of a Ni/H battery and 4 times that of a Ni/Cd battery [29][30]. A typical LIB cell is composed of a positive electrode (a cathode electrode during the discharge process), a negative electrode (an anode electrode during the discharge process), and separators where redox reactions occur with the presence of an electrolyte.

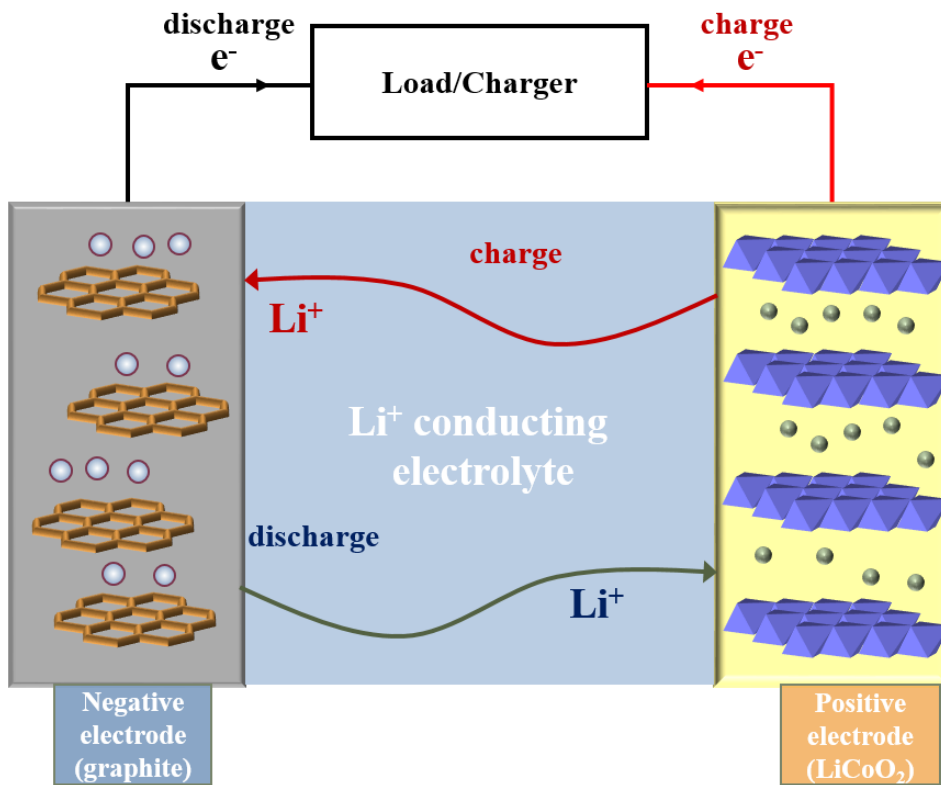
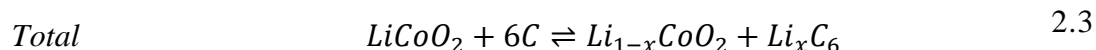
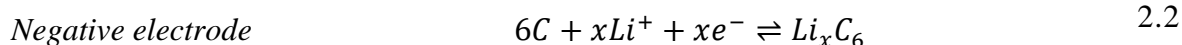
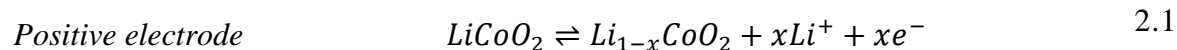


**Figure 2.1.** Schema of a rechargeable LIB. Lithium ions flow to the positive electrode through the electrolyte, and electrons flow from the external circuit during the discharge process. The flow directions are reversed during charging process.

A typical example of a LIB cell, as depicted in **Figure 2.1**, was reported for the first time by Goodenough *et al.* in 1980 [31][32], where a lithium cobalt oxide ( $\text{LiCoO}_2$ ) is applied as a positive electrode and graphite as the negative electrode in a Li-salt containing organic electrolyte [33]. The Li ions and electrons flow during the charging process of the cell based on the following reactions,



The Li ions shuttle back and forth between the positive and negative electrodes; that is, during the charging process,  $\text{Li}^+$  is de-intercalated from the positive electrode and intercalated into the negative electrode passing through the electrolyte; during the discharging process, the reaction occurs reversely [34][35][36][37].

As one of the critical components of a LIB cell, the electrolyte is currently intensively studied, among which  $\text{LiPF}_6$  and  $\text{LiTFSI}$  are commonly employed as lithium salts [38], while propylene carbonate (PC) [39], ethylene carbonate (EC) [40] and diethyl carbonate (DEC) [41] are widely used as organic solvents. Another crucial component of LIBs is the positive electrode; ideal positive electrode materials for LIBs should present good electrochemical compatibility with the electrolyte, be electrochemically stable in a fully charged state, and have fast kinetic and good reversibility for lithium-ion insertion/extraction. Based on these requirements, so far, in addition to layered-structure  $\text{LiCoO}_2$ , other prominent materials, the crystal structures are given in **Figure 2.2**, such as spinel-structured lithium-rich transition-metal layered oxide (LMO) [42][43][44], manganese-based lithium transition metal oxides ( $\text{LiNi}_{1-y-x}\text{Mn}_y\text{Co}_x\text{O}$ ) [45][46][47], and olivine-structured lithium iron phosphate ( $\text{LiFePO}_4$ ) [48][49][50] are regarded as the most widely used positive electrode materials in commercial LIBs. They have been drawing attention from the application market at different levels.

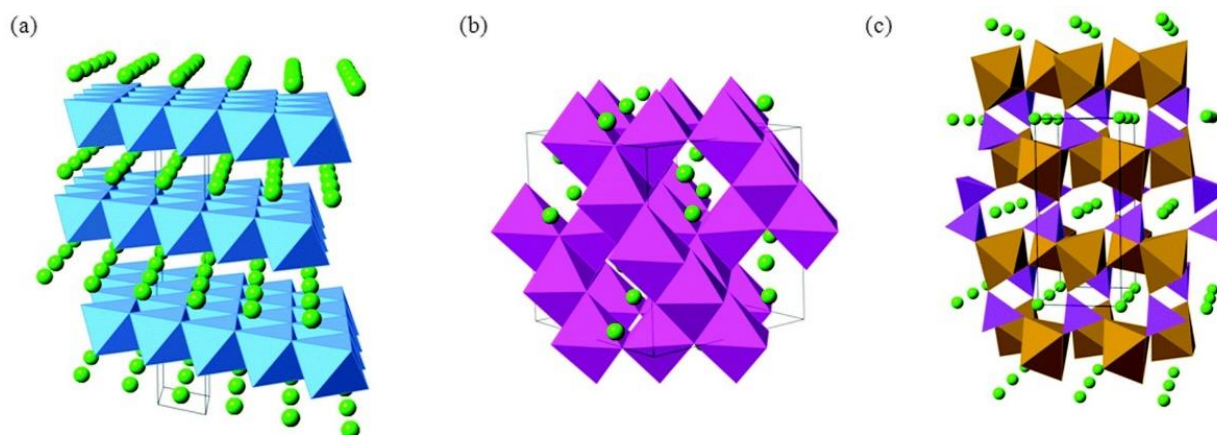


**Figure 2.2.** Representative crystal structures of positive electrode materials for LIBs: (a) layered LiCoO<sub>2</sub>, (b) spinel-structured LMO, and (c) olivine-structured LiFePO<sub>4</sub>. Copyright of The Royal Society of Chemistry 2014 [51].

### 2.2.2 Negative electrode materials for LIBs

The negative electrode for LIBs enables lithium-ion storage with high chemical stability and low working potential to guarantee the repeated insertion/extraction of lithium ions [52]. Negative electrode materials selection for LIBs is closely related to key factors, such as crystal structure as well as physical and chemical properties (specific capacity, electrical conductivity, and reversibility). With low prices and high safety, graphite has been applied as the negative electrode material on LIBs for decades. The theoretical capacity of graphite to form LiC<sub>6</sub> on LIBs, however, is merely 372 mAh g<sup>-1</sup>, which limits its energy density of LIBs when applied as an electrode [53]; such low specific capacity calls for the exploration of other alternative negative electrode materials to meet the market demand for high-energy LIBs [54][55][56].

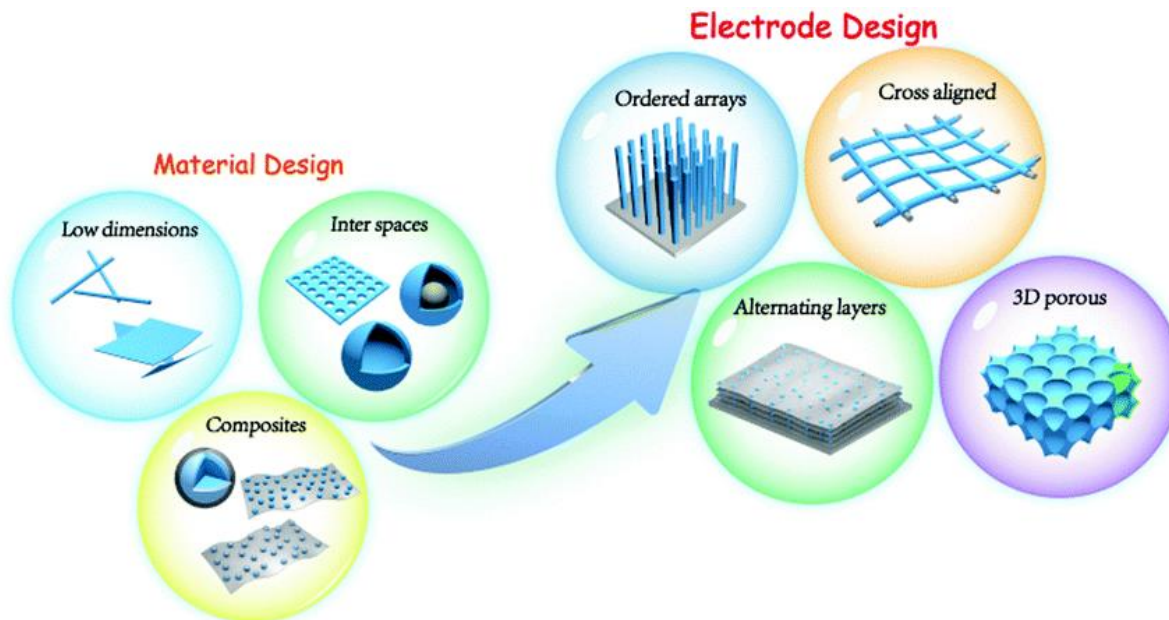


**Figure 2.3.** Negative electrode design for LIBs. Copyright from Journal of Energy Chemistry 2015 [57].

Many materials are designed accordingly to replace conventional graphite. Based on the progressive understanding of the negative electrode materials from dimensions, composites integration to interspaces adjustment, strategies on the level of negative electrode design, such as porous construction and alternating layers, as **Figure 2.3** shows, can meet the requirements of graphite replacement.

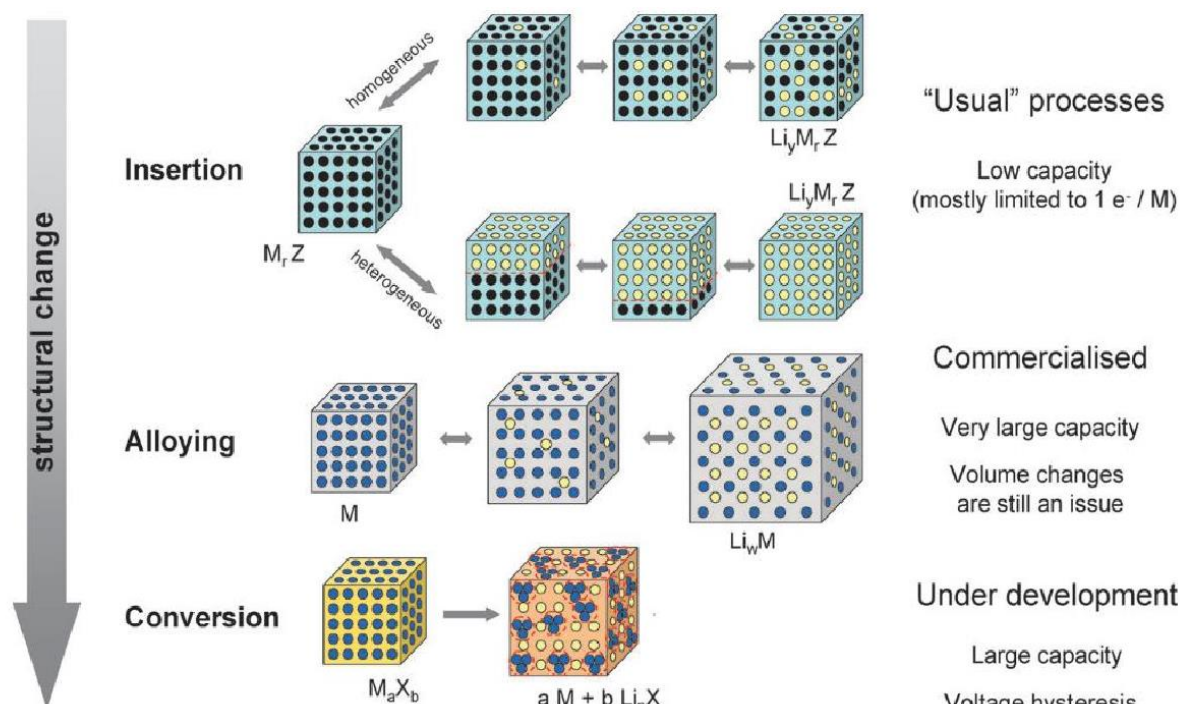


**Figure 2.4.** Negative electrode materials categories based on different reaction mechanisms for LIBs. Black circles: voids in the crystal structure, blue circles: metal, yellow circles: lithium. Reproduced with permission. Copyright from Royal Society of Chemistry 2009 [58].

Current research on negative electrode materials of LIBs can be categorized into three classes based on the Li storage mechanisms (**Figure 2.4**): i) insertion-based, ii) alloying-based, and iii) conversion-based reaction materials. The development and design of negative electrode materials should be closely associated with the Li-storage mechanisms to maximize their storage merits.

### i) Insertion-based materials

The Li-storage mechanism of insertion-based materials is based on the insertion and extraction of  $Li^+$  into the host lattice accompanied by the valence change of elements from negative electrode materials. Li insertion can happen heterogeneously with constant potential or homogeneously with changing potential along the battery operation. This working mechanism is less subjected to significant volume expansion owing to minor structural change along the battery operation,

protecting the integrity of the negative electrode materials' crystal structure from damage and achieving long cyclic life.

Apart from graphite, other non-graphite carbon-based materials are increasingly applied on LIBs based on the insertion mechanism. Hard carbon, for example, is non-graphitizable material with incomplete, dislocated, and collapsed lattice that enables lithium ions to migrate between layers and defects, resulting in a larger capacity on LIBs than conventional graphite [59][60].

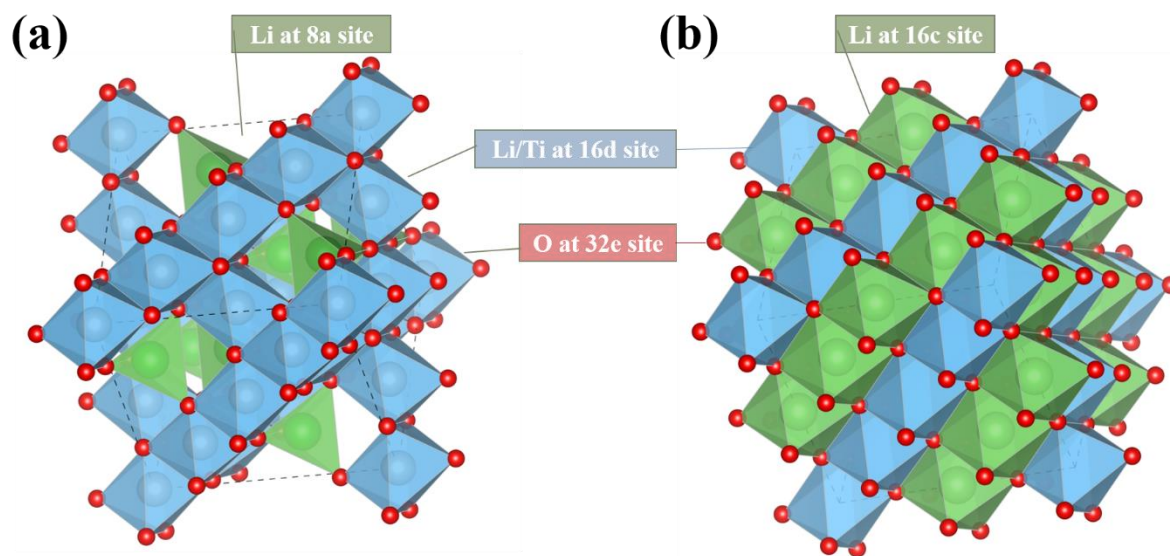
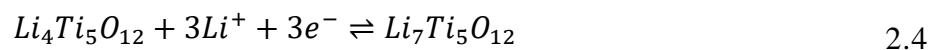


**Figure 2.5.** Unit cells of the a)  $\text{Li}_4\text{Ti}_5\text{O}_{12}$  and b)  $\text{Li}_7\text{Ti}_5\text{O}_{12}$ . During the phase transition, the Li-ions are transferred among the tetrahedral 8a sites (spinel  $[\text{Li}_3]^{8a}[\text{Li}_1\text{Ti}_5]^{16d}[\text{O}_{12}]^{32e}$ ) and the octahedral 16c sites (rock-salt  $[\text{Li}_6]^{16c}[\text{Li}_1\text{Ti}_5]^{16d}[\text{O}_{12}]^{32e}$ ). Constructed by Vesta software.

Lithium titanium oxide ( $\text{Li}_4\text{Ti}_5\text{O}_{12}$ , LTO) with a defective spinel structure is another negative electrode material that stores Li ions through an intercalation path. The insertion of Li into the spinel LTO from tetrahedral 8a sites to the octahedral 16c sites (the crystal structures of  $\text{Li}_4\text{Ti}_5\text{O}_{12}$  and  $\text{Li}_7\text{Ti}_5\text{O}_{12}$  are given in **Figure 2.5**) occurs by a two-phase process with the formation of  $\text{Li}_7\text{Ti}_5\text{O}_{12}$ . The reaction can be expressed as:



Per formula unit spinel LTO can store three Li ions, during which LTO undergoes minimal volume change owing to small lattice constant changes, which is smaller than 0.1% during Li intercalation [61]. Besides, LTO displays a relatively high lithium insertion potential plateau at  $\sim 1.55$  V (vs.  $\text{Li}^+/\text{Li}$ ), which is within most of the organic electrolytes' stability potential range, ensuring safe implementation of high-power batteries with reduced risk of lithium plating or dendrite formation at the negative electrode during charging; meanwhile, it presents a high-rate capability with a maximum discharge/charge current rate of up to 70 C [62][63][64]. However, the performance of the LTO-based negative electrode is hindered by its low specific capacity ( $175 \text{ mAh g}^{-1}$ ), resulting in a poor energy density in LIBs applications [65].

## ii) Alloying-based materials

Alloying reactions of Li with metals/semi-metals in non-aqueous electrolytes often bring high specific capacities; a negative electrode based on silicon, for example, delivers the highest theoretical gravimetric capacity amongst the negative electrode materials used on LIBs with  $4200 \text{ mAh g}^{-1}$  owing to a formation of the alloy  $\text{Li}_{44}\text{Si}$  phase [66][67]. Furthermore, many other advantages, such as being rich in resources, environmental friendliness, and economic efficiency, endow Si as an intention-drawing negative electrode material. However, as a semiconductor material, Si has poor conductivity, resulting in poor first Coulombic efficiency (CE) and cycle performance [68]. Besides, alloying mechanism-type electrodes suffer from massive volume changes (*e.g.*, expansion) during the full lithiation progress, causing a high lattice pressure of the alloy and severe electrode pulverization, consequently leading to rapid capacity decay and lithium depletion over cycles.

In order to overcome these challenges to improve the electrochemical performance of Si, magnificent efforts have been dedicated. One strategy is the nano-structural design on Si, as nano-sized Si has high structural fracture resistance, thus reducing the material crushing and improving the cycle performance [69][70]. Another strategy is proposed to apply silicon/carbon composite materials or silicon/polymer composites and form silicon and carbon into various coated structures to buffer the volume changes of the Si [71][72]. The role of carbon or polymer in silicon-based composite materials is mainly to improve the electronic conductivity of the material and buffer the process of lithiation and delithiation.

### iii) Conversion-based materials

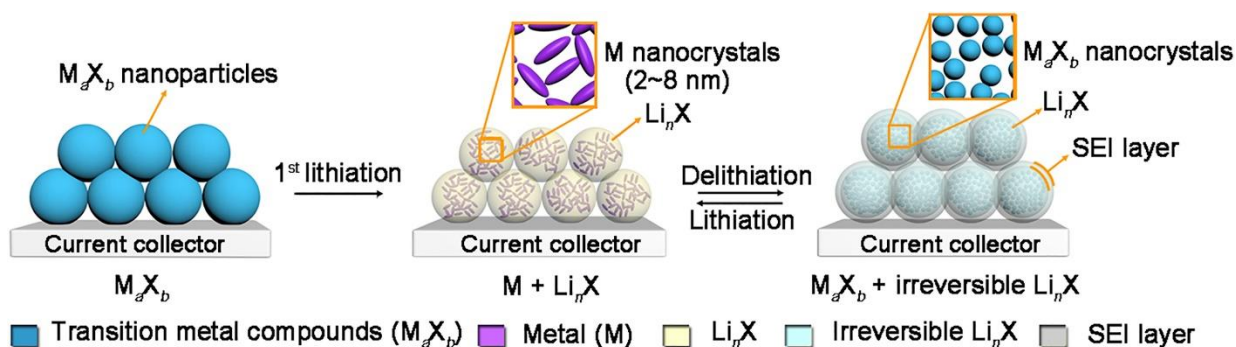


**Figure 2.6.** Schematic illustration of the local chemistry transformation during the conversion reaction, transition-metal compounds as an example. Copyright from Chem 2018 [73].

Transition metal (TM) such as Mn, Fe, Ni, Co and Ti has intrinsic properties of high electrochemical activity, rich chemical valence, and environmentally benign nature [74][75]. As the main type of conversion-based materials, transition metal compounds ( $M_aX_b$ ) as negative electrodes on LIBs present high theoretical specific capacity and good safety performance [76][77][78]. In the conversion reactions, Li reacts with  $M_aX_b$  to form lithium binary compounds ( $Li_nX$ ); meanwhile, metal ions are reduced to zero oxidation state. The chemical transformations during the conversion reaction of TMO compounds are shown in **Figure 2.6**.

Taking  $Fe_2O_3$  as an example, its conversion Li-storage mechanism can be expressed as,  $Fe_2O_3 + 6Li^+ + 6e^- \rightleftharpoons 3Li_2O + 2Fe$  (lithiation), achieving a theoretical capacity on LIBs as high as  $1005 \text{ mAh g}^{-1}$  [79]. However, the low electronic conductivity and large voltage hysteresis during cycling lead to poor cycling performance and rate capability, negatively affecting commercial development [80]. Currently, strategies to improve the shortcomings of metal oxides mainly include material structure design, material composite and nanoscale, and the preparation of doping-modified composite materials with high conductivity.

#### 2.2.3 Challenges for LIBs negative electrodes

Even though these materials are widely investigated and used on LIBs, their battery performance is limited due to the aforementioned reasons, from the inherent redox mechanism to

their intrinsic crystal structure [81][82]. Besides, the promotion of the development of electric vehicles and smart grids increases the consumption of lithium; statistically speaking, the average annual growth rate of the total consumption of global lithium resources has been 5% since 2008, and with this growth rate of 65 years, all lithium resources on earth will be exploited [83][84][85]; thus the scarcity of lithium resources can not be neglected [86][87]. These limitation conditions of LIBs further call on the exploration of novel negative electrode materials on LIBs and post-lithium-based energy storage systems.

## 2.3 Dual-ion batteries

DIBs are enabled for large-scale energy storage due to their cost-efficiency, inherent safety features, and high working voltages ( $> 4.5$  V vs.  $\text{Li}^+/\text{Li}$ ) [88][89][90]. The DIBs' mechanism was inspired by a precedent report using graphite as the positive electrode material for anion insertion, as reported by Rüdorff and Hofmann in 1938 [91], where anions can be reversibly shuttled between graphite layers. To overcome the challenges of the graphite electrode-based DIB's limited capacity, recent research on DIBs shows an increased interest in exploring anion-hosting positive electrode alternatives, *i.e.*, beyond-graphite materials [92][93][94] and multi-charge carriers, specifically, cation/anion co-working or co-intercalation-based materials [95].

### 2.3.1 Working principle of DIBs

Dual-ion batteries are constructed in the same configuration as traditional rocking chair batteries, composed of positive and negative electrodes, separated by a polymeric membrane and operating in an electrolyte. Unlike LIBs, where Li-ion is applied as the only carrier to shuttle back and forth between electrodes, in a DIB, cation and anion work simultaneously. It is worth noting that the high anion intercalation potential makes DIBs functional at a high potential (above 4.5 V vs.  $\text{Li}^+/\text{Li}$ ), enabling a high energy density [96][97][98].

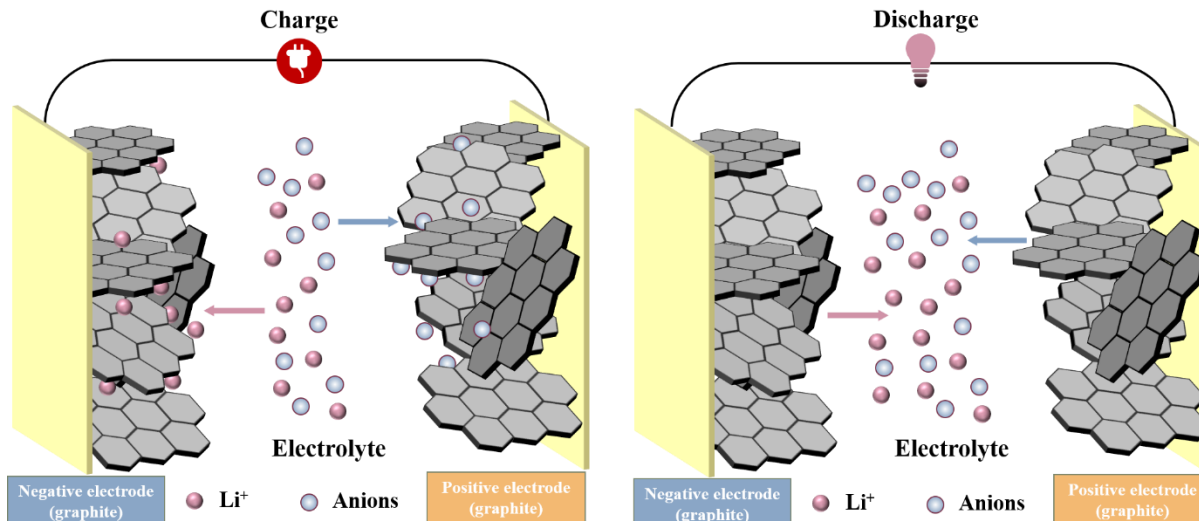


**Figure 2.7.** Schematic diagram of the working mechanism of a DIB.

**Figure 2.7** illustrates the working mechanism of graphite-based DIBs. During the charging process, Li ions from the electrolyte intercalate into the negative material (graphite); meanwhile, anions from the electrolyte (such as  $\text{PF}_6^-$  ions) intercalate into the positive material (graphite). The  $\text{Li}^+$  and anions migrate to the electrolyte during the discharging process. In DIBs, the electrolytes not only help transfer the charge carriers but also act as the active materials as the source of anions and cations. During the charging process, the anions and cations from the electrolytes migrate to the positive and negative electrodes, respectively, and during the discharging process, the inverse reaction occurs. The short migration path between electrolytes and two electrodes facilitates the fast ionic migration of both anions and cations, resulting in a fast kinetic reaction compared to LIBs. In particular, various anions can shuttle between electrodes through an electrolyte divided into insertion type, conversion type, and conversion-insertion type DIBs.

### 2.3.2 Recent advances for DIBs

DIBs own great advantages, including low cost, high output voltage, and environmental friendliness. However, a high operating voltage will lead to electrolyte decomposition. Besides, a low average capacity of host materials for anion intercalation hampers the application of DIBs. To stabilize the electrochemical performance, DIBs must develop an appropriate anion-hosting

material with a compatible electrolyte. So far, few electrode materials can realize anion intercalation. Graphite is the most commonly used positive electrode material on DIBs owing to its stable structures and large interlayer distances. However, the increase of layer spacing in the *c*-axis direction causes graphite volume expansion and destroys the electrode structure during cell operation [91]. In the following studies on graphite-based DIBs reported by Kravchyk *et al.*, graphite serves as both positive and negative electrodes, and the maximum discharge capacities of anion intercalation are within the range of 100–150 mAh g<sup>-1</sup> [97].

In the subsequent decades, the mechanism of anion embedding into graphite structure has been further investigated. Beltrop *et al.* unveiled that the diameter of anions has a significant impact on their embedding behavior: the larger the diameter of an anion is, the more difficult it is to be inserted into graphite (considering the interaction between anion and electrolyte solvent) [99]. Wang *et al.* [100] recently prepared high-purity graphene with an improved electrochemical stripping method. This stripped graphene can be used as positive and negative materials simultaneously. A rechargeable battery was constructed based on cationic Na<sup>+</sup> and anionic PF<sub>6</sub><sup>-</sup> double intercalation in an organic-based electrolyte. The exfoliated graphene electrode provides high charging and discharging potentials of 4.7 V and 4.3 V (*vs.* Na<sup>+</sup>/Na), respectively, by reversibly storing PF<sub>6</sub><sup>-</sup> anions. After 250 cycles, the capacity remains above 90 mAh g<sup>-1</sup> at 100 mA g<sup>-1</sup>.

Nevertheless, the intercalation of anions into conventional graphite carbon usually requires a working potential higher than 4.5 V (*vs.* Li<sup>+</sup>/Li), which may lead to the peeling of the graphite layer or the decomposition of traditional organic electrolytes, causing adverse effects on the cyclic life of DIBs. On the other hand, the low capacity of graphite significantly limits its performance as the electrode material on DIBs. The delivered capacity and cycling stability of DIBs can be improved by introducing metal-based materials (*e.g.*, Li, K, Mg, or Al) as negative electrodes, as alkali metal ions present good compatibility and benefit weight saving [101]. For example, Qin *et al.* developed an Al-based negative electrode with a bubble-sheet-like hollow interface on Al and applied it to a DIB cell. In this reported DIB cell, a carbon-coated hollow aluminum negative electrode was prepared and worked as both negative electrode material and current collector, while graphite was used as the positive electrode material. This strategy inhibits the stress generated by the lithium intercalation process and mitigates the volumetric expansion. Consequently, the battery

cell shows excellent cycling performance within 1500 cycles with a capacity retention of 99% at a rate of 2 C [102].

### 2.3.3 Challenges for DIBs

Since the size of anions (2.64 Å for  $\text{NO}_3^-$ , 3.5×3.5 Å for  $\text{PF}_6^-$  and 3.9×8.0 Å for  $\text{TFSI}^-$  as a rectangular shape with dimensions) is larger than that of Li ions (0.76 Å)[103][104], graphite can accommodate far fewer anions than lithium ions, which is challenging for reaching the theoretical specific capacities. Finding positive electrode materials with similar properties to graphite, high accommodation ability for anions, and higher specific capacity is essential for improving the capacity of DIBs [93][92][105]. Notably, aluminum foil can cause severe volume expansion to destroy the SEI film during cell operation, thus negatively affecting the electrochemical performance of DIBs [106]. On the other hand, unlike conventional commercial LIBs, where the charge carriers originate from the active positive electrode material, the charge carriers in DIBs come from lithium salts dissolved in the electrolyte [107]. So it is necessary to either use a large amount of electrolytes or increase the concentration of the electrolytes when preparing a DIB. Based on these concerns, exploring negative electrode materials with high energy storage capability and formulating electrolytes allowing rapid charge carriers transportation for DIBs are important research directions.

## 2.4 Chloride-ion batteries

Even if most research on rechargeable batteries, to date, focuses on the reversible migration of light metal cations-based mechanisms, a novel electrochemical system designed with anion as transport carriers have received attention in recent years [96][108]. Specifically, based on the chloride-ion shuttle mechanism, chloride-ion batteries stand out by the use of Cl ion-containing electrolytes, which are abundant in nature and economically efficient for mass production [109]. CIBs can provide a high theoretical volumetric energy density ( $\sim 2500 \text{ Wh L}^{-1}$ ) [110][111][112], and show good flexibility for a wide variety of choices for negative electrode materials such as Li, Na, Mg, Ca, and graphite [113]. Such abundant and cheap component resources and prominently high energy density enable CIBs to be potentially applied to large-scale electric energy storage and conversion equipment [114][115].

### 2.4.1 Working principle of CIBs

A common CIB uses metal chloride ( $MCl_x$ ) or metal oxychlorides ( $MOCl$ ) as a positive electrode, a pure metal (alkali metal, alkaline earth metal or rare earth metal) where Cl-ion oxidation occurs as a negative electrode, a chloride-conducting salt of ionic liquid or organic compound dissolved with solvent are used as electrolyte [116]. The working principle of a CIB is depicted in **Figure 2.8**.

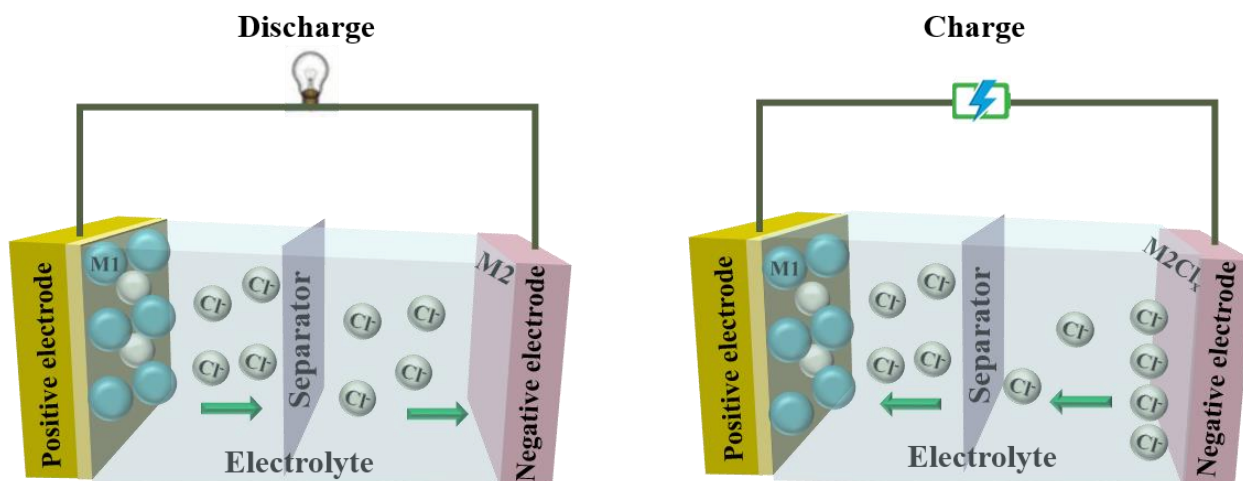
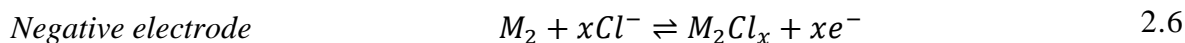
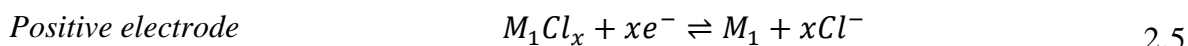


**Figure 2.8.** Working principle of a CIB.

The mechanism of CIB can be described as follows. During discharging, Cl ions shuttle from the positive electrode to the negative electrode through the electrolyte to chlorinate the negative electrode. When the battery is charged, Cl ions are extracted from the negative electrode and migrate back to the positive electrode. The corresponding redox reactions occurring at the electrodes can be described as equations in 2.5-2.6 [113]. The more chloride ions react, the higher the capacity can be delivered [5].



Where ‘ $M_1Cl$ ’ represents metal chloride, metal oxychlorides or organic chlorides, and  $M_2$  refers to highly electropositive metals (for example, Li).

## 2.4.2 Positive electrode materials for CIBs

To date, metal chloride, metal oxychloride [117][118][119][120], and polymers [121][122] have been investigated as positive electrode materials on CIBs, as summarized in **Table 2.1**.

**Table 2.1** Battery components and main research results on CIBs.

Positive electrode	Negative electrode	Electrolyte	Maximum capacity (mAh g <sup>-1</sup> )	Cycles	Capacity after cycling (mAh g <sup>-1</sup> )	Reference
CoCl <sub>2</sub> , VCl <sub>3</sub> , BiCl <sub>3</sub>	Li	[OMIM]Cl with [BMIM][BF <sub>4</sub> ]	142.9	3	75	[110]
FeOCl	Li	N <sub>116(14)</sub> Cl in N <sub>1114</sub> TFSI	158	30	60	[118]
VOCl	Li	PP <sub>14</sub> Cl in PC	189	100	113	[119]
PPy on CNT	Li	PP <sub>14</sub> Cl in PP <sub>15</sub> TFSI	118	40	90	[121]
VOCl	Mg	PP <sub>14</sub> Cl in PP <sub>15</sub> TFSI	101	53	60	[123]
FeOCl, BiOCl	Mg	PP <sub>14</sub> Cl in PP <sub>15</sub> TFSI	130	30	19.5	[124]

### i) Metal chlorides and metal oxychlorides

In the early research on CIBs by Zhao *et al.* [116], three metal chlorides (*i.e.*, CoCl<sub>2</sub>, VCl<sub>3</sub> and BiCl<sub>3</sub> compounded with carbon black) were applied as the positive electrodes, with a metal lithium as the negative electrode operating in a mixture of (1-methyl-3-octyl imidazoline chloride ([OMIM][Cl]) and 1-butyl-3-methylimidazolium tetrafluoroborate ([BMIM][BF<sub>4</sub>]) ionic liquid electrolyte. The CIBs were investigated at a potential window of 1.6-3.5 V (*vs.* Li). These simple metal chlorides show an initial discharge capacity of 80-180 mAh g<sup>-1</sup> at 3 mA g<sup>-1</sup>, marking the first principle of rechargeable battery based on chloride ions shuttle. However, metal chlorides suffer from drawbacks such as rapid capacity decay during the cycling process because of the high volume changes due to the possible conversion-based mechanism and the potential solubility issues of chlorides in the electrolyte.

Compared with metal chlorides, metal oxychlorides have been proposed to minimize the dissolution of active material during the operation of CIBs owing to their higher chemical stability against metal dissolution, as their cations are strongly bonded with the Lewis basic  $O^{2-}$  anions. Furthermore, the metal oxychlorides form an adjacent layered structure, in which layers are connected by van der Waals forces [125].

Metal oxychlorides (bismuth oxychloride (BiOCl) and iron oxychloride (FeOCl)) were investigated as positive electrode materials on CIBs by Zhao *et al.*, where Li was applied as negative electrode and 0.5 M  $N_{116(14)}Cl$  in  $N_{1114}TFSI$  as electrolyte [126]. Both positive electrodes show reversible reactions based on the chloride shuttle. BiOCl and FeOCl positive electrodes deliver the initial discharge capacity of 59 mAh  $g^{-1}$  and 158 mAh  $g^{-1}$ , respectively. Furthermore, the cyclic stability of FeOCl positive electrode shows retention of 38% for 30 cycles. This report confirms the feasibility of metal oxychlorides as positive electrode materials on CIBs; however, the poor cyclic stability hinders the overall battery performance. Besides, Gao *et al.* proposed applying VOCl as a positive electrode material on CIBs, where lithium worked as a negative electrode operating in a Cl ion transporting liquid electrolyte, showing good reversibility with a retained reversible capacity of 113 mAh  $g^{-1}$  after 100 cycles [119].

To further improve the electrochemical performance of FeOCl, carbon was incorporated to form a positive electrode nanocomposite by the same group. This compound gives a maximum discharge capacity of 202 mAh  $g^{-1}$ , and capacity retention of 80.2% after 30 cycles [127]. The configuration based on VOCl or FeOCl against Li negative electrode on CIBs can support longer cycles and higher capacities compared with other materials; however, the fast capacity decay observed in the FeOCl/Li system is challenging. One explanation for this sluggish performance is the contact loss between active material particles due to phase transformations, causing significant volume changes. Besides, the VOCl/Li CIB system shows a LiCl dissolution, indicating a possible interference of intercalated Li into the VOCl positive electrode that cannot be ignored; this is whereas has not been firmly proved.

## ii) Cl-doped conducting polymer

Apart from the above-mentioned inorganic Cl-containing compounds, organic conductive polymers have been proposed as positive electrode materials to improve the performance of CIBs.

Geschwind *et al.* investigated polyaniline (PANI) material as a positive electrode for CIBs, where a high initial capacity of 150 mAh g<sup>-1</sup> is achieved [122]. Nevertheless, the understanding of the mechanism is not yet wholly clarified. Additionally, only discharge processes were illustrated. Zhao *et al.* coated chloride-ion-doped polypyrrole (PPy) on a carbon nanotube substrate (PPyCl@CNTs) and applied it as a positive electrode on CIBs in the electrolyte of 0.5 M PP<sub>14</sub>Cl in PP<sub>14</sub>TFSI [121]. The electrode achieves a maximum discharge capacity of 118 mAh g<sup>-1</sup> and increased cycling stability with a slow capacity decay and a retained capacity of 90 mAh g<sup>-1</sup> over 40 cycles. The reported cell was built into a pouch cell and could power a commercially available red light-emitting diode (LED) for more than 5 min. Up to present, no reported CIBs show good enough performances comparable to LIBs [128][129], and no commercially available CIBs have been built yet due to current technical limitations.

### 2.4.3 Challenges for CIBs

Although some reported positive electrode materials offer improved stability and electrochemical properties, some drawbacks of CIBs still call for more effort and inputs due to limited research. The main obstacle of the chloride salts electrode materials is that the corresponding battery capacity decays rapidly, which often fails to exceed 100 cycles due to the dissolution of the electrode. Based on this, current research on CIBs mainly focuses on finding new positive electrode materials that can achieve stable cyclic performance. While the elucidation of the capacity fading mechanism of LDHs on CIBs still lacks reports. Thus, understanding the capacity decay of LDHs electrodes is an essential direction for CIB research.

## 2.5 Layered Double Hydroxides

As widely applied anion-hosting layered materials, LDHs emerged as prominent electrode alternatives in the energy storage field. LDHs are structurally constituted by hydrotalcite-like host layers that consist of divalent (M<sup>2+</sup>) and trivalent (M<sup>3+</sup>) metal cations, and charge-balancing interlayer anions (A<sup>n-</sup>) with water molecules [130][131][132]. The large interlayer space, abundance of anions choices and the flexibility of transition metal ions make LDHs promising for designing high-performance electrode materials for energy storage and conversion.

### 2.5.1 Structure of LDHs

Layered double hydroxides are a class of two-dimensional (2D) anionic clays made up of positively charged brucite-like host layers and exchangeable charge-balancing interlayer anions that can be expressed as [130][133]:



In which, M1 and M2 are divalent and trivalent cations, respectively.  $A^{n-}$  is the interlayer anion compensating for the positive charge of the brucite-like layers. The structure of nitrate-intercalated LDHs is shown in **Figure 2.9**. Analogous to graphite, LDHs materials are assembled by van der Waals forces along one crystallographic direction to provide large interstitial sites for anion intercalation; thus, the driving force of cations and anions is able to overcome the weak interlayer van der Waals forces when charging to a high potential [89].

The interlayer space of LDH materials is large enough for the rapid insertion and extraction of various ions. Benefiting from the flexible layered structure, LDHs can provide a large specific surface area (100~300 m<sup>2</sup> g<sup>-1</sup>). In addition, LDHs possess adjustable physical and chemical properties, which can be easily achieved by replacing the metal cations, tuning the molar ratio of metals, and altering the interlayer anions. The morphological diversity and the flexibility of incorporating mixed-valence transition metal ions into the LDHs structure in different compositions make its application promising in many fields, including catalysis [134][135], biochemistry [136][137], waste-water remediation, and supercapacitors [138][139][140][141], as well as the design of high-performance electrode materials for application in ion-storage [142].

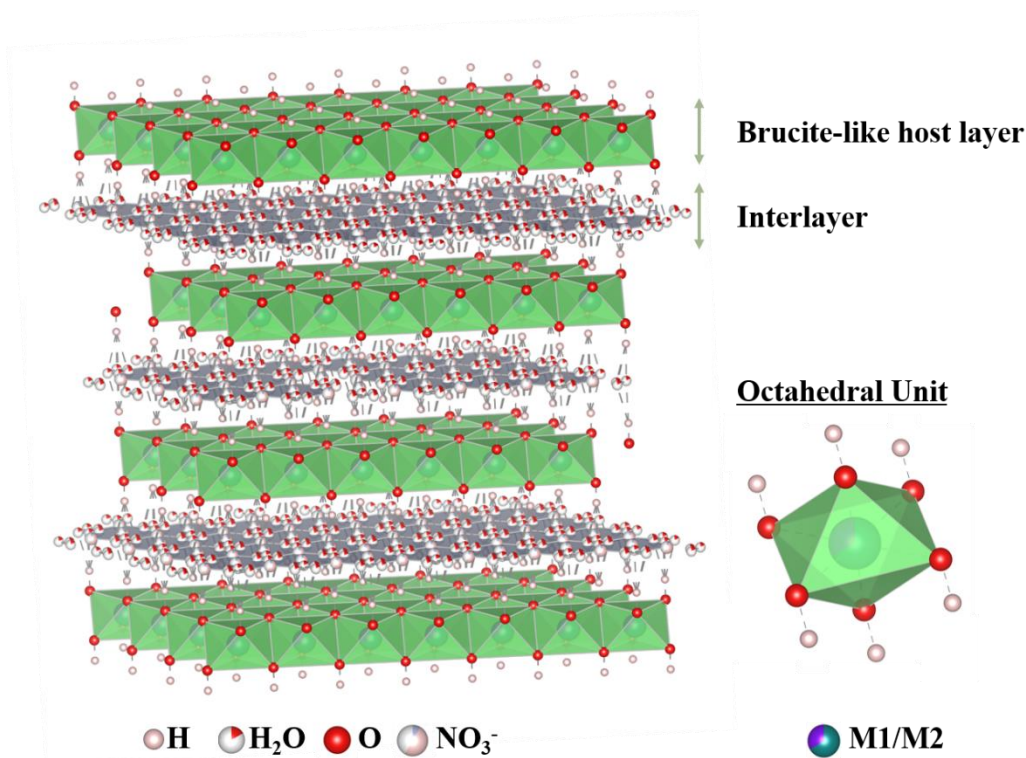
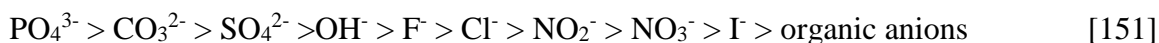


**Figure 2.9.** The structure of nitrate-intercalated LDHs with the metal hydroxide octahedra stacked along the crystallographic  $c$ -axis.

Metal cations in the host layers of LDH can chemisorb with ions and molecules from the electrolytes, conduct charge migration through reversible redox reactions, and induce faradaic pseudocapacitance. LDHs, stand out compared with traditional carbon-based electrode materials with higher specific capacitance. During the electrodes' working, the electrode surface and the bulk materials participate simultaneously in energy storage, improving the corresponding electrochemical performance [143][144]. Thus LDHs are regarded as excellent electrode materials for supercapacitors [145][146][147][148]. Li *et al.* [149] reported the electrode materials of NiAl LDH supercapacitors with different Ni/Al ratios and studied the effects of crystal structure, morphology, and interlayer structure on capacitance properties. Interestingly, when the Ni/Al ratio is 3:1, the NiAl LDH electrode achieves a mass-specific capacitance of  $2128 \text{ F g}^{-1}$  at  $1.0 \text{ A g}^{-1}$  with good cycle stability. The excellent electrochemical performance can be attributed to the introduction of  $\text{Al}^{3+}$ . The Ni/Al ratio increases lead to wider interlayer space and, therefore, to

faster ion diffusion kinetics. Loh *et al.* [150] found noticeable results in coal LDH. The introduction of  $\text{Al}^{3+}$  ion improves the electrochemical performance; furthermore, the content of  $\text{Al}^{3+}$  is positively correlated with the cycle stability and negatively correlated with the mass-specific capacitance; specifically, the appropriate introduction of  $\text{Al}^{3+}$  ion affects the micromorphology and improves the electrochemical performance.

In addition to metal cations, interlayer anions play a similarly important role in the electrochemical behavior of LDHs. The interlayer space can provide active sites for charge storage. However, the cations in the host layers of LDHs may strongly interact with the anions between the layers, making it difficult for the corresponding electrolyte ions to enter. The order of the interaction is (easy > hard):



Liu *et al.* reported the effects of different LDH's interlayer anions ( $\text{NO}_3^-$ ,  $\text{SO}_4^{2-}$ , and  $\text{Cl}^-$ ) on the structure and capacitive properties of CoMn LDH [152]. Different interlayer anions significantly affect the phase structure and charge storage properties of CoMn LDH materials.  $\text{SO}_4^{2-}$ -embedded LDH has the most stable layer structure and large interlayer spacing, exhibiting excellent supercapacitive behavior and showing a high area capacity of  $582.07 \text{ mC cm}^{-2}$  at  $2 \text{ mA cm}^{-2}$ , which is higher than other anions-based LDH electrode materials.

## 2.5.2 Recent advances for LDHs in electrode application

Although LDHs' flexible and adjustable structure has made them interesting materials in supercapacitors, in the field of rechargeable batteries, they are typically used as precursors or templates for synthesizing metal oxides, which are then used as electrode's active materials in metal-ion batteries [62]. The wide tunability of the metal ions in their host layers and the readiness of metal oxides conversion by calcination make LDHs excellent precursors for highly active negative electrode materials on ions storage. For example, Li *et al.* prepared a pure  $\text{NiFe}_2\text{O}_4$  spinel from a  $\text{NiFe}^{2+}\text{Fe}^{3+}$ -LDH precursor after calcination and applied it on LIBs [153]. The material delivers an initial discharge capacity of  $1239 \text{ mAh g}^{-1}$  and a reversible capacity of  $701 \text{ mAh g}^{-1}$ . The LDH precursor methods have significant advantages for synthesizing  $\text{NiFe}_2\text{O}_4$ . Indeed, with this method, a spinel with small particle sizes and uniform distribution of metal cations, which facilitates active site exposure and the Li-ion intercalation, can be prepared.

The application of LDHs-based composites directly as electrode materials was reported only recently (including a work presented in this thesis). For instance, Shi *et al.* presented the graphene-wrapped NiCo LDH as a negative electrode for LIBs [154]. The proposed NiCo LDH composite electrode exhibits a high reversible specific capacity of 1428 mAh g<sup>-1</sup> at 0.05 A g<sup>-1</sup> and excellent capacity retention of 75% after 10000 cycles at 10 A g<sup>-1</sup> in the potential range of 0.01-3.0 V vs. Li<sup>+</sup>/Li. Zhang *et al.* synthesized a Co<sub>3</sub>V<sub>2</sub>O<sub>8</sub>@NiCo LDH material, revealing a reversible specific capacity of 1329.4 mAh g<sup>-1</sup> at 1.0 A g<sup>-1</sup> after 500 cycles and good cycling performance (893.1 mAh g<sup>-1</sup> at 5 A g<sup>-1</sup> after 950 cycles) [155].

This bi-material shows improved performance compared to the single component-based electrodes, which are widely used in other secondary batteries. Li *et al.* reported an active material consisting of porous nanoflakes of Ni-Co hydroxides and Bi<sub>2</sub>O<sub>3</sub> that are successfully assembled on substrates of carbon cloth/carbon nanofiber 3D network (CC/CNF). This Ni/Bi battery delivers a capacity of 110 mAh g<sup>-1</sup> at a current density of 2 A g<sup>-1</sup>, and about 80% of its capacity (85 mAh g<sup>-1</sup>) can be retained when the current density increases to 20 A g<sup>-1</sup> [156].

Moreover, Wang *et al.* proposed a Ni-Zn battery with a Zn-doped NiMn LDH as an electrode, which achieves a high specific capacity of 294 mAh g<sup>-1</sup> at 1 A g<sup>-1</sup> and enhanced stability [157]. In addition, Yin *et al.* used a Cl-containing NiFe LDH as a promising positive electrode material for CIBs. The as-reported NiFe-LDH ([Ni<sub>2</sub>Fe(OH)<sub>6</sub>]Cl·1.37H<sub>2</sub>O) exhibits a maximum capacity of 350.6 mAh g<sup>-1</sup> and a long lifetime of over 800 cycles (at 101.1 mAh g<sup>-1</sup>) at 100 mA g<sup>-1</sup>, which is superior to most currently reported CIB positive electrode materials [158].

Recent studies have been illustrating the application of LDHs on CIBs [159][160][161]. In the latest research, chloride ion-containing layered materials, similar to graphite on LIBs, have been reported to provide a new direction for the development of CIBs. Han *et al.* introduced CoFe LDH as positive electrode material on CIBs for the first time, where a metal lithium foil was used as the positive electrode, and an ionic liquid was used as an electrolyte [162]. This configuration shows an operable electrochemical performance with a specific capacity of 239.3 mAh g<sup>-1</sup>, and a cyclic stability during 100 charge-discharge cycles with a capacity retention of 160 mAh g<sup>-1</sup>.

### **3 Battery and experimental**

The battery fundamentals and experimental processes in this thesis, including material synthesis, sample characterization, electrode preparation, battery assembly, and battery testing, are covered in this chapter.

#### **3.1 Battery components**

##### **3.1.1 Working principle**

A rechargeable battery is commonly made of multiple cells connected in series. One cell consists of a positive electrode (cathode), a negative electrode (anode), separators and an electrolyte. The electrodes are prepared by coating a slurry (a mixture of active material, binder, and conductive additive) on a current collector. The separator is placed between the electrodes as a safeguard against short circuits. All cell parts are placed in an electrolyte, which functions as a medium for charge transportation. The cell can be charged and discharged when connected to an electric circuit [163].

##### **3.1.2 Electrode material**

Electrodes are prepared by mixing the active material, binder (with a solvent), and conductive additive into a slurry, which is then coated on a current collector. The active material represents the reservoir for the ions shuttled between the electrodes (*e.g.*,  $\text{LiCoO}_2$  as the positive electrode and graphite as the negative electrode [22]; the electrochemical reactions are given in equations 2.1-2.3). This storage capability delivers the capacity of the cell. Besides showing high capacities, the active materials should be electrochemically active and able to provide enough cell voltage for a high energy density. Other desired properties are good conductivity, stability, ease of manufacture, and low cost [164].

##### **3.1.3 Binder**

The binder is supposed to connect all electrode components, provide good contact to the current collector, and be inert to other cell parts. A volume change may happen to the electrode during the charge-discharge process due to intercalation or phase changes. The binder must be resistant to mechanical stress to stabilize the structure of the active materials [165]. The binder supports the

coherence between active material particles, conductive additives, and the current collector and its inherent conductive properties, thus affecting the electrode conductivity. To achieve desirable performance, a suitable binder should provide good contact, high mechanical and electrochemical stability, and beneficial conductive properties.

In the slurry preparation process, the binder solvent must first wet the active material/conductive additive powder. A mechanical treatment breaks apart aggregates and agglomerates of particles. The binder should possess good dispersing properties with the solvent to stabilize particles against accumulation and precipitation. Besides, a solvent with economic efficiency, environmental friendliness, non-toxicity, and ease of handling is suitable for possible future production on a commercial level [166].

The most widely used binder for commercial LIBs is polyvinylidene fluoride (PVDF), which is dissolved in N-methyl pyrrolidone (NMP) solvent during the electrode fabrication [167]. PVDF is a non-conductive polymer binder with a high electrochemical stability window and good adhesion properties [168].

Nevertheless, the ultimately weak van der Waals forces between the active material particles and PVDF binder could lead to a severe capacity loss when PVDF is applied in high-capacity electrodes with substantial volume changes (such as Si) [169]. Another disadvantage is the hazardous and volatile nature of the NMP solvent, which is even more challenging to handle since its humidity has to be held below 2% during electrode manufacturing [170].

In finding ways to mitigate these disadvantages brought by PVDF, sodium alginate (SA) as an alternative electrode binder candidate has been proposed. SA is a compound primarily applied in food, pharmaceutical, and other fields [171]. One of its most intriguing characteristics is its water-processability [172]. In contrast to PVDF, de-ionized water and isopropanol, both easy to handle and widely available, can be used as co-solvents of SA binder in slurry preparation. Furthermore, SA possesses a high number of carboxylic groups and a significant polarity, which is around 50 times stiffer than PVDF and helps to form a great number of binder bonds to the active material [173]. This ensures strong adhesion between the active material and the current collector, promising its resulting properties. In reports on LIBs and sodium-ion batteries, the SA binder has shown superior performance compared to PVDF [174][175].

### 3.1.4 Conductive additives

The conductive additive is an electrode component that ensures good electric contact between active material particles to enhance the electronic flow [166]. Carbon black is a commonly used additive owing to its highly conductive and readily dispersible merits. Carbon black covers the surface of the active material particles in an exemplary network and thus provides a pathway for the flowing electrons [176].

### 3.1.5 Electrolyte

The electrolyte is an ionic conductor that serves as a medium for ion transfer inside the cell between the positive and negative electrodes. It is typically a dissolved salt, acid, or alkalis in water or other solvents. Solid or gel-type polymer electrolytes are also commonly present in some other batteries. Electrolytes are not electronically conductive to prevent short circuits. Further desired properties for electrolytes are non-reactivity towards the active material, broad thermostable window, and wide electrochemical stability window. Moreover, it must be cost-efficient and safe to handle [177].

LP30 is a widely used electrolyte in LIBs. LP30 is composed of lithium hexafluorophosphate (1.0 M  $\text{LiPF}_6$ ) salt and ethylene carbonate (EC), and dimethyl carbonate (DMC) (1:1 by volume) solvent.  $\text{LiPF}_6$  is highly conductive, consisting of anions with electron-withdrawing groups that reduce the interaction with  $\text{Li}^+$ , thus allowing it to move freely [178]. The conductivity of the LP30 electrolyte is  $10.7 \text{ mS cm}^{-1}$ . The solvent is composed of carbonates to increase fluidity and decrease the melting point of the electrolyte [179]. Furthermore, lithium bis(trifluoromethane sulfonyl) imide ( $\text{LiTFSI}$ ) is expected to be promising for LDH-type electrode materials since it owns the advantages of high solubility, low water sensitivity, and good thermal stability over lithium metal [180].

Until now, ionic liquid (IL) electrolytes have been reported as the most used type of electrolyte on CIBs owing to their merits, such as high thermal stability, wide electrochemical stability window, and non-toxicity [181][182]. Common electrolytes for CIBs are ILs with cations of imidazolium, piperidinium, pyridinium, pyrrolidinium, and quaternary ammonium [116]. The main challenge of using IL is the potential dissolution of electrode materials. To date, only a few studies on polymer-based electrolytes have been conducted, and ceramic-based ones have not been

explored yet [183][184]. Combining ILs with low viscous carbonate solvents can ease the drawbacks of ILs of high viscosity and poor ionic conductivity [185].

In this thesis, LP30 was applied as the electrolyte in LIBs from work in chapter 4; LiTFSI in dimethoxyethane (DME) was used as the electrolyte in DIB from work in chapter 5, and butyl-1-methylpyrrolidinium chloride (Bpy<sub>14</sub>Cl) in propylene carbonate (PC) was used as the electrolyte in CIB from work in chapter 6.

### 3.1.6 Current collector

The current collector is a thin substrate on which the slurry is coated and thus connects active material with the electric circuit. It should provide high conductivity and non-reactivity towards other cell parts and low cost and weight [186]. Commercial current collectors for LIBs are Cu (for the negative) and Al (for the positive electrode). Al is the lighter and cheaper material compared to Cu. However, Al cannot be used on the negative electrode side because lithium/aluminum alloys can be formed with Al at low potential. In turn, Cu is a current collector on the negative electrode side. Additionally, stainless steel (SS) is also widely investigated as the current collector. SS is a class of alloy steel consisting of nickel, molybdenum, titanium, niobium, copper, iron, chromium, and other elements [187]. It possesses good electrical conductivity, high electrochemical stability, and high resistance to chemical corrosiveness (such as air, water, and acids). Stainless steel is prone to form a passivation film on its surface, thus protecting the metal bulk from corrosion [188]. Besides, thinner stainless steel can be produced than copper as the current collector. Other advantages, such as low cost, facile process, and large-scale production, make stainless steel a prominent alternative current collector [189].

In this thesis, Cu is used as the current collector for NiAl LDH negative electrode on LIBs in LP30 electrolyte at a potential window of 0.01-3.0 V (*vs.* Li<sup>+</sup>/Li). Besides, stainless steel is used as the current collector for the NiAl LDH electrode on DIBs at a high potential window of 0.07-4.0 V (*vs.* Li<sup>+</sup>/Li). In the experiment of NiAl LDH on CIBs, the literature reports the usage of stainless steel as the current collector because of its high compatibility with the corrosive electrolyte [120][160].

### 3.1.7 Quasi reference electrode

A reference electrode has a known potential value and is designed to reach an ideal non-polarizable electrode behavior. Thus, the potential remains unchanged with the passage of a small current [190]. The potentials of the electrode and the electrolyte solution are equal, *i.e.*, in thermodynamic equilibrium. Well-defined reference electrodes for non-aqueous batteries are difficult to prepare and stabilize. For this reason, quasi-reference electrodes (QREs) are implemented. According to Bard and Faulkner [178], QREs are metal wires used with the presumption that the potential remains stable during electrochemical measurements. Commonly used QREs are the metal Ag and platinum (Pt). The potential of QREs varies along the change of their surface condition, which could result from the reaction with electrolytes, dissolution in the electrolyte, or polarization [191]. Thus a calibration of QRE's potential against a reliable internal reference electrode or reference redox system is a prerequisite. One of the most employed internal standards is cobaltocene/cobaltocenium ion ( $Cc/Cc^+$ ) [192].

### 3.1.8 Separator

The separator is a microporous membrane that physically separates the positive electrode and negative electrodes to prevent short circuits while simultaneously allowing ions to pass between the electrodes. The most common separator for LIBs is a porous polymeric membrane (*e.g.*, Celgard separator made out of polypropylene membrane (PP)). Other types are nonwoven mats and composite separators. In lab-scale environments, glass fiber separators are typically used as well. On the one hand, thinner separators have lower resistance and increase the energy and power density of the battery while decreasing the safety factor at the same time. On the other hand, thicker separators provide a larger safety factor, but the high resistance may negatively affect the batteries' performance. Consequently, the thickness and the porosity of the separator is a trade-off between performance and safety.

## 3.2 Experimental

### 3.2.1 NiAl LDH electrode on LIBs

#### Preparation of NiAl LDH

NiAl LDH was obtained by a facile and straightforward one-pot hydrothermal reaction. All reagents (aluminum nitrate nonahydrate ( $\text{Al}(\text{NO}_3)_3 \cdot 9\text{H}_2\text{O}$ ), nickel nitrate hexahydrate ( $\text{Ni}(\text{NO}_3)_2 \cdot 6\text{H}_2\text{O}$ ) and urea ( $\text{CO}(\text{NH}_2)_2$ ) provided by Sigma-Aldrich) were of analytical purity and were directly used without further purification. By following the procedure in the report [193], a solution has been prepared by dissolving 30 mmol of  $\text{Ni}(\text{NO}_3)_2 \cdot 6\text{H}_2\text{O}$ , 45 mmol of urea and 15 mmol of  $\text{Al}(\text{NO}_3)_3 \cdot 9\text{H}_2\text{O}$  (a Ni:Al ratio of 2:1) in 150 mL of deionized water. This solution was then transferred into a Teflon-lined stainless steel autoclave of 200 mL capacity at a temperature of  $100^\circ\text{C}$ . After a 24 h of hydrothermal process, the product was filtered and washed with water and ethanol several times. The NiAl LDH was finally obtained by drying the product in an oven for overnight at  $70^\circ\text{C}$ .

### Structural and physical characterization

The X-ray diffraction patterns were collected using STOE STADI P X-ray powder diffractometers equipped with Mythen1K detectors with  $\text{Mo K}\alpha_1$  radiation ( $\lambda = 0.70930 \text{ \AA}$ ). The diffraction pattern was refined by full-profile Rietveld, using the software package WinPLOTR [194]. The instrument used for the field emission scanning electron microscope (FE-SEM) characterization was a ZEISS SUPRA 40 VP. FT-IR spectroscopy was performed using a Spectrum 65 FT-IR Spectrometer (PerkinElmer, Waltham, MA, USA) equipped with a KBr beamsplitter and a DTGS detector by using an ATR accessory with a diamond crystal; the spectra were recorded from  $4000 \text{ cm}^{-1}$  to  $500 \text{ cm}^{-1}$ .

The XPS was acquired using a Thermo Fischer Scientific K-alpha spectrometer. The samples were analyzed using a micro-focused, monochromated  $\text{Al K}\alpha$  X-ray source (1486.6 eV,  $400 \mu\text{m}$  spot size). XPS spectra were recorded with a concentric hemispherical analyzer at the pass energy of 50 eV and fit with one or more Voigt profiles (binding energy uncertainty:  $\pm 0.2 \text{ eV}$ ). Scofield sensitivity factors were applied for quantification using the Avantage software package [195]. On the electrode samples, all spectra were referenced to the  $\text{CF}_2$  component originating from the PVDF binder centered at 290.7 eV binding energy. Regarding the NiAl LDH-SA sample, the spectral calibration was done on C1s peak (C–C, C–H) at 285.0 eV binding energy controlled utilizing the photoelectron peaks of metallic Cu, Ag, and Au, respectively. X-ray absorption near-edge structure (XANES) and extended X-ray absorption fine structure (EXAFS) spectra for the Ni K-edge of the samples with the different state of charge were conducted on the P65 beamline,

PETRA III, German Electron Synchrotron in Hamburg (DESY). XAS spectra were collected at Ni K-edge in transmission geometry with the continuous-scan mode. The double-crystal fixed-exit monochromator was equipped with Si(111) crystals. *Ex situ* samples for XAS measurements were obtained by applying a constant potential to equilibrate the system after the desired potential is reached.

### **Electrode preparation and electrochemical tests**

NiAl LDH electrode has been prepared as follows: 70 wt% of the as-prepared NiAl LDH was mixed by stirring in a quartz mortar for 10 minutes with 20 wt% conductive carbon black (TIMCAL® Super C65) and 10 wt% of binder in the appropriate solvent. For comparison, PVDF (R6020/1001, Solvay) and SA (Sigma-Aldrich) were chosen as the binders. The solvents used to dissolve PVDF and SA were NMP and 9:1 water/isopropanol, respectively. The blended slurries were then coated on a 10  $\mu\text{m}$  thick copper foil current collector with a wet thickness of  $\sim 110 \mu\text{m}$ , followed by drying in an oven at  $80^\circ\text{C}$  for 12 h. After that, the coated electrodes were cut into individual discs of 12 mm diameter with  $\sim 0.7 \text{ mg}$  mass loading of NiAl LDH. The electrodes with different binders are denoted as NiAl LDH-SA and NiAl LDH-PVDF, respectively. CR2032 coin cells were built in an argon-filled glovebox (MB200, MBraun GmbH,  $\text{O}_2$  and  $\text{H}_2\text{O} \leq 0.5 \text{ ppm}$ ) consisting of the as-prepared working electrode, a lithium foil counter electrode (15 mm diameter, Alfa Aesar), a glass fiber separator (Whatman glass microfiber filter,  $675 \mu\text{m}$  thickness) and LP30 electrolyte (1 M  $\text{LiPF}_6$  in EC/DMC (in a volume ratio of 1:1), BASF). The electrochemical tests (galvanostatic charge-discharge (GCD) and cyclic voltammetry (CV) were carried out on a VMP3 multichannel potentiostat (Bio-Logic Science Instrument, France) equipped with EC-Lab software. The electrochemical cells were kept in a BINDER climate chamber at  $25^\circ\text{C}$  during the electrochemical experiments. Two potential ranges (0.01-3.0 V and 0.4-3.0 V vs.  $\text{Li}^+/\text{Li}$ ) were employed for GCD and CV tests.

### **3.2.2 NiAl LDH electrodes on DIBs**

#### **Structural and physical characterization**

The morphology of the LDH samples was observed by a scanning electron microscope (SEM, Zeiss Merlin) with an acceleration voltage of 10 keV. The coupled energy-dispersive X-ray (EDX) analysis was conducted at a Quantax 400 system from Bruker.

Magnetic properties were measured using a DynaCool Physical Property Measurement System (PPMS) from Quantum Design equipped with a vibrating sample magnetometer (VSM). DC Magnetic moment vs. temperature was measured in zero-field cooled (ZFC) and field-cooled (FC) mode with 1 K resolution from 2 K to 20 K in settle mode and from 21 K to 300 K in sweep mode at a rate of 2 K/min and at magnetic field of 500 Oe. Magnetic moment vs. field was measured at 2, 10 and 300 K with the field scanned in a full loop starting from 7 T at 2 K. After measurement at 2 K the temperature was increased within the field of 7 T to next temperature of 10 K, *etc.* 6.1 mg of the  $\text{Ni}_{0.66}\text{Al}_{0.33}(\text{OH})_2(\text{NO}_3)_{0.33}\cdot 0.16\text{H}_2\text{O}$  sample ( $5.9014\cdot 10^{-5}$  mol) has been filled into polypropylene capsules for the measurements.

### Electrochemical tests

The electrochemical experiments were performed on two-electrode Swagelok-type cells. NiAl LDH working electrodes were prepared by mixing the active material, carbon black (Super C65, Imerys Ltd.), and 5 wt% PVDF binder (R6020/1001, Solvay) in NMP (GC 99.5%, Merck KGaA) solvent in a weight ratio of 7:2:1. The blended slurry was further coated on a stainless steel current collector with a wet thickness of 110  $\mu\text{m}$ , and dried in an oven at 80°C for 12 h. Circular electrodes with a diameter of 12 mm were punched out and dried at 120°C in a vacuum oven for 24 h with average mass loading of active materials of 1-1.5 mg per electrode (0.9~1.3  $\text{mg cm}^{-2}$ ). The two-electrode Swagelok-type cells were built in an above-mentioned argon-filled glovebox consisting of NiAl LDH working electrode, a lithium foil counter electrode (CE, 12 mm diameter, Alfa Aesar), two glass fiber separators (Whatman glass microfiber filter, 675  $\mu\text{m}$  thickness per disc) and electrolyte. As comparison, two different electrolytes were investigated: 1.0 M LiTFSI with additional 0.7 M  $\text{LiNO}_3$  salt in DME solvent, and 1.0 M LiTFSI in DME, noted as LiTFSI/ $\text{LiNO}_3$ , and LiTFSI, respectively. A glass cell was built for the stability window test of the LiTFSI/ $\text{LiNO}_3$  electrolyte, where two metallic Li stripes work as both reference electrode and counter electrode, and a glassy carbon works as the working electrode.

The cells were kept in a climate chamber (BINDER) at 25°C for electrochemical experiments (GCD and CV), which were conducted on a multichannel potentiostat (VMP3, Bio-Logic). Different potential ranges (0.7–3.0 V, 0.7–4.0 V and 0.7–4.5 V vs.  $\text{Li}^+/\text{Li}$ ) were employed for GCD and CV tests, respectively.

### 3.2.3 NiAl LDH electrode on CIBs

#### Electrode preparation

A homogenous slurry of a mixture of NiAl LDH active material, carbon black, and PVDF binder (the 5 wt% PVDF binder was prepared by dissolving PVDF (R6020/1001, Solvay) in NMP (GC 99.5%, Merck KGaA)) in a ratio of 7:2:1 was prepared using Speedmixer (Hauschild SpeedMixer® DAC 150.1 FVZ) at 850 rpm for 5 min. The as-prepared slurry was then coated with a wet thickness of 130  $\mu\text{m}$  on a 15  $\mu\text{m}$ -thickness stainless steel foil current collector; after drying in the fume hood overnight, the electrodes were transferred into the oven for further drying at 120°C for 8 hours. The dried slurry was punched into 12 mm diameter discs (GELON GROUP, manual punching machine, GN-CP20), which were then used as electrodes and transferred into a glass oven (Büchi Glass oven B585) under vacuum for drying at 120°C overnight. The electrodes have an average mass loading of 1.65 g cm<sup>-2</sup> and a final thickness after drying of ~0.95  $\mu\text{m}$ . The dried electrodes were subsequently transferred into the above-mentioned argon-filled glovebox for cell assembly.

A 0.5 mol L<sup>-1</sup> electrolyte of Bpy<sub>14</sub>Cl (99%, Sigma-Aldrich) in PC (99.7%, Sigma-Aldrich) was prepared in the argon-filled glovebox and magnetically stirred for 24 hours for further use, denoted as Bpy<sub>14</sub>Cl/PC.

#### Electrochemical tests

The electrochemical experiments were performed on two-electrode Swagelok-type cells. NiAl LDH working electrodes were prepared by mixing the active material, carbon black (Super C65, Imerys Ltd.). The cell assembly was conducted in an above-mentioned argon-filled glovebox. For the electrochemical stability window test of electrolyte, a TSC 1600 Closed-cell (rhd instruments GmbH & Co. KG) was used, which contains a glassy carbon as WE, two Pt-wires as counter and reference electrodes, separately. For the GCD and CV measurements, the cells were built using two-electrode Swagelok cell configurations. The two-electrode Swagelok cell consists of Li as the counter electrode, separator (Whatman® glass microfiber filter, Grade GF/D, 0.67 mm thickness), electrolyte (300  $\mu\text{L}$ ), and the working electrode. The cells were kept in a climate chamber (BINDER) at 25°C for electrochemical experiments (GCD and CV), which were conducted on a

multichannel potentiostat (VMP3, Bio-Logic Science Instrument, France). A potential range (1.0–3.0 V *vs.* Li) was employed for GCD and CV tests, respectively.

## 4 Electrochemical study of NiAl LDH as negative electrode material for LIBs

### 4.1 Morphology and structure characterization

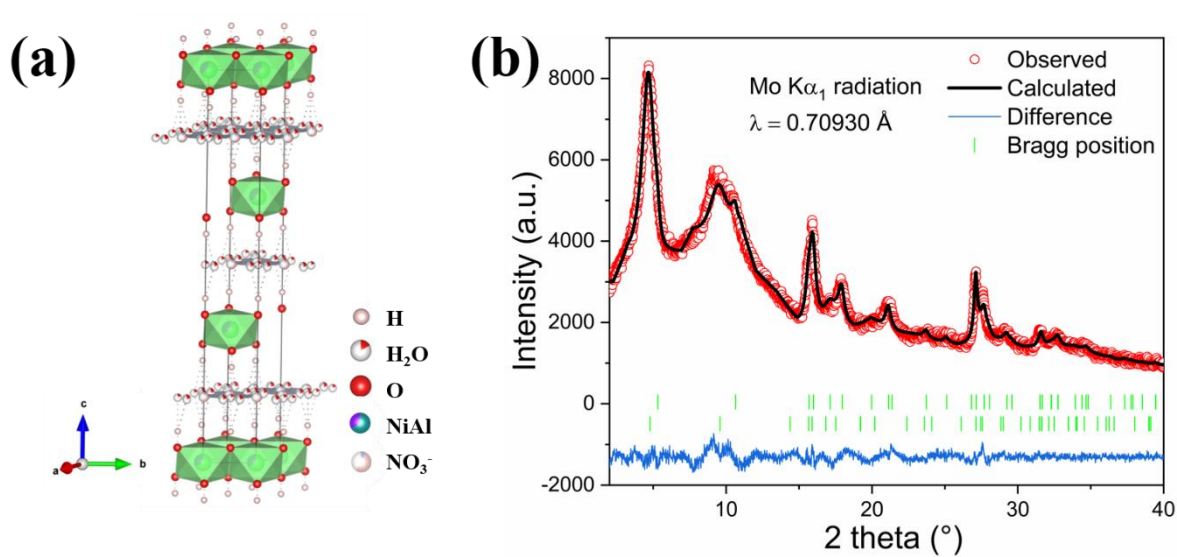


**Figure 4.1.** a) Crystal structure of NiAl LDH (one unit cell, constructed by Vesta software) and b) Observed and calculated diffraction patterns after Rietveld refinement of the hydrotalcite structure model.

The as-prepared NiAl LDH was characterized by XRD (**Figure 4.1**), and the diffraction data analysis was carried out by the Rietveld method using the Fullprof software package. The XRD reflections of NiAl LDH can be indexed using a unit cell of hydrotalcite (ICSD 81963). The XRD reflections show a slight phase separation of NiAl LDH with the rhombohedral R-3m space group. With Bragg's law, the interplanar distance  $d_{003}$  can be calculated. A large interplanar distance can provide more space for anions in the structure of NiAl LDH. The  $d_{003}$  spacing is 8.48 Å and the  $c$ -parameter of the LDH unit cell is  $c = 25.490$  Å. The  $d$  distance was calculated from the Bragg position of the prevailing phase (80 w/w %).

The FT-IR spectrum is shown in **Figure A 1 a**. The broad absorption band at  $3433\text{ cm}^{-1}$  can be attributed to the O-H stretching vibrations of the hydroxyl groups and the presence of water molecules in the interlayer of LDH [196]. Specifically, the interlayered lattice water is hydrogen-bonded to the transition metal slabs [197][198]. It is expected that during delithiation, the crystal water molecules remain in the interlayer space [199][200]. The weak peak at  $1637\text{ cm}^{-1}$  is ascribed to the vibrations of the in-plane bending mode of water molecules. The sharp characteristic absorption band at  $1352\text{ cm}^{-1}$  corresponds to the stretching vibration mode of  $\text{NO}_3^-$ , which confirms the absorption of  $\text{NO}_3^-$  in the interlayer of NiAl LDH materials. The bands at  $769$  and  $621\text{ cm}^{-1}$  are due to the stretching and bending modes of Al-OH and Ni-OH, respectively. XRD and FT-IR spectra demonstrate the successful synthesis of NiAl LDH with  $\text{NO}_3^-$  in the interlayer. Based on the thermogravimetric curve (**Figure A 1 b**) and the feeding molar ratio of  $\text{Ni}(\text{NO}_3)_2 \cdot 6\text{H}_2\text{O}$  and  $\text{Al}(\text{NO}_3)_3 \cdot 9\text{H}_2\text{O}$  (with a Ni:Al ratio of 2:1), the molecular formula of the as-prepared NiAl LDH expected to be  $[\text{Ni}_{1-x}\text{Al}_x(\text{OH})_2]^{x+}(\text{NO}_3^-)_x \cdot m\text{H}_2\text{O}$  with  $m=0.16$  and  $x \approx 0.33$ .

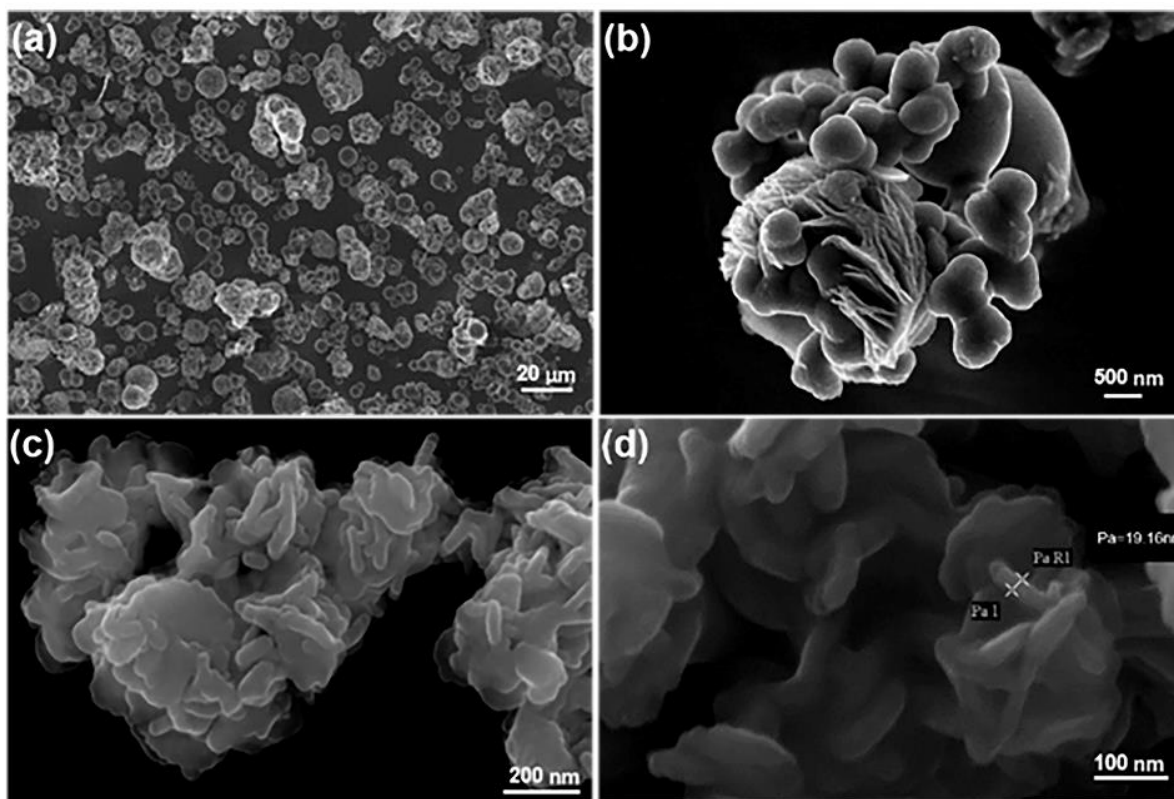


**Figure 4.2** FE-SEM micrographs of NiAl LDH. a) overview; b) low magnification image; c) and d) high magnification images.

The morphology of NiAl LDH was characterized *via* FE-SEM, which is shown in **Figure 4.2**. The homogeneously dispersed cluster of lamellae with 10-30  $\mu\text{m}$  of diameter can be observed on the image at low magnification (**Figure 4.2 a**). The higher magnification image (**Figure 4.2 c**) shows that the NiAl LDH lamellae cluster has a flower-like structure arranged in a concentric form and it is highly nano-crystallized. Besides, a thickness of the NiAl LDH lamellae ranging from 20 nm to 40 nm can be observed in **Figure 4.2 d**. Furthermore, nitrogen ( $\text{N}_2$ ) isotherms of NiAl LDH have been performed to determine the surface area and pore size. The BET-specific surface area of NiAl LDH is  $46.85 \text{ m}^2 \text{ g}^{-1}$ , and the average pore diameter is around 8.54 nm (**Figure A 2**).

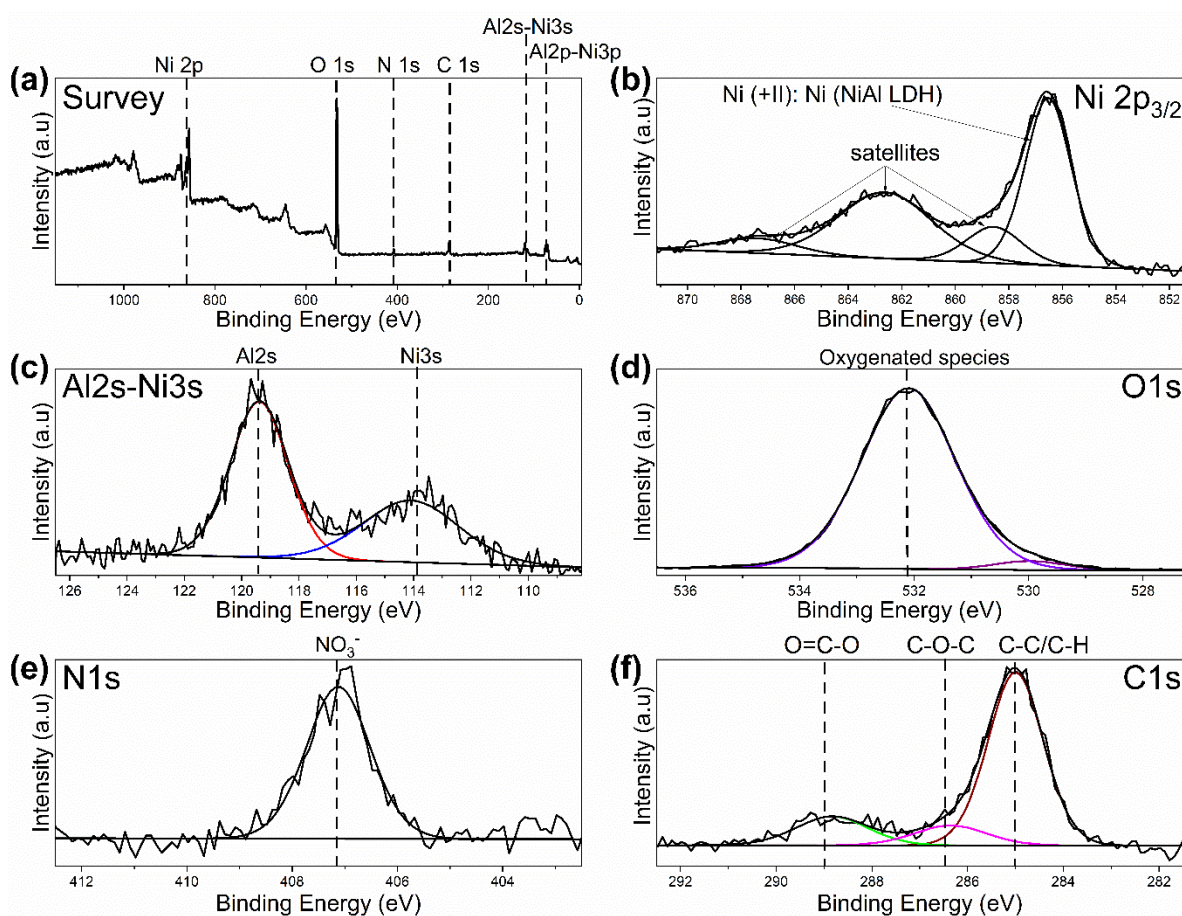


**Figure 4.3.** XPS spectra: a) survey of NiAl LDH; b) Ni2p<sub>3/2</sub>; c) Al2s, d) O1s; e) N1s and f) C1s.

The surface electronic state of NiAl LDH materials is illustrated by XPS, as shown in **Figure 4.3**. Survey X-ray photoelectron spectrum reveals the presence of nickel (Ni2p, Ni3p or Ni3s), aluminum (Al2s or Al2p), oxygen (O1s), nitrogen (N1s) and carbon (C1s). High-resolution XPS spectra of Ni2p<sub>3/2</sub>, Al2s, O1s, N1s and C1s are shown in **Figure 4.3 b-f**. The peak of Ni2p<sub>3/2</sub> located at 856.3 eV with its shake-up satellites, as shown in **Figure 4.3 b**, is a signature of various Ni (+II) species in NiAl LDHs [201][202]. The Al2s-Ni3s spectrum shows two peaks centered at 114.1 eV and 119.7 eV (**Figure 4.3 c**), which are signatures of Ni and Al chemical environments. The peak positions of these atoms are the signature of Ni<sup>2+</sup> and Al<sup>3+</sup> environments in the crystal structure of NiAl LDH material [203]. The O1s spectrum (**Figure 4.3 d**) shows signals coming from all oxygenated species at the surface. The prominent oxygen peak at 532 eV corresponds to a mix of oxygen from NiAl LDH structure and other oxygenated species from surface contamination environments (CO and COO groups) [204]. The XPS analysis demonstrates that the Ni<sup>2+</sup> and Al<sup>3+</sup> elements coexist in the product, which is in good accordance with the prediction. Concerning the C1s spectrum, three peaks are presented. The main peak on C1s spectrum at 285.0 eV corresponds to hydrocarbon contamination. The peaks centered at 286.5 eV and 288.5 eV correspond, respectively, to mono- and bi-oxygenated carbon environments. Carbon species come from surface contamination of NiAl with the air environment. N1s (**Figure 4.3 e**) spectra display one peak at 407.1 eV, corresponding to nitrate (NO<sub>3</sub><sup>-</sup>) present in the interlayer of NiAl LDHs material. The XPS analysis of the prepared NiAl LDH material determines the atoms' chemical environments present in the crystalline structure and it agrees with the FT-IR and XRD measurements made on the material.

## 4.2 Electrochemical characterization

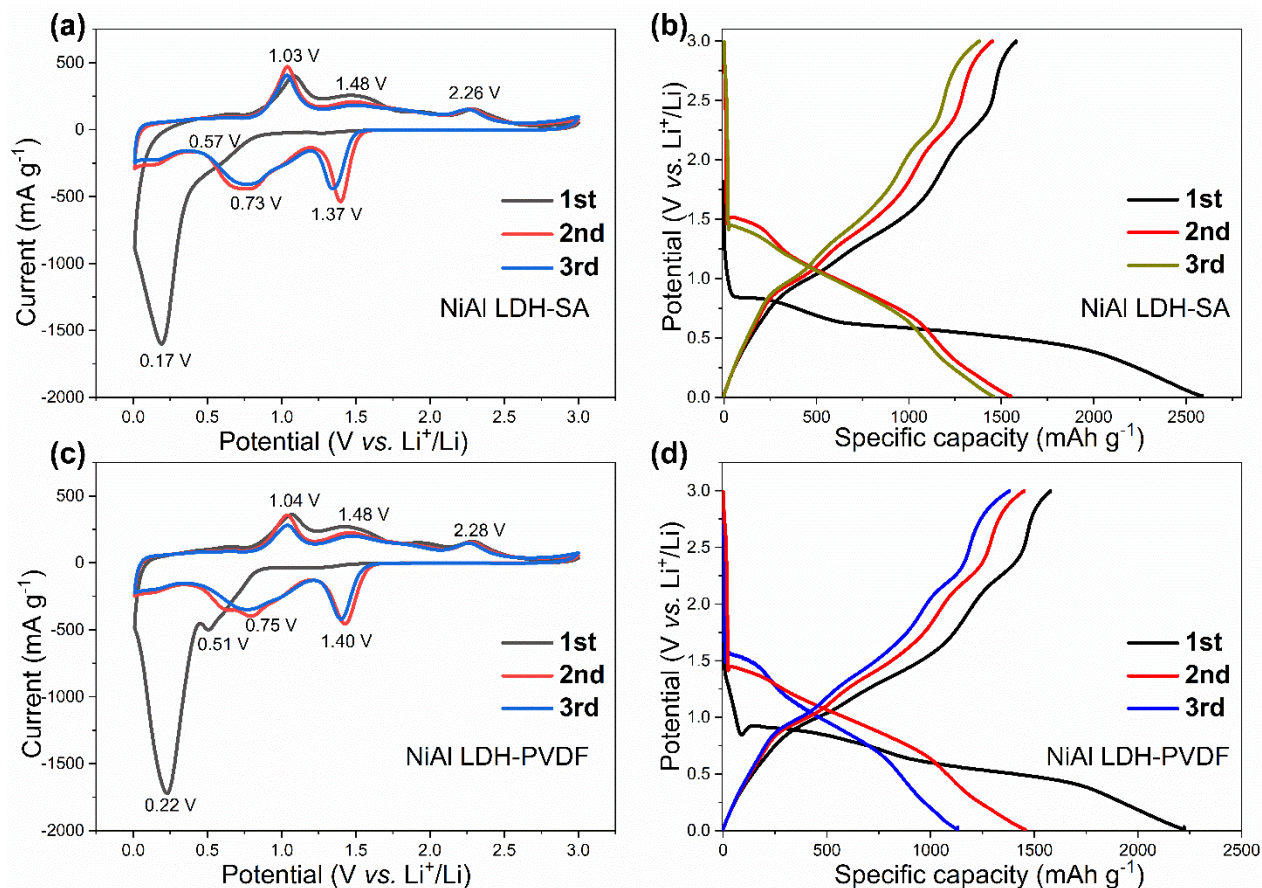


**Figure 4.4.** Electrochemical characterization of NiAl LDH based on different binders at the potential window of 0.01-3.0 V vs. Li<sup>+</sup>/Li. a) CV curves at 0.1 mV s<sup>-1</sup> on the NiAl LDH-SA electrode; b) GCD profiles at 0.05 A g<sup>-1</sup> of NiAl LDH-SA electrode; c) CV curves at 0.1 mV s<sup>-1</sup> on the NiAl LDH-PVDF electrode; d) GCD profiles at 0.05 A g<sup>-1</sup> of the NiAl LDH-PVDF electrode.

The NiAl LDH composite electrodes based on the two binders (SA and PVDF) have been characterized *via* CV and GCD. **Figure 4.4 a** displays the CV curves of NiAl LDH-SA electrode at 0.1 mV s<sup>-1</sup> in the potential window of 0.01-3.0 V (vs. Li<sup>+</sup>/Li). In the first cycle, the weak and broad peak located at 0.57 V is due to the reduction of the intermediate product LiOH into Li<sub>2</sub>O and probably LiH [205]. The well-defined cathodic peak that appears at 0.17 V can be ascribed to

the formation of the solid electrolyte interphase (SEI) films on the surface of NiAl LDH electrode originating from the electrolyte decomposition. During the anodic sweeps, the peak at 1.03 V is due to the oxidation of LiH into LiOH [206]. The anodic peaks located at 1.48 and 2.26 V could be attributed to the decomposition of SEI, as well as the oxidation of metallic Ni<sup>0</sup> to Ni<sup>2+</sup> [207]. In addition, the presence of cathodic peaks at 0.73 V and 1.37 V after the first cycle indicates an irreversible structural or textural transformation, which occurs during the first lithiation [208]. It's worth noting that the CV sweep of the third cycle can be well overlapped with that of the second cycle, implying reversible electrochemical reactions in the process of lithiation/delithiation after the first cycle.

The galvanostatic charge-discharge performance of NiAl LDH electrode with SA binder at a specific current of 50 mA g<sup>-1</sup> in the potential range of 0.01–3.0 V (vs. Li<sup>+</sup>/Li) is shown in **Figure 4.4 b**. In the first lithiation curve, the long plateau at around 0.51–0.57 V is in agreement with the initial cathodic peak at approximately 0.57 V observed in the CV curve. Three sloped plateaus can be observed in the first delithiation profile, corresponding to the anodic peaks observed in the CV curve. The NiAl LDH-SA electrode delivers 2586 and 1578 mAh g<sup>-1</sup> for the first lithiation and delithiation, respectively, indicating an initial Coulombic efficiency (ICE) of 61.3%. This low ICE is due to the irreversible decomposition of the electrolyte and the formation of the SEI layer on the surface of the active material. From the second discharge profile, two discharge plateaus at around 1.49 V and 0.85 V emerge, corresponding to the cathodic peaks related to the reduction of Ni<sup>2+</sup> and LiOH in the CV curves, respectively. Besides, three charge plateaus located at approximately 0.92 V, 1.46 V and 2.22 V in the second charge profile agree well with the anodic peaks in the CV curves. Despite the capacity loss in the first cycles, a high reversible capacity of around 1500 mAh g<sup>-1</sup> is achieved in the subsequent processes.

**Figure 4.4 c-d** show the electrochemical features of the NiAl LDH electrode based on the PVDF binder, which is the most widely used binder in commercial electrodes for LIBs. Similar to the results shown in **Figure 4.4 a**, in **Figure 4.4 c**, the cathodic peaks at 0.51 V and 0.22 V are due to the transformation of LiOH/LiH and Ni<sup>2+</sup>/Ni<sup>0</sup>, respectively. The cathodic peak at 0.22 V also includes the electrochemical reduction of the electrolyte with the formation of the SEI film. In the anodic sweeps, the peaks centered at 1.04, 1.45 and 2.28 V are well-overlapped with that of the first cycle and can be assigned to the reversible conversion process of LiH/LiOH and Ni<sup>0</sup>/Ni<sup>2+</sup>, respectively.

As shown in **Figure 4.4 d**, when the PVDF binder is utilized in the NiAl LDH electrode, the initial discharge and charge capacities of 2221 and 1577 mAh g<sup>-1</sup> are achieved, corresponding to an initial Coulombic efficiency of 71.0%, which is higher than what obtained with the NiAl LDH-SA electrode. During the following charge process, the decomposition of the SEI film can be responsible for the rapid capacity decay of the electrode based on both binders, as reported in the literature [209]. Although the NiAl LDH-PVDF electrode delivers comparative capacity as the NiAl LDH-SA in the first and second cycles, it presents a dramatic decay in the third cycle, suggesting inferior charge-discharge stability.

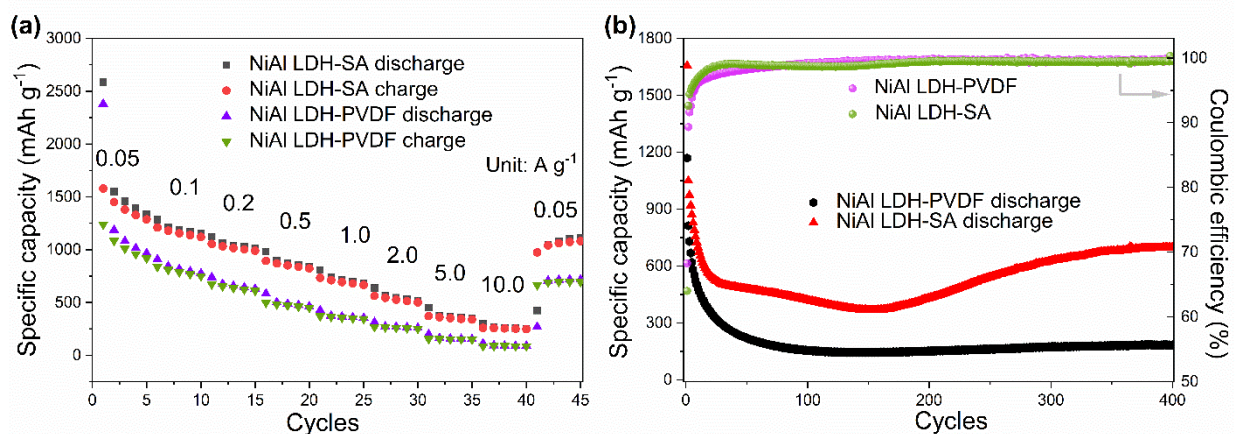


**Figure 4.5.** Electrochemical performance of NiAl LDH with different binders at a potential window of 0.01–3.0 V for a) rate performance, and b) cycle performance and Coulombic efficiency at a current density of 0.5 A g<sup>-1</sup>.

The rate capability test was performed with currents ranging from 0.05 to 10.0 A g<sup>-1</sup>, as shown in **Figure 4.5 a**. The NiAl LDH-SA electrode delivers average discharge capacities of 1665, 1201 and 1051 mAh g<sup>-1</sup> at 0.05, 0.1 and 0.2 A g<sup>-1</sup>, respectively. When using PVDF as a binder, the average discharge capacities at the same currents are 1324, 827 and 668 mAh g<sup>-1</sup>, respectively, significantly lower than those of the electrode with SA binder. Furthermore, the NiAl LDH-SA electrode recovers to a high reversible capacity of 1109 mAh g<sup>-1</sup> when the current reverses back to 0.05 A g<sup>-1</sup>. This value is higher than the recovered capacity of 715 mAh g<sup>-1</sup> obtained with the NiAl LDH-PVDF electrode, indicating that the NiAl LDH-SA electrode is more stable and can

better withstand high currents. **Figure 4.5 b** depicts the cyclic performance of the two electrodes. It is worth noting that after a significant capacity decay during the first 154 cycles, the capacities of the NiAl LDH-SA electrode increase gradually. After 400 cycles, the electrode can still retain a high reversible capacity of  $697 \text{ mAh g}^{-1}$  at the current of  $0.5 \text{ A g}^{-1}$ . Both electrodes reach nearly 100% of Coulombic efficiency after the initial cycles, confirming the excellent reversibility of NiAl LDH and the absence of side reactions after the formation of the SEI.

The long cycling performance of the NiAl LDH electrodes in the potential range of 0.01–3.0 V at the high specific current of  $1.0 \text{ A g}^{-1}$  has been further evaluated and shown in **Figure A 3**. A similar high initial discharge capacity ( $1405 \text{ mAh g}^{-1}$ ) is achieved by both electrodes (independently from the binder). After undergoing a capacity decay for 170 cycles, the NiAl LDH-SA electrode starts a period of capacity increase. Stable long-term cycling has been achieved with a capacity of  $388 \text{ mAh g}^{-1}$  after 1400 cycles. On the other side, the NiAl LDH-PVDF electrode shows an irreversible capacity fading after 65 cycles, with poor long cycling performance.

### 4.3 Li-ion storage mechanism in NiAl LDH electrode

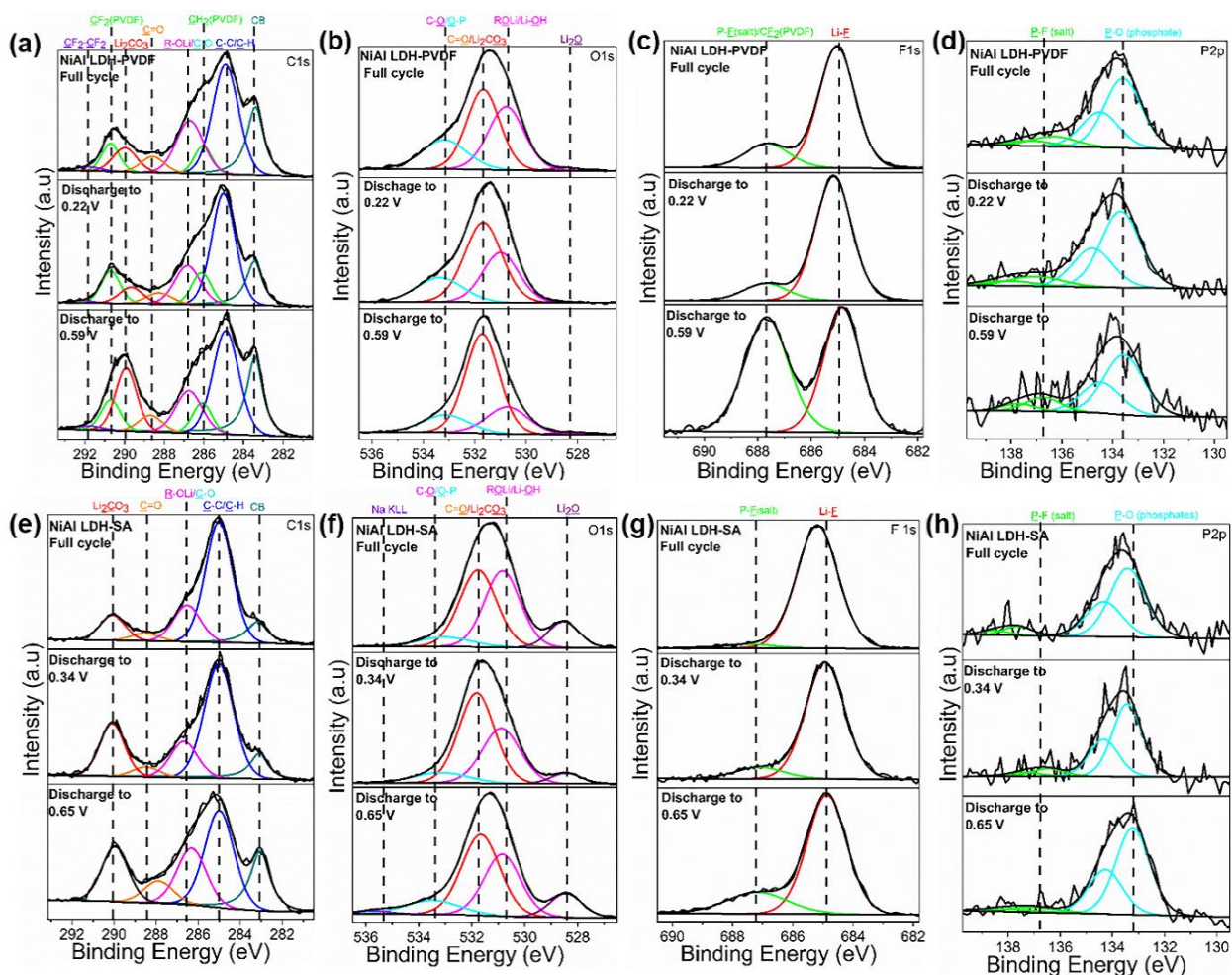


**Figure 4.6.** a) C1s, b) O1s, c) F1s and d) P2p X-ray photoelectron spectra of NiAl LDH-PVDF electrode discharged to 0.59 V, 0.22 V and charged to 3.0 V (1 cycle) respectively; e) C1s, f) O1s, g) F1s and h) P2p XPS spectra of NiAl LDH-SA electrode discharged to 0.65 V, 0.34 V and charged to 3.0 V (1 cycle), respectively.

To better understand the influence of binders and reactivity of NiAl LDH electrodes on the electrochemical response, we performed XPS analysis. C1s, F1s, O1s, P2p X-ray photoelectron spectra are presented in **Figure 4.6**. O1s spectra collect signals coming from all oxygenated species present on the NiAl LDH-PVDF samples. **Figure 4.6 (b and f)** reveals one peak centered at around

531.5 eV, which is characteristic of the mix of O=C and Li<sub>2</sub>CO<sub>3</sub> components in the battery system with DMC as the solvent. Three additional elements center at 530.3 eV (the combination of lithium alkylates (ROLi) and LiOH), 533.6 eV (O–C and P–O environments), and 528.5 eV (attributed to O<sup>2-</sup> anions from Li<sub>2</sub>O component) are presented in the spectra, respectively. Another peak that appears at 537.8 eV is assigned to Na KLL-Auger from sodium present in the SA binder, which is always present in O1s spectra of sodium-based samples.

**Figure 4.6 c** and **g** show the spectra of F1s, one component located at 685.0 eV confirming the presence of LiF (on all cycled electrode samples), and the other situated at around 687.1 eV indicating the presence of P–F component from LiPF<sub>6</sub> and CF<sub>2</sub>–CH<sub>2</sub> component from PVDF (only present on NiAl LDH-PVDF samples). Besides, P2p spectra (**Figure 4.6 d** and **h**) have to be fitted with 2p<sub>3/2</sub>-2p<sub>1/2</sub> doublets separated by 0.9 eV with 2:1 intensity ratio due to spin-orbit coupling. The main doublet with P2p<sub>3/2</sub> component located at 133.6 eV is the phosphates signal from the decomposition of LiPF<sub>6</sub>, and the other at around 137.0 eV corresponds to the phosphorus from LiPF<sub>6</sub>.

The C1s spectra (**Figure 4.6 a** and **e**) comprise one component (located at 283.3 eV) characteristic of the carbon black (CB). The three components at 286.2 eV (attributed to the CH<sub>2</sub> chemical environment in PVDF binder), 290.7 eV (CF<sub>2</sub>–CH<sub>2</sub>) and 291.8 eV (CF<sub>2</sub>–CF<sub>2</sub>) confirm the presence of the PVDF binder on the surface of the electrode [210]. The four other components at 285 eV (C–C/C–H), 286.8 eV (mix of C–O/ROLi) [211], 288.5 eV (C=O) and 290.1 eV (attributed to the Li<sub>2</sub>CO<sub>3</sub> chemical environment) are due to the degradation products of the electrolyte which are composing the SEI. These components remain on the electrodes during electrochemical measurements. For the NiAl LDH-PVDF electrode, the intensity of the components attributed to CB slightly increases after discharging to 0.22 V, indicating the thinning down of the SEI film. While for the NiAl LDH-SA electrode, the CB components' decreases, suggesting a thicker up of the SEI. The change of C1s spectra after the full cycle reveals a thicker SEI formation on the NiAl LDH-SA electrode. This difference may be due to the gelation derived from a stronger interaction of PVDF binder and electrolyte, which hinders the further formation of SEI film [212].

XPS analysis of NiAl LDH after cycling confirms a similar SEI composition for the electrode with both binders. The species of Li<sub>2</sub>O (from NiAl LDH-SA samples), LiF, a mix of ROLi/LiOH,

$\text{Li}_2\text{CO}_3$  and phosphates, which are decomposition products of electrolyte during cycling, are detected with XPS on all samples. Furthermore, compared with the NiAl LDH-PVDF electrode, a less amount of LiF and a higher amount of oxygen (from oxidized species) on the NiAl LDH-SA electrode surface are found, which suggests a higher electrolyte degradation when SA is used as the binder. **Table A 2** and **Figure A 4** show the binders influence on the concentration of the species that make up the SEI film. The use of PVDF as a binder on the electrode can promote the LiF formation, which is found in less amount on the NiAl LDH-SA electrode. In comparison, the SA binder facilitates the lithium oxide formation, such as  $\text{Li}_2\text{O}$ ,  $\text{ROLi}$ , and  $\text{LiOH}$ . Moreover, the quantity of these species remains stable during the first full cycle. The lower solubility of lithium oxide respect to LiF in carbonate electrolytes brings about a stable SEI film [213]. As a result, the stable lithium oxide component in SEI film could be a dominant source of negative electrode passivation. The thicker and stable SEI film detected when using SA as binder might be the reason for the higher irreversible capacity at the first cycle and for the better cycling stability as compared to the PVDF-based electrode.

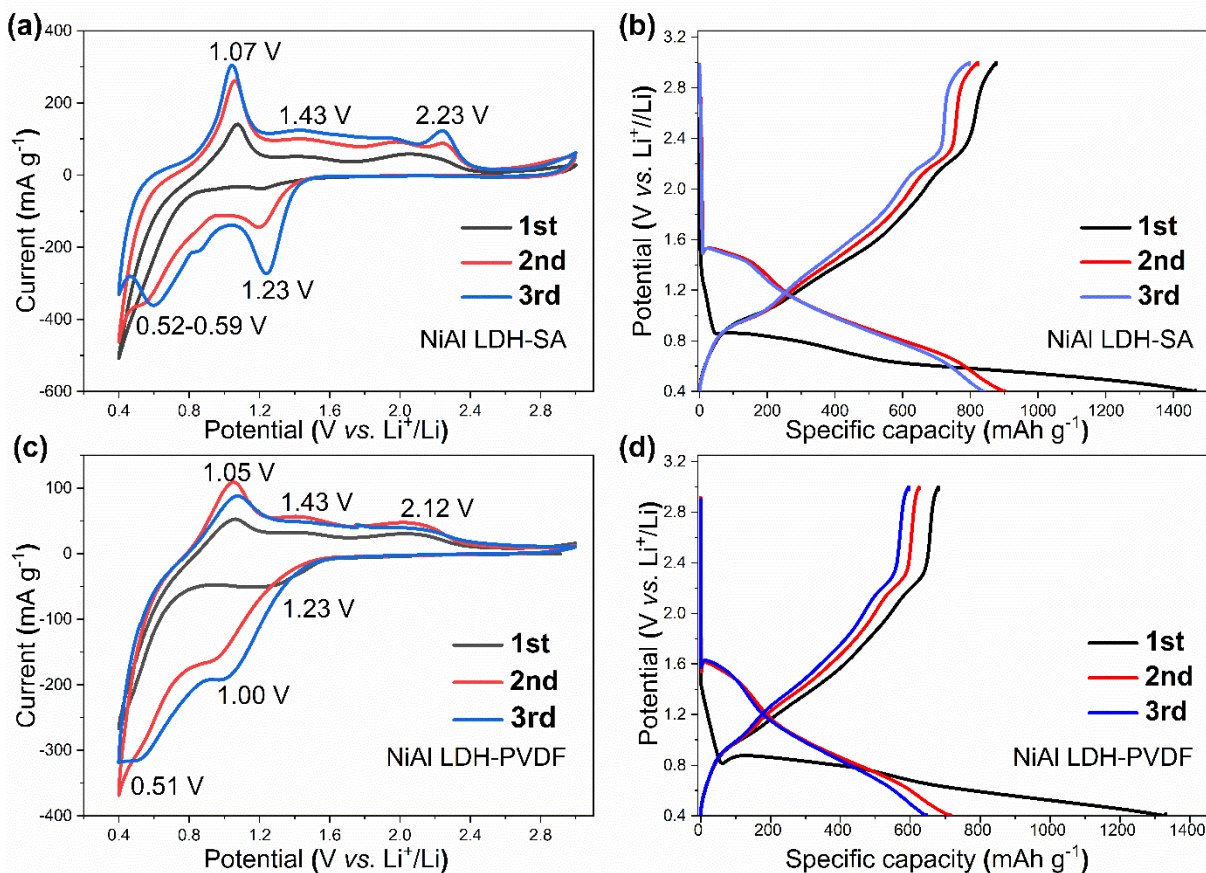


**Figure 4.7.** Electrochemical performance of NiAl LDH with different binders in the potential range of 0.4–3.0 V (vs.  $\text{Li}^+/\text{Li}$ ). a) CV curves at a scan rate of  $0.1 \text{ mV s}^{-1}$  for NiAl LDH-SA electrode; b) GCD curves at a current density of  $0.05 \text{ A g}^{-1}$  for NiAl LDH-SA electrode; c) CV curves at a scan rate of  $0.1 \text{ mV s}^{-1}$  for NiAl LDH-PVDF electrode and, d) GCD curves at a current density of  $0.05 \text{ A g}^{-1}$  for NiAl LDH-PVDF electrode.

According to recent reports [214][215][216][217], the potential discharge cut-off can influence cycling stability. Indeed, a higher potential discharge cut-off can prevent the complete reduction of  $\text{Ni}^{2+}$  to  $\text{Ni}^0$  and result in a different SEI. **Figure 4.7** and **Figure A 5** report the CV and GCD curves recorded on the two electrodes in the potential range 0.4–3.0 V (vs.  $\text{Li}^+/\text{Li}$ ). The NiAl LDH-SA and NiAl LDH-PVDF electrodes show similar CV shapes during the first cycle (black curves in **Figure 4.7 a** and **c**). A weak peak at 1.23 V can be observed during lithiation, which is attributed

to the reduction of  $\text{Ni}^{2+}$  to  $\text{Ni}^0$  and the simultaneous intercalation of  $\text{Li}^+$ , which will be explicated in the following investigation. This peak strengths during the following cycles, suggesting the domination of the  $\text{Ni}^0/\text{Ni}^{2+}$  transformation. A distinct cathodic peak appears when discharging to about 0.60 V, suggesting the reduction of the intermediate product  $\text{LiOH}$  into  $\text{Li}_2\text{O}$  and the formation of the SEI films. The anodic peak at 1.07 V accounts for the oxidation of  $\text{Li}_2\text{O}$  into  $\text{LiOH}$  [206], and the other anodic peak at around 2.23 V can be correlated to the conversion of Ni into nickel hydroxide.

The weak anodic peak appearing at 1.43 V may be attributed to the decomposition of SEI film [218] [219]. The reduction peak at around 1.23 V of the NiAl LDH-SA electrode shows almost no shift in the following cycles (**Figure 4.7 a**). In comparison, the corresponding reduction peak of the NiAl LDH-PVDF electrode (**Figure 4.7 c**), with cycling, shifts to more negative potentials, from 1.23 V to around 1.00 V, indicating an increase in electrode polarization. [220][221].

The GCD performance of the NiAl LDH electrode based on SA and PVDF binders at 0.4–3.0 V (vs.  $\text{Li}^+/\text{Li}$ ) was further investigated (**Figure 4.7 b and d**). The initial discharge capacity of the NiAl LDH-SA electrode is  $1465 \text{ mAh g}^{-1}$ , which is higher than that of the NiAl LDH-PVDF electrode ( $1330 \text{ mAh g}^{-1}$ ). The corresponding initial Coulombic efficiencies are 60.0% and 51.1%, respectively. Besides, the SA binder-based electrode shows more well-defined lithiation and delithiation plateaus in the subsequent sweep profiles.

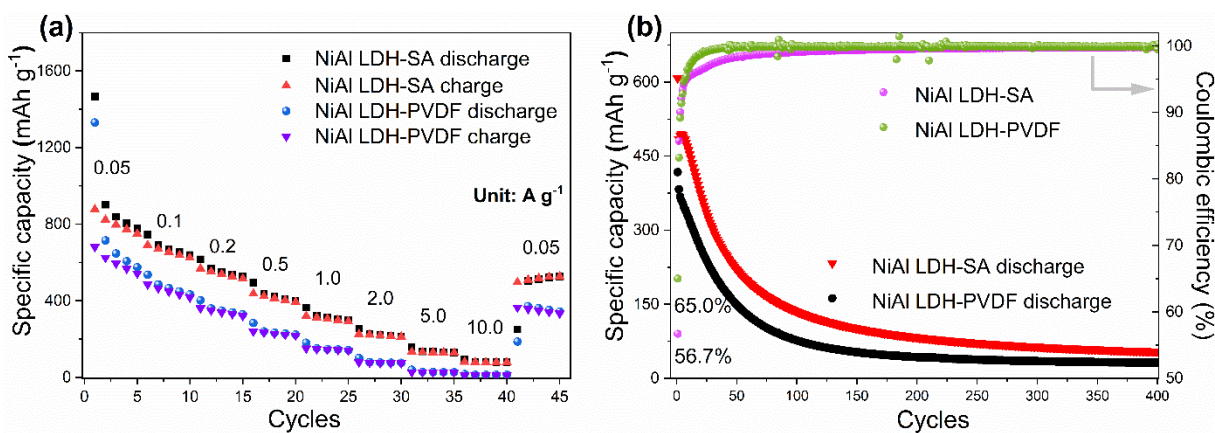


**Figure 4.8.** Electrochemical performance with different binders in the potential range of 0.4-3.0 V (vs.  $\text{Li}^+/\text{Li}$ ). a) rate capacity at different current densities of SA and PVDF-based electrodes

and; b) cycle performance and Coulombic efficiency at a current density of  $0.5 \text{ A g}^{-1}$  of NiAl LDH-SA and NiAl LDH-PVDF electrodes.

**Figure 4.8 a** shows the rate test of the NiAl LDH electrode with the two different binders at current densities from  $0.05\text{--}10.0 \text{ A g}^{-1}$ . The average discharge capacities of the NiAl LDH-SA electrode are 957, 679 and  $559 \text{ mAh g}^{-1}$  at  $0.05$ ,  $0.1$  and  $0.2 \text{ A g}^{-1}$ , respectively, and a reversible capacity of  $526 \text{ mAh g}^{-1}$  is recovered when the current rate returns to  $0.05 \text{ A g}^{-1}$  after 45 cycles, corresponding to a 58.0% of retention at  $0.2 \text{ A g}^{-1}$ . As a comparison, the NiAl LDH-PVDF electrode provides an average capacity of 774, 474 and  $356 \text{ mAh g}^{-1}$  at  $0.05$ ,  $0.1$  and  $0.2 \text{ A g}^{-1}$ , respectively, along with a lower restored capacity at  $0.05 \text{ A g}^{-1}$  after 45 cycles ( $343 \text{ mAh g}^{-1}$ ) and lower retention at  $0.2 \text{ A g}^{-1}$  (46%).

**Figure 4.8 b** shows the long-term cycling experiment on the two electrodes in the restricted potential range at  $0.5 \text{ A g}^{-1}$ . The NiAl LDH-SA electrode delivers a higher initial discharge capacity ( $607 \text{ mAh g}^{-1}$ ) and Coulombic efficiency (65.0%) than the NiAl LDH-PVDF electrode ( $417 \text{ mAh g}^{-1}$  and 56.7%, respectively). However, in the potential window  $0.4\text{--}3.0 \text{ V}$  (*vs.*  $\text{Li}^+/\text{Li}$ ), in contrast to what was obtained in the extended potential region of  $0.01\text{--}3.0 \text{ V}$  (*vs.*  $\text{Li}^+/\text{Li}$ ), both electrodes suffer from poor cycling retention ( $<10\%$  after 400 cycles). These results demonstrate that the small cut-off potential of the NiAl LDH electrode can dramatically affect the delivered capacity and cycling stability. This finding is the opposite of what was observed with another LDH composite electrode (CoFe LDH with nitrates in the interlayer) tested in  $1 \text{ M NaCF}_3\text{SO}_3/\text{Diglyme}$  on sodium-ion batteries, where the electrode at a potential window of  $0.4\text{--}3.0 \text{ V}$  (*vs.*  $\text{Na}^+/\text{Na}$ ) resulted in improved stability compared with the CoFe LDH electrode in a smaller cut-off potential ( $0.01 \text{ V vs. Na}^+/\text{Na}$ ) at  $1 \text{ A g}^{-1}$  after 200 cycles [215].

Furthermore, CV at different scan rates of NiAl LDH electrode at  $0.4\text{--}3.0 \text{ V}$  (*vs.*  $\text{Li}^+/\text{Li}$ ) was performed (**Figure A 6**) to better understand the electrochemical reaction kinetics. With increasing the scan rate, the CV shape is retained and the peak positions (**Figure A 6 a and b**) gradually change, which suggests low resistance and mild polarization [222]. Bulk ion-diffusion controlled and capacitive effect behaviors can be revealed from the equation describing the relationship of peak current ( $i$ ) and scan rate ( $v$ ) [223][224]:

$$i = av^b \quad 4.1$$

A  $b$  value of  $\sim 0.5$  indicates a diffusion-driven process, while a value  $\sim 1.0$  indicates a capacitive-controlled effect. The parameter  $b$  can be expressed as the slope of the  $\log(v)$ - $\log(i)$  plot. Regarding the SA binder-based electrode, the  $b$ -values of anodic peak 1 and peak 2 are 0.92 and 0.90, respectively (**Figure A 6 c**). The  $b$ -values of the anodic peak 1 (0.84) and cathodic peak 2 (0.85) of the PVDF binder-based electrode are consistent with that of the SA-based electrode, revealing that the intercalation of Li-ion within the NiAl LDH electrode is a surface-dominated process, independently from the binder.

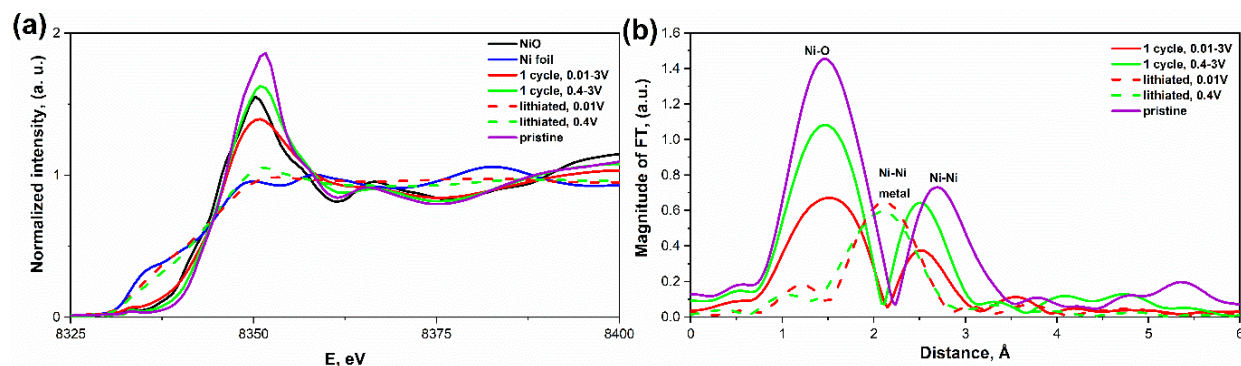
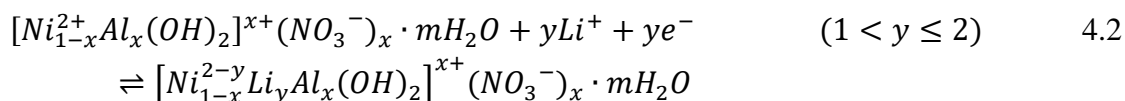


**Figure 4.9.** a) Normalized XANES spectra at Ni K-edge and, b) Fourier transform of the recorded EXAFS-spectra collected on *ex-situ* samples.

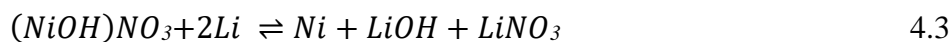
To understand the redox processes occurring on the NiAl LDH electrode during the first cycle, XAS measurements were performed on *ex-situ* samples. Normalized Ni K-edge XANES spectra and Fourier transform (FT) of the recorded EXAFS-spectra are displayed in **Figure 4.9**. The *ex-situ* samples consist of lithiated (0.4 V, 0.01 V) and delithiated (3.0 V after 0.4 V, 3.0 V after 0.01 V) NiAl LDH electrodes. The current used to bring the electrodes to the desired potential is  $0.05 \text{ A g}^{-1}$ . The Ni K-edge (**Figure 4.9 a**) of the NiAl LDH shifts to lower energies after lithiation to 0.01 V, confirming the conversion reaction  $\text{Ni}^{2+} \rightarrow \text{Ni}^0$  at this potential. According to FT-EXAFS spectra, the pristine NiAl LDH shows two distinct peaks at around 1.4 and 2.7 Å, corresponding to the 1<sup>st</sup> and 2<sup>nd</sup> Ni coordination shells in the initial structure, accordingly. The Ni metal phase is obtained when the peak corresponding to Ni-Ni band in the metal structure appears at around 2.1 Å on the FT-EXAFS spectra (sample lithiated to 0.4 V). Based on the *ex-situ* XAS and XPS measurements, by stopping the electrochemical reduction to 0.4 V the SEI is not completely

formed and the conversion reaction is only started but not completed. This can reflect the worst stability of the electrodes cycled at the cut-off potential of 0.4 V. On the other side, when the sample is discharged to the lowest potential of 0.01 V, the diffraction reflections of another product of the conversion reaction of LiOH can be recognized. Besides, the pristine NiAl LDH material does not return to the initial oxidation state after one cycle and the Ni remains slightly reduced, explaining the fast capacity loss of NiAl LDH. The mechanism of the electrochemical reaction occurring during the first cycle can be proposed as two steps process:

Intercalation (corresponding to the potential range of 3.0-0.5 V) [225]



Conversion (corresponding to the long plateau at around 0.5 V)



#### 4.4 Conclusive aspects: Li-ion storage of NiAl LDH electrode

In summary, NiAl LDH material with  $NO_3^-$  as the interlayer anion was applied as a negative electrode on lithium-ion batteries and the role of the binder (PVDF and SA) and of the potential cut-off were evaluated. The NiAl LDH electrode with SA binder shows a high capacity and more stable cycling ability than the electrode with PVDF binder. A higher amount of lithium oxide component at the surface of the NiAl LDH-SA electrode is detected by XPS. Since  $Li_2O$  is less soluble in carbonate-based solvents than LiF (detected as a major SEI component in the PVDF-based electrode), the resulting SEI should be more stable and explains the better cycling ability of the SA-based electrode. Furthermore, the NiAl LDH electrode at the discharge cut-off potential of 0.01 V can achieve a longer cycling life in comparison to the electrode at a discharge cut-off potential of 0.40 V owing to a complete conversion reaction and a complete SEI formation in the potential range of 0.01–3.0 V (*vs.*  $Li^+/Li$ ). *Ex-situ* XAS confirms that the NiAl LDH stores  $Li^+$  via a conversion mechanism ( $Ni^{2+}$  to  $Ni^0$ ) in the potential range of 0.01–3.0 V (*vs.*  $Li^+/Li$ ). Hence, this work clearly shows that the environmentally friendly sodium alginate binder, applied to NiAl LDH, improves the electrochemical performance of this material on LIBs. Future studies should focus

on addressing the irreversible capacity loss issue that is an overall problem for LDH materials; overcoming such a problem can open up a broad possibility of applying LDH materials on ion-storage batteries.

## 5 Multi-ion intercalation enables NiAl LDH a positive electrode for dual-ion battery

### 5.1 Morphology and structure of NiAl LDH

The previous work [143] shows that the as-prepared NiAl LDH material was synthesized and characterized by XRD, SEM and FT-IR, which confirms the NiAl LDH structure. Based on the previous study and the molar ratio of  $\text{Ni}(\text{NO}_3)_2 \cdot 6\text{H}_2\text{O}$  and  $\text{Al}(\text{NO}_3)_3 \cdot 9\text{H}_2\text{O}$  (a Ni:Al ratio of 2:1), the molecular formula of the as-prepared NiAl LDH is expected to be  $[\text{Ni}_{1-x}\text{Al}_x(\text{OH})_2]^{x+}(\text{NO}_3^-)_x \cdot m\text{H}_2\text{O}$  with  $m=0.16$  and  $x \approx 0.33$ .

Additionally, the magnetic properties of the NiAl LDH material were further studied based on the formula of NiAl LDH further to amplify the understanding of the valence of Ni in the material, as shown in **Figure A 7**. The ZFC/FC susceptibility vs. temperature curves show a Langevin type of paramagnetism stemming from magnetic moments at the Ni ions (**Figure A 7**). From a Curie-Weiss fit (inserted in **Figure A 7 a**) to the linear region of the inverse susceptibility vs. temperature from 200 K to 300 K an effective paramagnetic moment of  $\mu_{\text{eff}}=2.89(1) \mu_{\text{B}}$  per Ni ion and a Weiss constant of  $\theta=42.7(2)$  K pointing to dominant ferromagnetic coupling has been determined (**Figure A 7 b**). For a  $\text{Ni}^{2+}$  ion with electronic configuration  $[\text{Ar}]3d^8$ , it is expected to have two unpaired electrons in the octahedral configuration  $(t_{2g})^6(e_g)^2$  with a total spin-orbital quantum number  $S=1$  and a corresponding spin-only magnetic moment of  $2.83 \mu_{\text{B}}$ . As a result, the vast majority of Ni ions in  $\text{Ni}_{0.66}\text{Al}_{0.33}(\text{OH})_2(\text{NO}_3)_{0.33} \cdot 0.16\text{H}_2\text{O}$  are present as  $\text{Ni}^{2+}$  in octahedral coordination. The fact that the observed  $\mu_{\text{eff}}=2.89(1) \mu_{\text{B}}$  is slightly higher than the spin-only value is attributed to some contribution of orbital momentum (total orbital momentum  $J=1.21$  and Landé factor  $g=1.82645$ ). However, this can hardly be discriminated from the alternative explanation to have some minor contributions from  $\text{Ni}^{3+}$  species with a higher magnetic moment due to small off-stoichiometries. The corresponding saturation magnetization of  $M_{\text{S}} = 2.21 \mu_{\text{B}}$  is almost reached at 2 K and 7 T (**Figure A 7 c**).

## 5.2 Electrochemical performance of NiAl LDH electrode on DIB

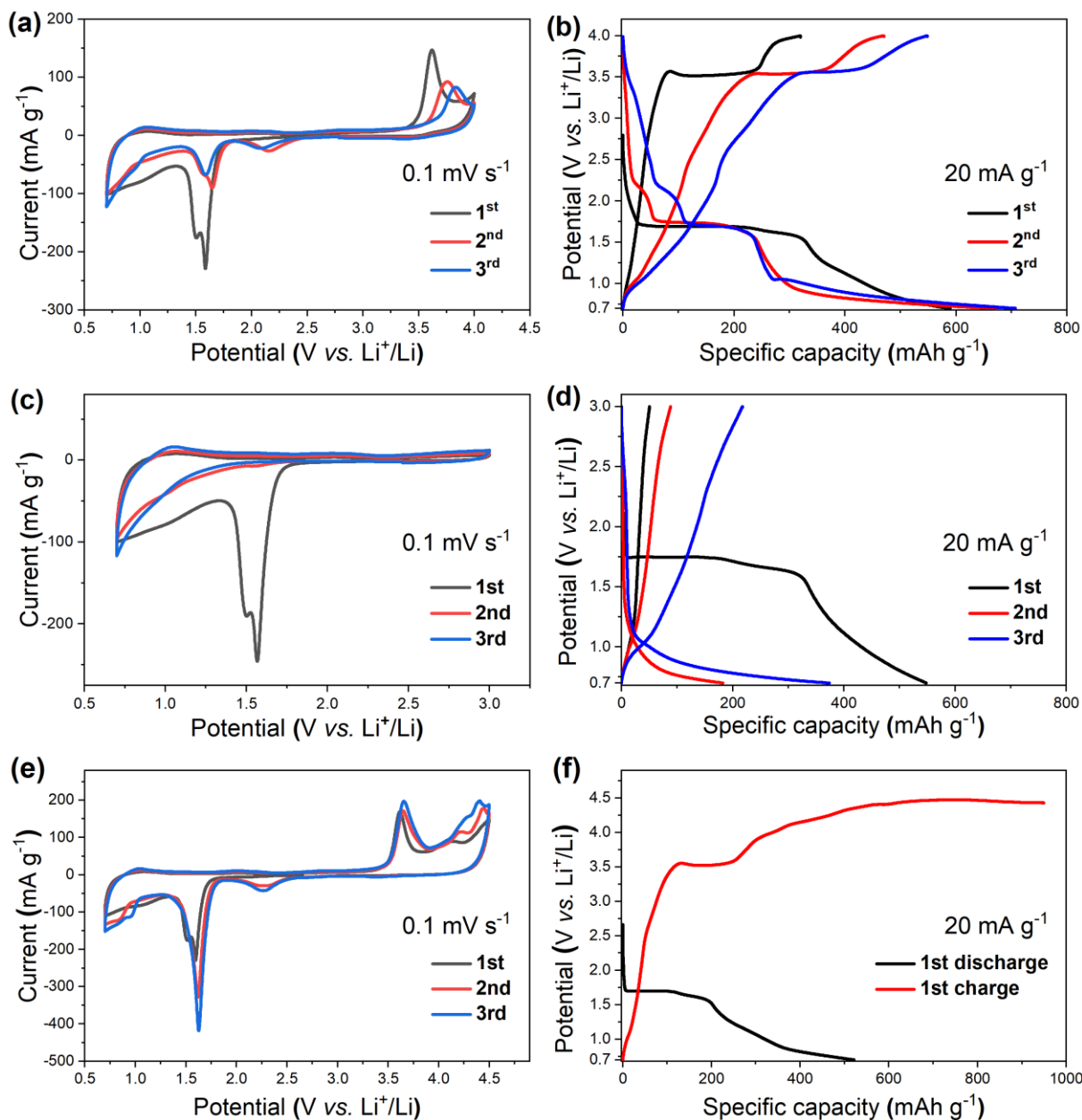


**Figure 5.1.** CV curves at  $0.1 \text{ mV s}^{-1}$  and GCD curves at the current density of  $20 \text{ mA g}^{-1}$  in  $1.0 \text{ M LiTFSI/LiNO}_3$  electrolyte of NiAl LDH electrode at different potential windows of 0.7–4.0 V (a, b), 0.7–3.0 V (c, d), and 0.7–4.5 V (e, f) (vs.  $\text{Li}^+/\text{Li}$ ).

The electrochemical performance of the NiAl LDH electrodes was studied based on a formulated binary-salt electrolyte of 1.0 M LiTFSI/LiNO<sub>3</sub> in DME solvent. The corresponding CV and GCD behaviors under different potential windows (0.7-4.0 V, 0.7-3.0 V, 0.7-4.5 V *vs.* Li<sup>+</sup>/Li, respectively) are presented in **Figure 5.1**. The initial three CV cycles were conducted at the potential range of 0.7-4.0 V (*vs.* Li<sup>+</sup>/Li) at a scan rate of 0.1 mV s<sup>-1</sup> (**Figure 5.1 a**). The first reduction scan displays one sharp peak at around 1.59 V (*vs.* Li<sup>+</sup>/Li); this is due to the initial formation of the cathodic electrolyte interphase (CEI) films on the NiAl LDH electrode [226]. A following cathodic CV slope from 1.6 V to 1.0 V can be ascribed to the reduction of LiNO<sub>3</sub> in the electrolyte to form a further protective CEI film, which hinders the further reduction of LiNO<sub>3</sub> in the following cycle, thus achieving improved reversibility. When the oxidation scan reaches high potentials beyond 3.0 V, an intense anodic peak appears at 3.6 V, which can be ascribed to the intercalation of the NO<sub>3</sub><sup>-</sup> anion [227]. This anodic peak slightly weakens in the subsequent cycles, probably owing to the electrolyte consumption. A well-overlapped profile for the second and third CV cycles indicates good reversibility of the NO<sub>3</sub><sup>-</sup> oxidation process in the LiTFSI/LiNO<sub>3</sub> electrolyte [228].

The galvanostatic charge-discharge performance of the NiAl LDH electrode in LiTFSI/LiNO<sub>3</sub> electrolyte was further investigated with galvanostatic charge-discharge cycles at the same potential range (0.7-4.0 V *vs.* Li<sup>+</sup>/Li) at 20 mA g<sup>-1</sup> as depicted in **Figure 5.1 b**. In the first cycle, a discharge plateau at around 1.69 V and a charge plateau at approximately 3.50 V are observed, consistent with the corresponding current responses of CV profiles, owing to the CEI formation and NO<sub>3</sub><sup>-</sup> oxidation, respectively. An initial discharge capacity of 589 mAh g<sup>-1</sup> is delivered, which can be ascribed to the contribution of the CEI formation and the extraction of NO<sub>3</sub><sup>-</sup>. It is worth noting that the initial charge capacity is 319 mAh g<sup>-1</sup> with an initial Coulombic efficiency of 54%; this undesired performance is possibly related to the irreversible insertion of NO<sub>3</sub><sup>-</sup> into the NiAl LDH structure during charging at the potential range of 3.0-4.0 V (*vs.* Li<sup>+</sup>/Li). The capacity gradually increases during the successive cycles (673 and 706 mAh g<sup>-1</sup> for the second and third discharge cycle, respectively), increasing ICE to 70% and 77%, respectively. This increasing capacity over the initial three cycles suggests a material activation, suggesting the synergetic participation of the NO<sub>3</sub><sup>-</sup> anions that are intrinsically embedded in the interlayers of NiAl LDH structure and the NO<sub>3</sub><sup>-</sup> anions from the electrolyte additive LiNO<sub>3</sub>, which contribute to the capacity over cycles.

To explore the impact of cut-off potentials on the multi-ion co-shuttle chemistry of NiAl LDH electrode in the LiTFSI/LiNO<sub>3</sub> electrolyte, CV and GCD were recorded at different cut-off charge potentials (3.0 V and 4.5 V vs. Li<sup>+</sup>/Li, respectively). When the upper potential is limited to 3.0 V, during the first cathodic CV scan (**Figure 5.1 c**), a similar current response corresponding to the CEI formation is observed in the potential range of 1.6–1.0 V. During the subsequent anodic scans, no CV peak related to NO<sub>3</sub><sup>-</sup> oxidation is observed, suggesting that no NO<sub>3</sub><sup>-</sup> reduction chemistry occurs at the narrow potential window of 0.7–3.0 V (vs. Li<sup>+</sup>/Li) and possibly the Li<sup>+</sup> insertion exclusively contributes the corresponding capacity at this potential window. Correspondingly, the GCD profiles at the same cut-off potential (0.7–3.0 V) (**Figure 5.1 d**) show a discharge plateau at around 1.72 V with an initial discharge capacity of 548 mAh g<sup>-1</sup> and an ICE of merely 8.9%. Besides, the subsequent capacity decays rapidly during the following cycles. Moreover, the charge capacity increases slower in the restricted potential range (0.7–3.0 V) compared to the electrode cycled between 0.7–4.0 V (vs. Li<sup>+</sup>/Li). Additionally, when the upper cut-off potential reaches 4.5 V (vs. Li<sup>+</sup>/Li), a CV profile similar to the one at the potential window of 0.7–4.0 V is observed, as shown in **Figure 5.1 e** and **f**. A strong polarization at this extended potential window charged to 4.5 V can be observed, indicating a severer electrolyte decomposition compared to the electrode performance at the potential window of 0.7–4.0 V.

Accordingly, the electrochemical stability of the LiTFSI/LiNO<sub>3</sub> electrolyte is investigated by CV using a glass cell setup with a glassy carbon as a working electrode, a lithium foil as a counter electrode and a lithium wire as a reference electrode, as shown in **Figure A 8**. For all three potential windows, an irreversible reduction peak can be observed at about 1.4 V (this is consistent with the reduction peak observed in **Figure 5.1 a** and **c**, which is described in detail in the following section), corresponding to the reduction of the LiNO<sub>3</sub> presented in the electrolyte. This peak appears during the subsequent cycles owing to the lacking of a passivation-protecting layer formation on glassy carbon. When the charge cut-off potential reaches 4.5 V, an oxidation peak at 3.6 V is observed in the CV curves, similar to what was observed in the potential window of 0.7–4.0 V (vs. Li<sup>+</sup>/Li). Besides, another strong peak appears at 4.38 V (vs. Li<sup>+</sup>/Li), accompanied by an intense polarization, which may correspond to the current increase. This is consistent with the irreversible charge plateau that appears beyond 4.4 V in the first GCD cycle. The CV results reveal that the electrochemical window's upper limit of the electrolyte can reach around 4.3 V.

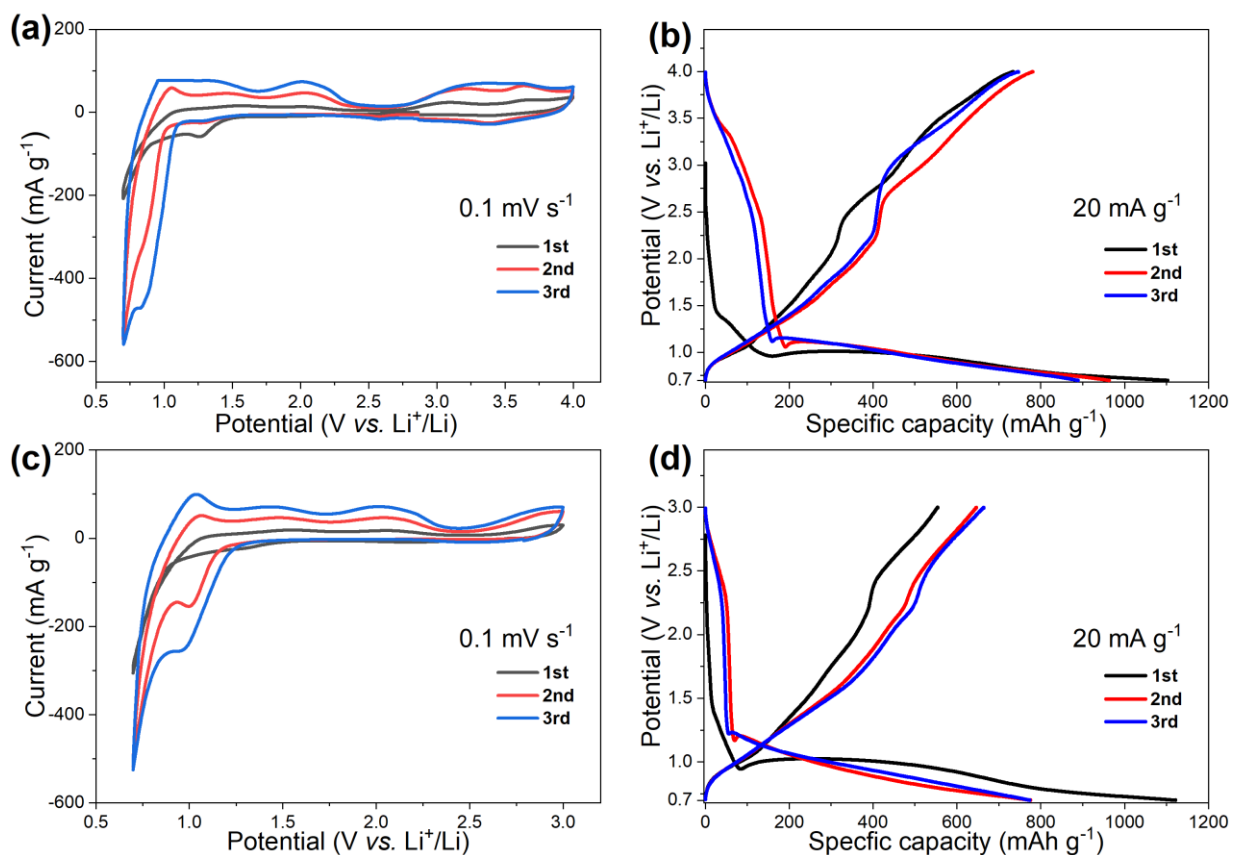


**Figure 5.2.** CV curves at  $0.1 \text{ mV s}^{-1}$  and GCD profiles at the current density of  $20 \text{ mA g}^{-1}$  of NiAl LDH electrodes in  $\text{LiNO}_3$ -free LiTFSI electrolyte at different potential windows of: (a and b)  $0.7\text{--}4.0 \text{ V (vs. Li}^+/\text{Li)}$  and, (c and d) at  $0.7\text{--}3.0 \text{ V (vs. Li}^+/\text{Li)}$ .

As a comparison, the NiAl LDH electrode was tested in a  $\text{LiNO}_3$ -free LiTFSI electrolyte to understand the impact of the electrolyte additive  $\text{LiNO}_3$  on its performance. **Figure 5.2 a** shows the CV behaviors of the NiAl LDH electrode in the  $1.0 \text{ M LiTFSI}$  electrolyte at the potential range of  $0.7\text{--}4.0 \text{ V (vs. Li}^+/\text{Li)}$  at a scan rate of  $0.1 \text{ mV s}^{-1}$ . A subtle anodic peak appears at  $3.6 \text{ V}$  during the first CV scan while fading over the following cycles, attributed to the reduction of the  $\text{NO}_3^-$  that originated from the NiAl LDH electrode during the initial reduction scan. GCD profiles (**Figure 5.2 b**) of the electrode in LiTFSI electrolyte present a high initial discharge capacity of  $1102 \text{ mAh g}^{-1}$  without a steady plateau; the capacity decreases gradually over cycles. **Figure 5.2 c** and **d** displays the CV and the GCD of the NiAl LDH electrodes in a narrow potential window of

0.7–3.0 V (vs.  $\text{Li}^+/\text{Li}$ ) in the LiTFSI electrolyte. The CV profiles (**Figure 5.2 c**) are similar to what was observed in the potential window of 0.7-4.0 V (vs.  $\text{Li}^+/\text{Li}$ ), indicating that the upper cut-off potential does not significantly affect the electrochemical features of the electrodes in LiTFSI electrolyte as the  $\text{Li}^+$  shuttle mechanism dominates. It is worth mentioning that in the  $\text{LiNO}_3$ -free LiTFSI electrolyte, the only anion that could intercalate at high potentials is TFSI $^-$ . However, the size of TFSI $^-$  anion (8.0 Å) is far larger than that of the  $\text{NO}_3^-$  anion (2.64 Å), as described in section **2.3.3**, which makes the insertion of TFSI $^-$  into NiAl LDH interlayer very difficult to occur [89][105]. This could be ascribed to the synergetic contribution of the cations ( $\text{Li}^+$ ) insertion and anion intercalation ( $\text{NO}_3^-$ ) boosted by an extended oxidation range, a similar effect cation/anion ( $\text{PF}_6^-/\text{Li}^+$ ) co-functional system also observed for recycled graphite/ $\text{LiFePO}_4$  material in DIBs reported by Meng *et al.* [229].

### 5.3 Multi-ion storage mechanism in NiAl LDH electrode

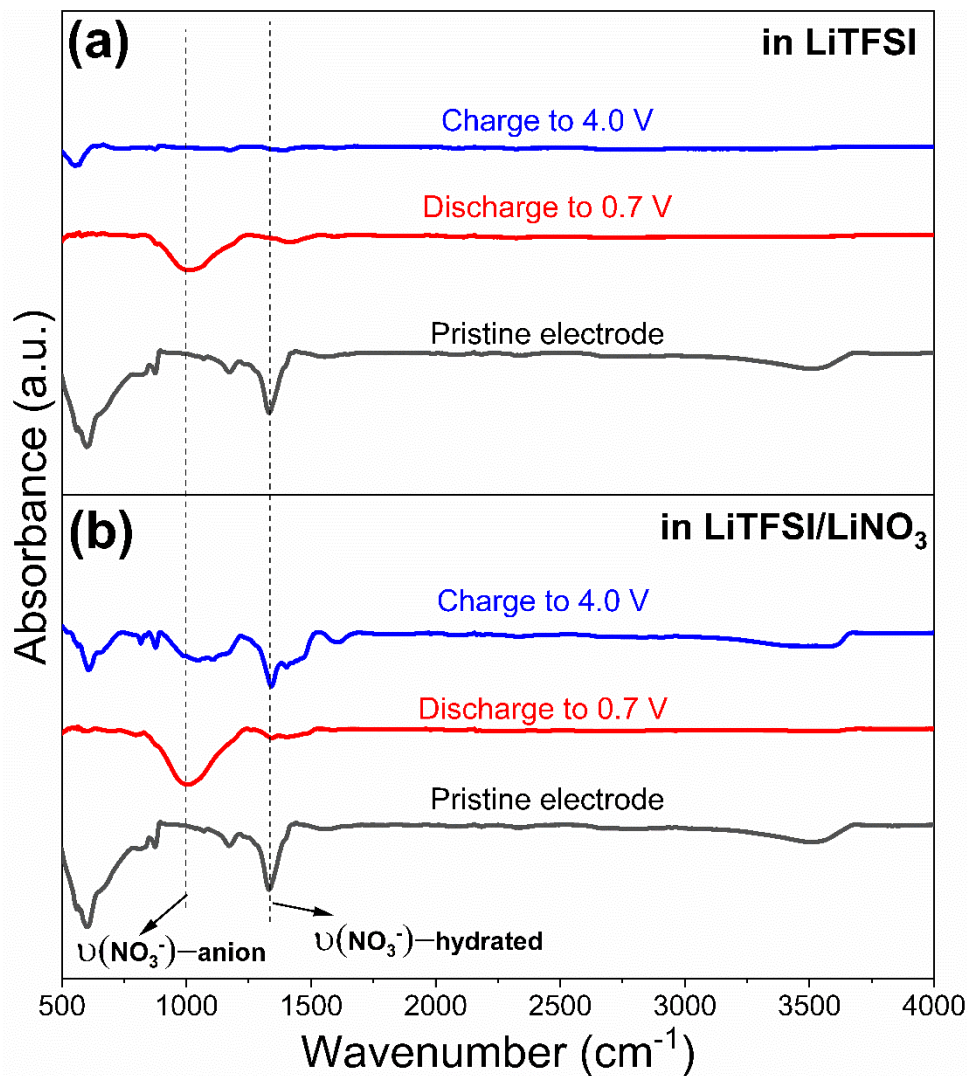


**Figure 5.3.** *Ex-situ* FT-IR spectra of NiAl LDH electrodes: a) in LiTFSI electrolyte, and b) in LiTFSI/LiNO<sub>3</sub> electrolyte during the first discharge-charge cycle.

To uncover the anion intercalation mechanism in the NiAl LDH electrode, an *ex-situ* FT-IR analysis was conducted after cycling in the 1.0 M LiTFSI/LiNO<sub>3</sub> electrolyte (**Figure 5.3 b**). From the IR spectra of the pristine NiAl LDH electrode, the vibration of the interlayer NO<sub>3</sub><sup>-</sup> anion forms the LDH structure characterized by the band location at around 1334 cm<sup>-1</sup> [230][231]. It is worth

noting that two IR bands are observed for N=O stretching modes. According to a theoretical calculation of  $\text{NO}_3^-$  in a hydrated environment by Panthak *et al.*[232], the band at  $1334\text{ cm}^{-1}$  is owing to the asymmetric stretching vibration of N=O bonds of the  $\text{NO}_3^-$ -hydrated environment, corresponding to the interlayer  $\text{NO}_3^-$  anion surrounded by the interlayer water molecule. The band at  $1000\text{ cm}^{-1}$  can be ascribed to the N=O band in  $\text{NO}_3^-$  anion, which refers to the de-intercalated  $\text{NO}_3^-$ .

When the electrode is discharged to 0.7 V, the  $\text{NO}_3^-$  stretching vibration bonding at around  $1334\text{ cm}^{-1}$ , detected in the pristine electrode, disappears [196]. Meanwhile, the appearance of the distinct band at around  $1000\text{ cm}^{-1}$  that corresponds to the  $\text{NO}_3^-$  anion reveals the extraction of  $\text{NO}_3^-$  from the NiAl LDH interlayer structure after discharging to 0.7 V. The hydrated- $\text{NO}_3^-$  bonding peak is present after charging to 4.0 V, along with the absence of the stretching vibration of  $\text{NO}_3^-$  anion at around  $1000\text{ cm}^{-1}$ , suggesting the presence of  $\text{NO}_3^-$  anion in the NiAl LDH interlayer.

When the electrode operates in the  $\text{LiNO}_3$ -free LiTFSI electrolyte (**Figure 5.3 a**), the hydrated- $\text{NO}_3^-$  bonding from the pristine is absent, and the stretching vibrations of N=O in  $\text{NO}_3^-$  anion can be found for the discharged electrode (to 0.7 V), demonstrating the de-intercalation of the  $\text{NO}_3^-$  from the NiAl LDH interlayer. However, no dramatic  $\text{NO}_3^-$  vibration band can be observed for the charged electrode (to 4.0 V), confirming the irreversible de-intercalation of  $\text{NO}_3^-$  in pure LiTFSI electrolyte, where the NiAl LDH is the only source of the anion. The limited anion shuttle in the  $\text{LiNO}_3$ -free electrolyte explains the poor cyclic performance of the NiAl LDH electrode (**Figure 5.3 b**). The FT-IR analysis shows that with the introduction of  $\text{LiNO}_3$  into the electrolyte as an additional source of  $\text{NO}_3^-$ , a sustainable and reversible  $\text{NO}_3^-$  anion shuttle into/from the NiAl LDH interlayer dynamic can be achieved.

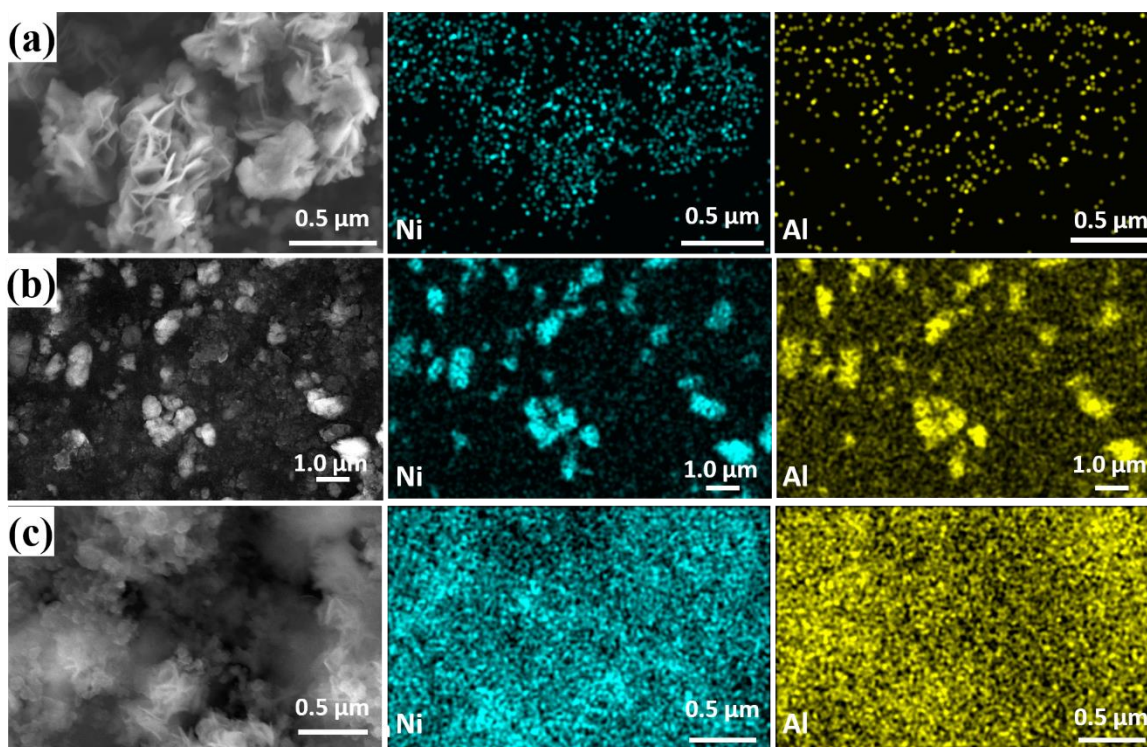


**Figure 5.4.** EDX images of NiAl LDH electrodes in LiTFSI/LiNO<sub>3</sub> electrolyte: a) pristine electrode, b) after discharging to 0.7 V, and c) after charging to 4.0 V.

The morphological features after the first discharge/charge process of the NiAl LDH electrode in the LiTFSI/LiNO<sub>3</sub> electrolyte were further investigated *via* SEM and EDX. **Figure A 9** displays the SEM morphology of NiAl LDH electrodes for the first discharge-charge process in the LiTFSI/LiNO<sub>3</sub> electrolyte. The homogeneous morphology integrated with a dispersed cluster of lamellae can be observed. The flower-like cluster structure is well-remained during the discharge-charge process, suggesting structural stability over galvanostatic cycles. Moreover, EDX mapping (depicted in **Figure 5.4**) was employed to investigate possible changes in the distribution of Ni and Al in NiAl LDH electrodes during charge and discharge. A homogeneous dispersion of Ni and Al on the pristine NiAl LDH electrode can be observed and maintained after the discharge and charge processes.

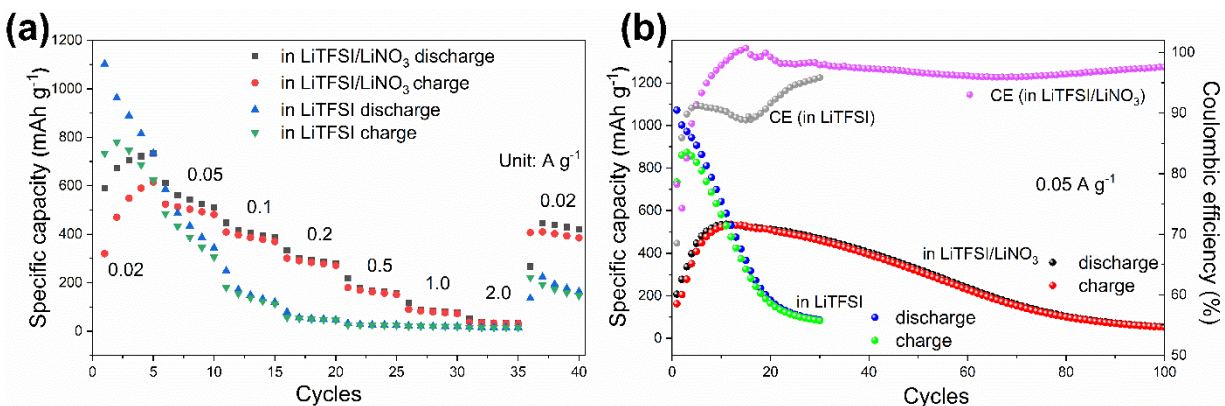


**Figure 5.5.** NiAl LDH electrode in different electrolytes at 0.7–4.0 V (vs. Li<sup>+</sup>/Li) for a) rate performance at different current densities, and b) cycling stability at a current density of 0.05 A g<sup>-1</sup>.

To further compare the electrochemical performance of NiAl LDH electrode in different electrolytes, the rate capability and cycling stability of the electrode were assessed in the potential window of 0.7–4.0 V (vs. Li<sup>+</sup>/Li) and shown in **Figure 5.5**. The NiAl LDH electrode delivers a high capacity in LiTFSI/LiNO<sub>3</sub> electrolyte with a retention of 71.0% of the first discharge capacity after recovery to 0.02 A g<sup>-1</sup> at the end of the rate test. For the electrode operating in LiTFSI electrolyte, the corresponding rate capacities show a fast decay from a higher initial capacity and end up with a retention of only 13.0% (with respect to the initial discharge capacity) after 40 cycles. Besides, the cycling stability of the NiAl LDH electrodes in the two electrolytes is tested at 0.05 A g<sup>-1</sup> for 100 cycles and depicted in **Figure 5.5 b**. During the initial 12 cycles, the NiAl LDH positive electrode in LiTFSI/LiNO<sub>3</sub> electrolyte presents a distinct capacity increase (159% of the increase to 536 mAh g<sup>-1</sup> with respect to the first discharge capacity), probably due to the progressive electrode wetting and the increased exposure of the active sites during the gradual activation process over cycling. With further increases in cycles, the discharge capacity decays to 53 mAh g<sup>-1</sup> with a retention of 26.0% (of the initial discharge capacity) after 100 cycles, where the continuous consumption of LiTFSI/LiNO<sub>3</sub> electrolyte can be one of the causes. The corresponding ICE reaches around 97.6% after 100 cycles. As a comparison, the reversible capacity retention of the NiAl LDH electrode in the LiNO<sub>3</sub>-free LiTFSI electrolyte is only 9.0% after 30 cycles.

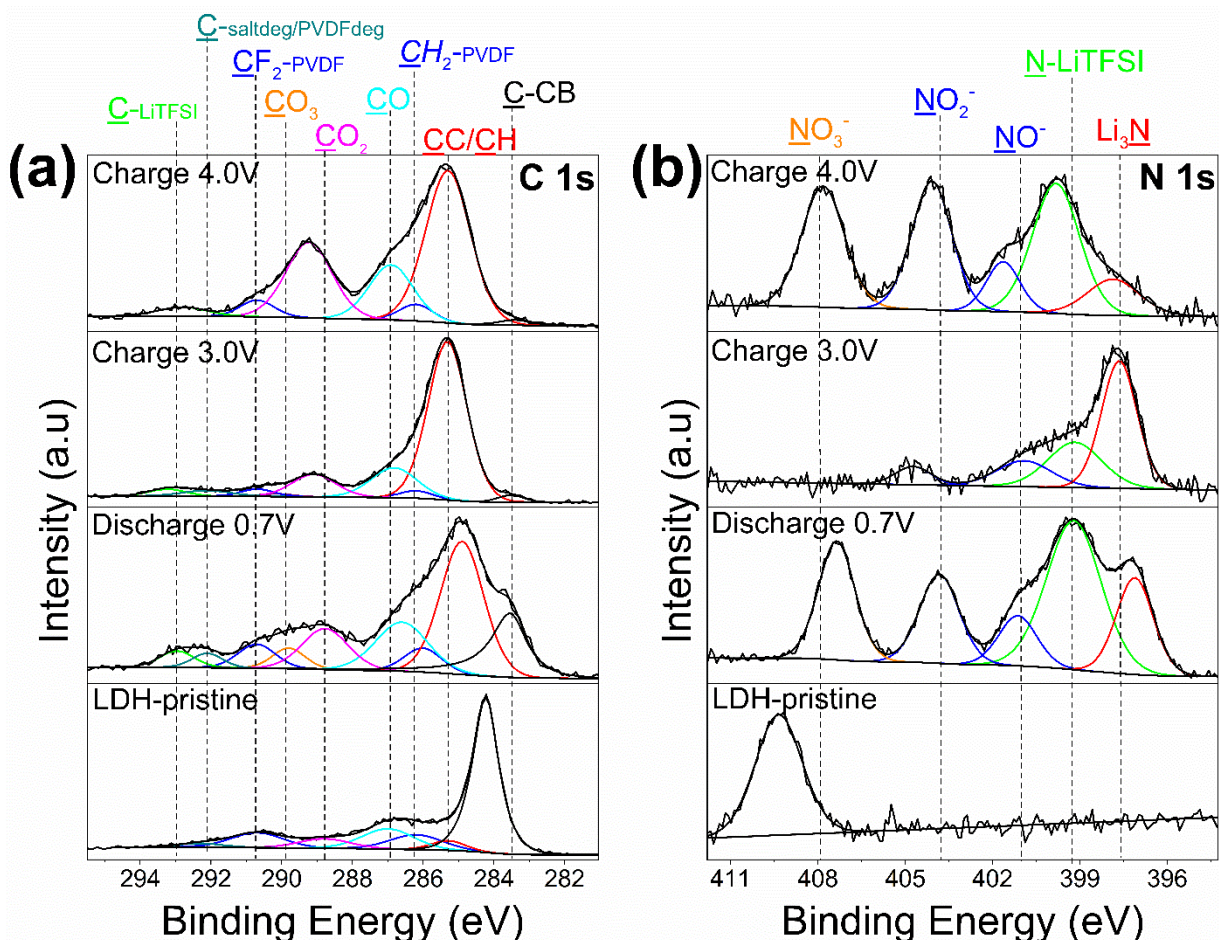


**Figure 5.6.** *Ex-situ* (a) C 1s and (b) N 1s XPS spectra conducted in LiTFSI/LiNO<sub>3</sub> electrolyte of NiAl LDH electrodes of pristine, discharged to 0.7 V, charged to 3.0 V, and charged to 4.0 V (vs. Li<sup>+</sup>/Li) on the first cycle, respectively.

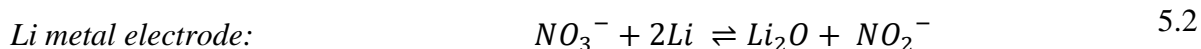
*Ex-situ* XPS analysis of the NiAl LDH electrodes at different discharge/charge potentials during the first cycle (discharged to 0.7 V, charged to 3.0 V, and fully charged to 4.0 V, respectively) was carried out to understand the storage mechanism with the presence of NO<sub>3</sub><sup>-</sup> in the NiAl LDH structure in the LiTFSI/LiNO<sub>3</sub> electrolyte and to gain more information on the chemical composition of the CEI films on the electrodes over the first cycle.

The C 1s spectra of the NiAl LDH electrodes at different discharge-charge potentials are shown in **Figure 5.6 a**. The peak at 283.5 eV is attributed to the carbon black (CB) [233], which is present

in the formulation of the NiAl LDH electrode. The three components at 286.2 eV (from the CH<sub>2</sub> chemical environment in PVDF binder), 290.7 eV (CF<sub>2</sub>-CH<sub>2</sub>), and 291.8 eV (CF<sub>x</sub>), evidence the presence of the PVDF binder on the pristine electrode, and salt degradation species during cycling [210][234]. On the spectra of the electrode discharged to 0.7 V (*vs.* Li<sup>+</sup>/Li), some new peaks of C1s spectra appear. The peaks centered at 285.4 eV (C-C/C-H), 286.8 eV (mix of C-O/ROLi) [211], 288.5 eV (C=O), 290.0 eV (attributed to the Li<sub>2</sub>CO<sub>3</sub> chemical environment), and 293 eV (CF<sub>3</sub> from the LiTFSI), are related to the degradation products that composed of the CEI films after the first discharge process [235][236][237][238]. Besides, based on the XPS depth of 5-10 nm, the high intensity of the components attributed to the carbon black and PVDF (CH<sub>2</sub> and CF<sub>2</sub>) suggests a thin CEI film formation for the electrode discharged to 0.7 V.

For the electrodes charged to 3.0 V and 4.0 V (*vs.* Li<sup>+</sup>/Li), a decreasing tendency of the specific area of the characteristic peaks of C-O-C, C=O and O-C=O groups in the C1s spectra on the electrode is observed, as depicted in **Figure 5.6 a** and **Figure A 10**, indicating a partial degradation of CEI components. This phenomenon shows that the formation of CEI film is a dynamic evolution during the discharge-charge process, as also observed directly by *in-situ* atomic force microscopy for a Li anode in the LiNO<sub>3</sub>-containing electrolyte by Lang *et al.* [239]. Besides, the decreased intensity of the peaks corresponding to carbon black and PVDF (CH<sub>2</sub> and CF<sub>2</sub>) suggests a thicker CEI film formation for the electrode charged to 3.0 V.

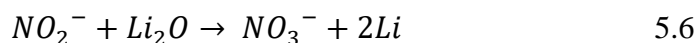
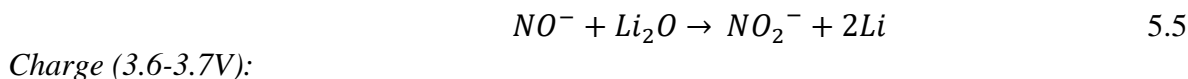
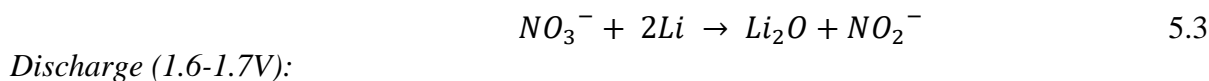
The N1s spectra collect signals of all the nitrogen species present on the surface of the *ex-situ* electrode, as shown in **Figure 5.6 b**. The peak centered at around 399.7 eV can be attributed to the nitrogen from LiTFSI [240][241]. The peak detected at 397.5 eV corresponds to Li<sub>3</sub>N, which is generated by the degradation of the LiTFSI electrolyte on the Li electrode. This compound is soluble in the electrolyte and thus can migrate to the NiAl LDH electrode [237]; Li<sub>3</sub>N possesses a high ion conductivity (1.2·10<sup>-3</sup> S cm<sup>-1</sup> at 25°C), thus boosting the Li-ions' transport [242]. Three other components detected at 401.0 eV, 403.7 eV, and 408.0 eV can be attributed to the NO<sup>-</sup> anion, the NO<sub>2</sub><sup>-</sup> anion, and NO<sub>3</sub><sup>-</sup> environments, respectively. The peaks at 401.0 eV and 403.7 eV are the signals related to nitrate generated from the reduction of LiNO<sub>3</sub> from the LiTFSI/LiNO<sub>3</sub> electrolyte on the Li electrode during cycling [243]:



These species' high solubility endues them to easily migrate from the electrolyte to the NiAl LDH positive electrode during cycling in the DME-based solvent, explaining their presence on the NiAl LDH electrode. The presence of  $\text{NO}_3^-$ , which corresponds to the observed peak at 408.0 eV, on the NiAl LDH electrode discharged at 0.7 V can be ascribed to the extraction of  $\text{NO}_3^-$  anions from the bulk of NiAl LDH structure to the interface, which is consistent with the absence of the nitrate signal in the bulk of electrode from the FT-IR measurement after discharging to 0.7 V (**Figure 5.3**).

During the charging process up to 3.0 V, the detected signals related to reduced  $\text{NO}_2^-/\text{NO}^-$  species are due to their migration from the Li electrode through the electrolyte or the preceding reduction process of  $\text{NO}_3^-$  ions at 1.7 V that comes from the NiAl LDH interlayer structure [244]. For the electrode that is charged to 3.0 V, a relatively low amount of  $\text{NO}_2^-/\text{NO}^-$  can be detected (**Figure A 10**). However, the limited anion intercalation at this charging potential, which is due to lacking  $\text{NO}_3^-$  anion, results in the absence of  $\text{NO}_3^-$  signal from the N1s spectrum. This result is well consistent with the CV profile of the NiAl LDH electrode in LiTFSI/LiNO<sub>3</sub> electrolyte.

For the *ex-situ* NiAl LDH electrode charged to 4.0 V, the presence of  $\text{NO}_3^-$  and  $\text{NO}_2^-$  peaks on the electrode CEI can be attributed to the oxidation of previously intercalated  $\text{NO}_2^-$  and  $\text{NO}^-$  species during the charging to >3.6 V process. Based on the XPS study on the *ex-situ* electrodes, the migration of nitrate in the DIB can be depicted by the following equations:



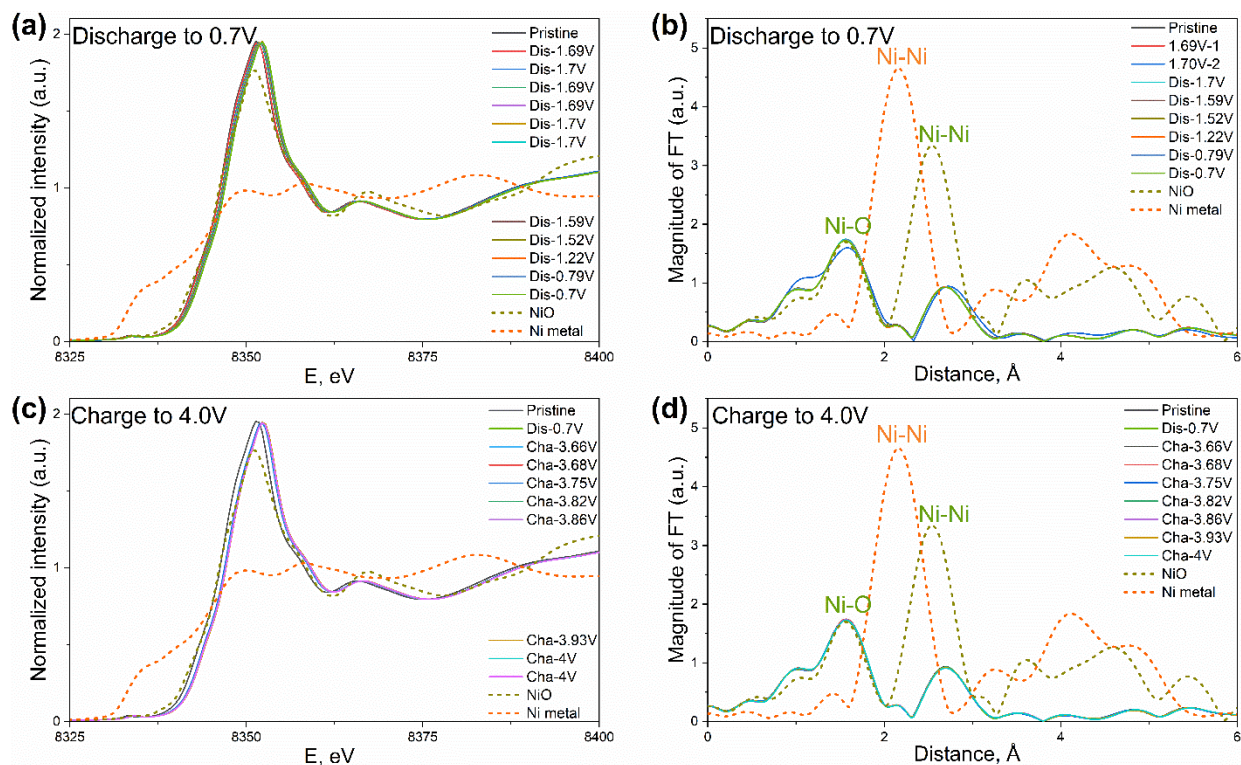
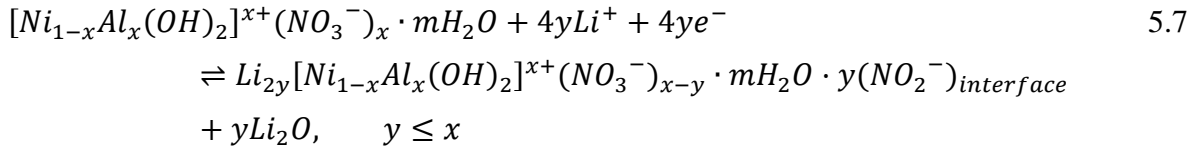


**Figure 5.7.** *In-situ* normalized XANES spectra at Ni K-edge and Fourier transform of the recorded EXAFS spectra of the discharge process (a) and (b) and, the charging process (c) and (d).

To further elucidate the redox chemistry of the NiAl LDH electrode in the LiTFSI/LiNO<sub>3</sub> electrolyte, *in-situ* XAS analysis was performed during the first galvanostatic cycle at 20 mA g<sup>-1</sup>. The progress of the Ni K-edge XANES and FT-EXAFS spectra during the electrochemical process are shown in **Figure 5.7**. During the first discharge steps to the potential of 0.7 V, the Ni K-edge of the NiAl LDH shows a slight shift to low energy, as shown in **Figure 5.7 a**, implying a considerable tendency of Ni oxidation. It could be explained by the fact that an increased lamellar charge density increases the electrostatic attraction of the layer anions, resulting in anions accumulation on the interface of NiAl LDH electrode during the discharging process. A study focusing on the anion (Cl<sup>-</sup>) exchange of CoAl-LDH material observed a similar trend [245], where the adsorption capacity of Co<sub>4</sub>Al<sub>1</sub>-Cl-LDH (827.5 mg g<sup>-1</sup>) was far greater than that of Co<sub>2</sub>Al<sub>1</sub>-Cl-LDH (581.9 mg g<sup>-1</sup>). This was elucidated as a decreased percentage of Al<sup>3+</sup> resulting in a

reduced surface area (per unit charge), thus enhancing the electron mobility between the layers to achieve an easier anion absorption or exchange. Compared to the conversion reaction of NiAl LDH electrode on LIB, as shown in **Figure A 11**, when the Ni ions are reduced during discharge, the decreasing amplitude of the FT-EXAFS peaks emphasizes structure disordering during the electrochemical reaction.

The positive charge of intercalated Li-ion can be equilibrated by the reduction products of  $\text{NO}_3^-$  anions, which is supported by *ex-situ* N1s X-ray photoelectron spectra in **Figure 5.6 b**, that intensive signals of  $\text{NO}_3^-$  and  $\text{NO}_3^-$  reduction products are detected for the electrode charged to 0.7 V. During the subsequent charging process, no energy shift for the Ni K-edge is observed from the normalized XANES (**Figure 5.7 c**), which can be ascribed to the formation of  $\text{Li}_2\text{O}$  layer on the interface of NiAl LDH electrode hinders the following redox chemistry in the LDH lamellas. This corresponds to the decreased signal of carbon black for the *ex-situ* electrode charged to 4.0 V in **Figure 5.6 a**, suggesting that a thicker interface is obtained after charging to 4.0 V. In addition, from the FT-EXAFS graph for NiAl LDH electrode, no changing amplitude and peak position is observed, which proves the high stability of the local structure of NiAl LDH upon cycling. A proposed mechanism of NiAl LDH electrode during the discharge/charge process can be expressed by the following equation:



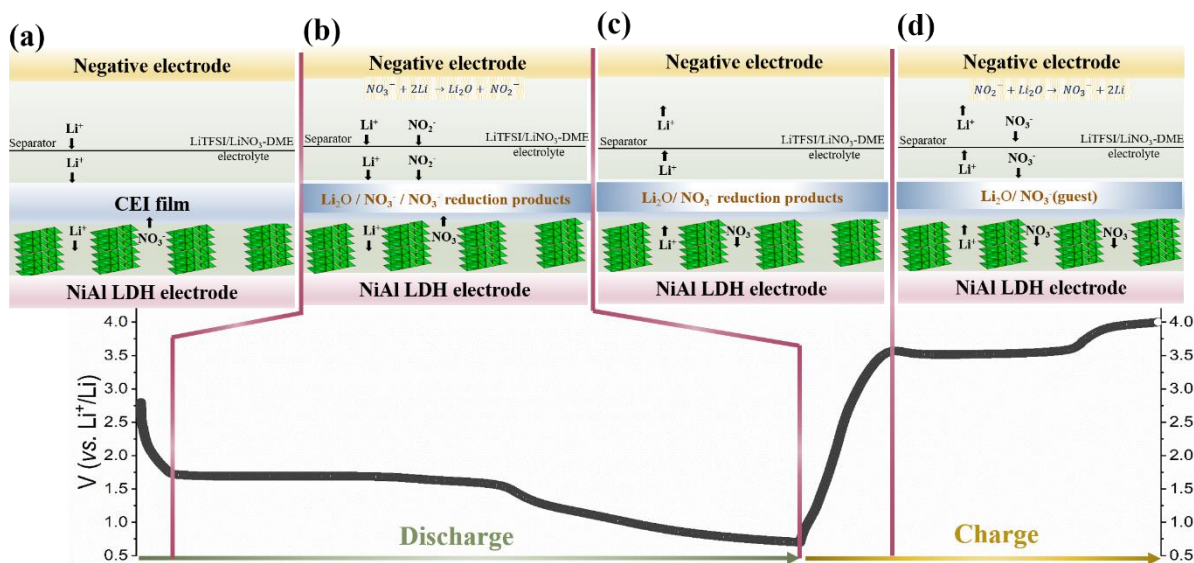


**Figure 5.8** The schema illustrates the working mechanism of the NiAl LDH electrode with  $\text{Li}^+/\text{NO}_3^-$  shuttle in the  $\text{LiTFSI}/\text{LiNO}_3$  electrolyte during the first cycle: a) first discharging process (OCV-discharge plateau), b) first discharging process (discharge plateau-0.7 V), c) first charging process (0.7-charging plateau and, d) first charging process (charge plateau-4.0 V).

Based on the *ex-situ* and *in-situ* characterization, a conceptual schema was developed to illustrate the working mechanism of multi-ion storage in the NiAl LDH electrode operating in 1.0 M  $\text{LiTFSI}/\text{LiNO}_3$  electrolyte at a potential window of 0.7-4.0 V during the first cycle, as depicted in **Figure 5.8**. During the initial discharge process from OCV to 0.7 V (vs.  $\text{Li}^+/\text{Li}$ ), as shown in **Figure 5.8 a**, Li ions are inserted into the NiAl LDH electrode from the electrolyte along with the reverse migration of  $\text{NO}_3^-$  from the interlayer of NiAl LDH to the interface. At the potential of around 1.6 V (**Figure 5.8 b**), the  $\text{NO}_3^-$  reduction takes place, thus forming the CEI film with reduced species ( $\text{NO}_2^-$  and  $\text{NO}^-$ ), which is consistent with the cathodic peak at 1.6-1.7 V in the CV profiles (**Figure 5.1 a**). During the subsequent charging process at the potential range of 0.7-3.6 V (vs.  $\text{Li}^+/\text{Li}$ ), as depicted in **Figure 5.8 c**, Li ions are extracted from the NiAl LDH structure and deposited on the negative electrode. The  $\text{NO}_3^-$  anions originally extracted from the NiAl LDH structure are inserted back at the charging potential of 3.6-3.7 V. Guest  $\text{NO}_3^-$  anions are formed on the negative electrode and inserted into the NiAl LDH structure, resulting in an

increased capacity. At the same time, the reduced species, such as  $\text{NO}_2^-$  and  $\text{NO}^-$ , migrate from the negative electrode side to the interface of the NiAl LDH electrode. Thus, during the electrochemical process, the species from electrolyte and CEI are actively involved instead of Ni from the structure of NiAl LDH, which is verified by *in-situ* XAS (Figure 5.7).

## 5.4 Conclusive aspects: multi-ion storage of NiAl LDH electrode

In summary, this work reports a positive electrode concept suitable for DIBs based on co-shuttle dynamics of dual-ion, *i.e.*, cation ( $\text{Li}^+$ ) and anion ( $\text{NO}_3^-$ ) in the NiAl LDH structure. The NiAl LDH electrode operates in a formulated bi-salt electrolyte consisting of 1.0 M LiTFSI and 0.7 M  $\text{LiNO}_3$  in DME solvent at a safe oxidation potential of 4.0 V (*vs.*  $\text{Li}^+/\text{Li}$ ). Unlike traditional graphite positive electrode for DIBs, the NiAl LDH electrode is based on the co-shuttle mechanism of  $\text{Li}^+/\text{NO}_3^-$ , which achieves a maximum discharge capacity of 589 mAh  $\text{g}^{-1}$  at 20 mA  $\text{g}^{-1}$ . The NiAl LDH electrode shows a tendency to increase the capacity (159% with respect to the initial discharge capacity) for the first 12 cycles at the current density of 50 mA  $\text{g}^{-1}$  owing to an additional source of  $\text{LiNO}_3$  supporting the intercalation/de-intercalation of anions. The multi-ion storage mechanism of NiAl LDH electrode during the first cycle was investigated at different charge cut-off potentials of 3.0 V and 4.0 V (*vs.*  $\text{Li}^+/\text{Li}$ ), respectively, by *ex-situ* FT-IR, XPS, and *in-situ* XAS characterization. During the first discharge process (from OCV to 0.7 V), the insertion of  $\text{Li}^+$  and the de-intercalation of  $\text{NO}_3^-$  occur. During charging from 0.7 to 4.0 V (*vs.*  $\text{Li}^+/\text{Li}$ ), Li ions are extracted from the NiAl LDH electrode; meanwhile, the  $\text{NO}_3^-$  anion intercalates into the NiAl LDH interlayer. During the first cycle, the Li ions shuttle is achieved with the involvement of the redox chemistry of  $\text{NO}_3^-$ . Adding  $\text{LiNO}_3$  in the electrolyte enables a reversible intercalation/de-intercalation of  $\text{NO}_3^-$  and a high recovered capacity.

Although the electrochemical performance of this NiAl LDH electrode may be further enhanced *via* optimization strategies, it broadens the possibility of using non-carbon cathodes in DIBs with high capacity at a safe but high potential window. A full DIB concept integrated with NiAl LDH electrode and a non-metallic anode is worth to be taken consideration. The feasibility of this anion/cation multi-ion storage chemistry provides an effective approach to designing post-graphite-based DIBs for possible practical applications in the future.

## 6 Elucidation of the anion shuttle mechanism for NiAl LDH as Cl-storage electrode

To date, a few Cl<sup>-</sup>-containing LDHs materials have been applied as positive electrodes on CIBs, and their corresponding electrochemical performance was investigated, whereas the capacity fading of LDH electrodes is not clearly unveiled. As in my previous work, NO<sub>3</sub><sup>-</sup> has been illustrated to actively participate in the multi-ion shuttle when the NiAl LDH (with NO<sub>3</sub><sup>-</sup> as the interlayer anion) used as an electrode on DIBs, a Cl<sup>-</sup>-free NiAl LDH electrode was applied as the positive electrode on CIBs to investigate the anions storage mechanism and uncover the causing for capacity decay.

### 6.1 Cell configuration on CIB

#### 6.1.1 Reference electrodes

As one widely used reference electrode on LIBs, Li metal can also be used as RE in CIBs. However, the suitability of Li metal in specific Cl-containing electrolytes in CIBs is not well investigated so far, making it crucial to screen out reference electrodes (RE) suitable for CIB systems. Herein, an alternative cell configuration has been proposed, where the potential stability of two quasi-reference electrodes (QRE, silver (Ag) and Li) in a Cl-based electrolyte is investigated. A three-electrode glass cell was applied for the screening of REs.

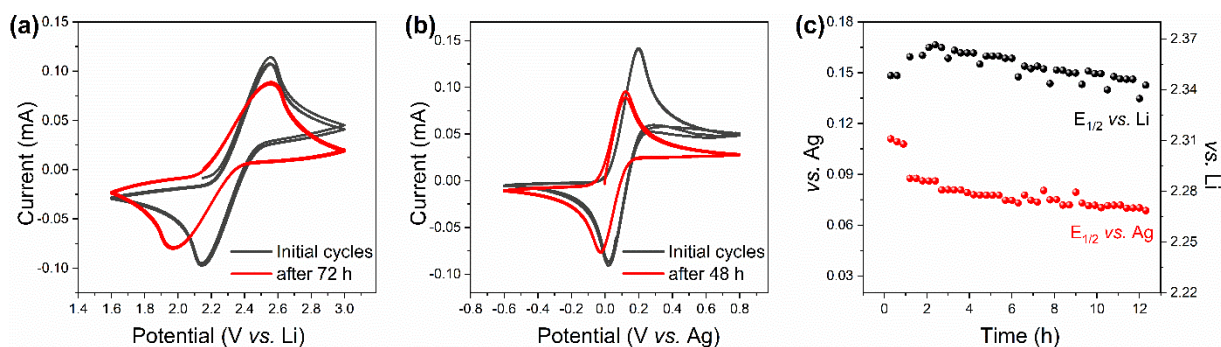


**Figure 6.1.** CV curves in 0.5 M Bpy<sub>14</sub>Cl/PC with 0.02 M Cc<sup>+</sup> at 10 mV s<sup>-1</sup>: a). vs. Li QRE, b) vs. Ag QRE, and c) evolutions of  $\phi_{\text{Cc/Cc}^+}$  vs. two QREs measured vs. time.

The cyclic voltammetry curves shown in **Figure 6.1** were obtained from a three-electrode glass cell with an electrolyte based on 0.02 M cobaltocene (Cc) (as internal reference electrode) and 0.5 M Bpy<sub>14</sub>Cl/PC, a platinum (Pt) disc working electrode, a larger area Pt counter electrodes. Two QREs electrodes (Ag and Li) were evaluated for comparison. The potential of the Cc/Cc<sup>+</sup> vs. the QREs was calculated using the equation:

$$\varphi_{Cc/Cc^+} = \frac{\varphi_{p,c} + \varphi_{p,a}}{2} \quad 6.1$$

Where  $\varphi_{Cc/Cc^+}$  is the measured potential of the cobaltocene/cobaltocenium couple,  $\varphi_{p,c}$  and  $\varphi_{p,a}$  is the cathodic and anodic peak potentials, respectively.

Cyclic voltammograms showing the oxidation and reduction of cobaltocene in Bpy<sub>14</sub>Cl/PC electrolyte against Li and Ag QREs are presented in **Figure 6.1 a** and **b**, respectively. The CVs clearly show different half-wave potentials in the electrolyte for the Ag QRE (0.11 V) and the Li QRE (2.35 V). An excellent overlapping of the CV profiles is observed when Ag is used as QRE, indicating better stability of the Ag QRE in the Bpy<sub>14</sub>Cl/PC electrolyte. It is worth noting that the potential of the QRE vs. SHE could be different once the electrolyte composition change. A change in the electrolyte composition varies the ionic speciation in solution, influencing the charging phenomena at the QRE/electrolyte interface.

**Figure 6.1 c** shows the measured potential of the Cc/Cc<sup>+</sup> redox couple vs. Li and Ag QRE over time. The measurements demonstrate a significant influence of the solvent composition on the potential value and stability of the QRE. The most relevant effect of the solvents is the QRE potential drift. After the first one-hour resting period, the Ag QRE shows the most significant potential shift of about 0.02 V. Afterwards, the Ag QRE remains relatively stable against  $E_{1/2}$  of Cc/Cc<sup>+</sup>. While using Li as the QRE, a higher potential scattering during the four consecutively CV cycles is observed. Suggesting Ag can be chosen as a more stable QRE in this CIB system.

### 6.1.2 Electrochemical stability of the Cl-based electrolyte

The electrochemical stability window (ESW) is one of the crucial criteria to characterize the stability of the electrolyte. Generally, the larger the electrochemical window obtained, the better the electrolyte's stability is. Herein, Ag was applied as the reference electrode for the investigation

of ESW of the electrolyte, as Ag shows the best compatibility and stability in the Bpy<sub>14</sub>Cl/PC electrolyte based on the above investigation in section 6.1.1.

Standard glass cells were built to evaluate the electrochemical stability of the Bpy<sub>14</sub>Cl/PC electrolyte. Two Pt foils with low and high areas are applied as the working electrode and counter electrode, respectively. To screen out a suitable configuration for further application, two different systems were investigated: stainless steel (SS)||Pt and SS||Li as WE and CE, respectively. The electrochemical stability of the electrolyte in different configurations was determined by linear sweep voltammetry (LSV) at a scanning rate of 10 mV s<sup>-1</sup> from -3.0 to 2.0 V (*vs.* Ag) at 25°C, as presented in **Figure A 12**.

The standard cell (Pt||Pt) presents a wide potential window of -2.17-1.48 V *vs.* Ag, while the stainless steel foil worked as the working electrode shows a stability window of -2.17-0.92 V *vs.* Ag. Interestingly, in this investigation, when applying Li as the counter electrode and stainless steel foil as the working electrode, the potential window remains stable in the same range of around 3.09 V. The maximum potential range that can be achieved in a battery is 0.4-3.8 V (*vs.* Li). Past studies on LDH positive electrodes for CIBs used a restricted potential range of 1.2-3.0 V (*vs.* Li<sup>+</sup>/Li) [161][160], this reported potential window can be expanded based on the pre-tested electrolyte stability window of the electrolyte. Therefore, a slightly broader potential range than 1.2-3.0 V (*vs.* Li) is used for the electrochemical measurements of this work, *i.e.*, 1.0-3.0 V (*vs.* Li).

## 6.2 Electrochemical performance of NiAl LDH electrode on CIB

The cyclic voltammetry of the NiAl LDH electrode was tested in 0.5 M Bpy<sub>14</sub>Cl/PC electrolyte at a scan rate of 0.02 mV s<sup>-1</sup> in the potential range of 1.0-3.0 V (*vs.* Li), as shown in **Figure 6.2 a**.

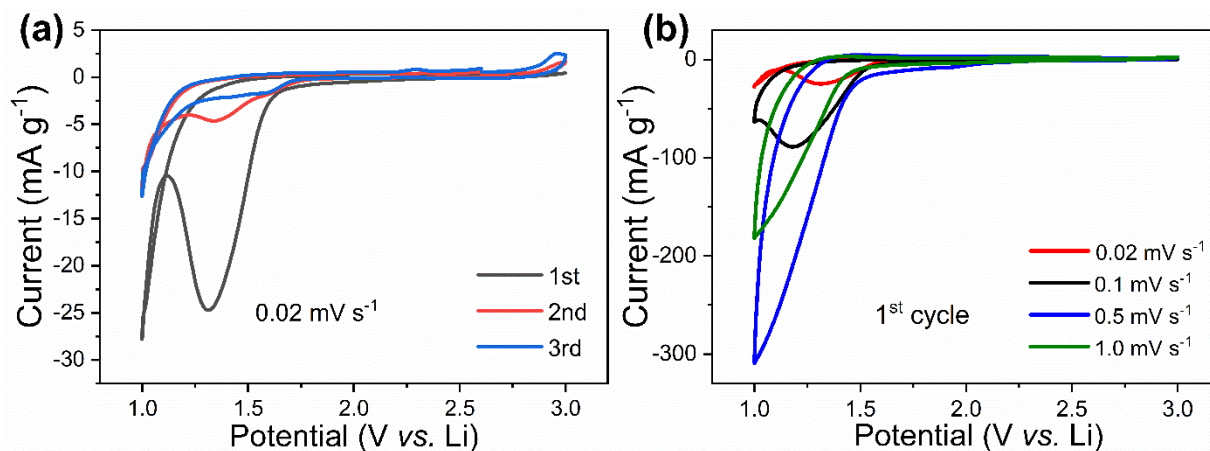


**Figure 6.2** CV curves of NiAl LDH electrode in 0.5 M Bpy<sub>14</sub>Cl/PC electrolyte: a) at 0.02 mV s<sup>-1</sup> and, (b) at different scan rates of 0.02, 0.1, 0.5 and 1.0 mV s<sup>-1</sup> for the first cycle within 1.0-3.0 V (vs. Li).

During the first CV scan, an intensive cathodic peak at 1.31 V can be observed, which decays during the subsequent cycle, this peak could be owing to the formation of CEI films on the NiAl LDH electrolyte. After the first CV scan, the cathodic peak at around 1.5 V can be ascribed to the negative shift of the reduction peak at 1.31 V during the first cycle, corresponding to a decreased polarization along cycling.

For the oxidation curves, no distinctive anodic peaks were found, which could be ascribed to the irreversible reduction of NO<sub>3</sub><sup>-</sup> and the formation of thick CEI during the previous discharge process. To further reveal the behavior of the NiAl LDH electrode at different scan rates, multiple scan rates of 0.02, 0.1, 0.5, and 1.0 mV s<sup>-1</sup> were performed on the electrode, respectively. **Figure 6.2 b** depicts the first cycle at different scan rates. The cathodic peak at 1.31 V shifts to lower potential with the increase of scan rates due to the cells' intrinsic resistance [246].

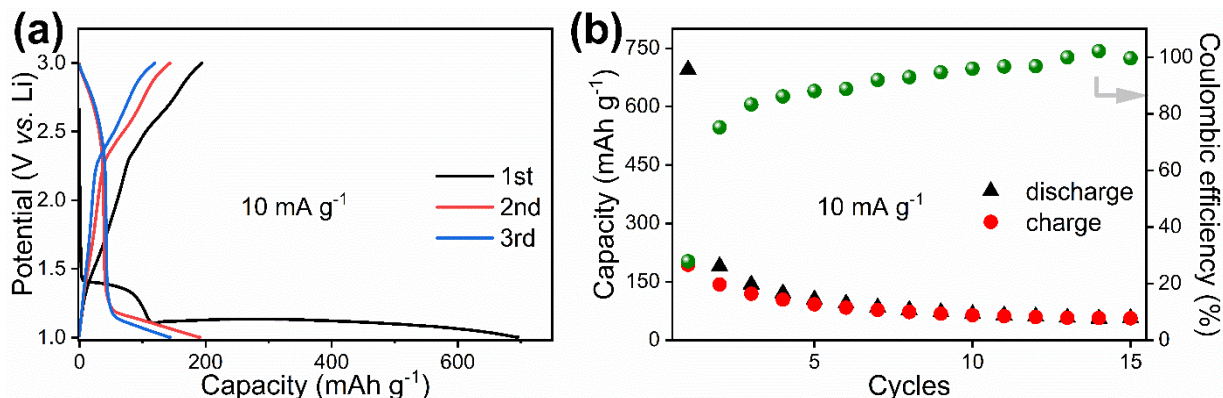


**Figure 6.3** a) Galvanostatic charge-discharge curves; and b) cycling performance of NiAl LDH electrode in Bpy<sub>14</sub>Cl/PC electrolyte within 1.0–3.0 V (*vs.* Li) at 10 mA g<sup>-1</sup>.

The initial three galvanostatic charge-discharge cycles of the NiAl LDH electrode in 0.5 M Bpy<sub>14</sub>Cl/PC electrolyte at 10 mA g<sup>-1</sup> at the voltage range of 1.0–3.0 V (*vs.* Li) is depicted in **Figure 6.3**. During the first discharge cycle, two plateaus can be observed at around 1.4 V and 1.12 V, respectively. An initial discharge capacity of 695 mAh g<sup>-1</sup> is delivered with an initial Coulombic efficiency of 28.0%, which reaches 83.0% in the third cycle. With the irreversible first discharge capacity delivered, the NiAl LDH electrode suffers from rapid capacity decay in the following 15 cycles with a remaining capacity of 56.8 mAh g<sup>-1</sup> after 15 cycles. Such irreversible behavior during the first cycle could be ascribed to the irreversible reduction of NO<sub>3</sub><sup>-</sup>, which is extracted from the NiAl LDH structure at around 1.4 V (**Figure 6.2 a**), as a similar mechanism is disclosed in chapter **5.3**, and the formation of the thick CEI layer. Interestingly during the initial discharge GCD cycle, two discharge plateaus can be observed at around 1.4 V and 1.1 V (*vs.* Li), respectively, suggesting the importance of understanding the capacity decay causes and the anion storage mechanism during the first cycle.

### 6.3 Cl-ion storage mechanism in NiAl LDH electrode

Current reports of LDH positive electrodes on CIBs focus on the Cl-ion in the interlayer. However, the mechanism of Cl-ion storage of Cl-free LDH has not been fully uncovered yet. Based on the previous electrochemical study on Cl<sup>-</sup>-free NiAl LDH on CIBs, the Cl-ion storage mechanism and the role played by the interlayer anion (NO<sub>3</sub><sup>-</sup>) in Cl-ion batteries are illustrated in

the following. Based on the current reports about the Cl-ion storage mechanism in a CIB (anions shuttle to the negative electrode and cations to the positive electrode during discharging), CIBs follow the mechanism based on equations 2.5-2.6 during discharge [5][247]. Given this background, a hypothesis is formulated for the storage mechanism of the Cl-free NiAl LDH on CIBs: on the first discharge cycle,  $\text{NO}_3^-$  ions are extracted from the LDH positive electrode structure. Cl ions are inserted back into the NiAl LDH structure during the subsequent charging process. Thus, the corresponding mechanism measurements were further implemented.

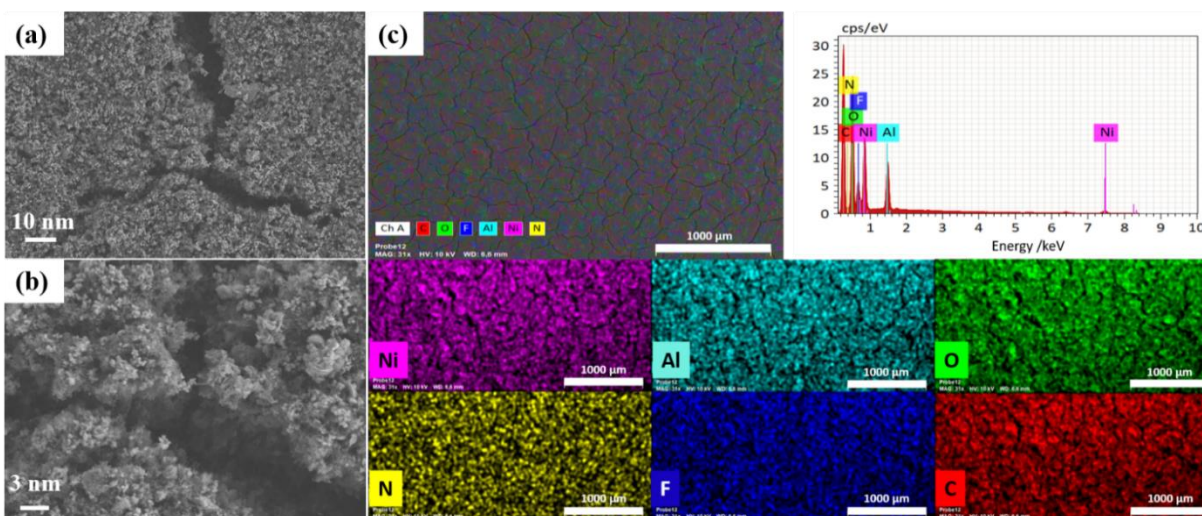


**Figure 6.4.** SEM (a,b) and EDX mapping (c) of the pristine NiAl LDH electrode.

To gain information about the morphology of the NiAl LDH electrode at discharge/charge status, SEM and EDX measurements were employed, as shown in **Figure 6.4**. A flower-like integrated laminar-type structure is well retained from **Figure 6.4**, consistent with the NiAl LDH pristine structure [248]. The even distribution of elements, which originated from the electrode slurry, including NiAl LDH material, carbon black, and PVDF binder (nickel, aluminum, oxygen, and nitrogen from the active material, and fluor and carbon are from binder and carbon black), confirms a homogenous electrode preparation.

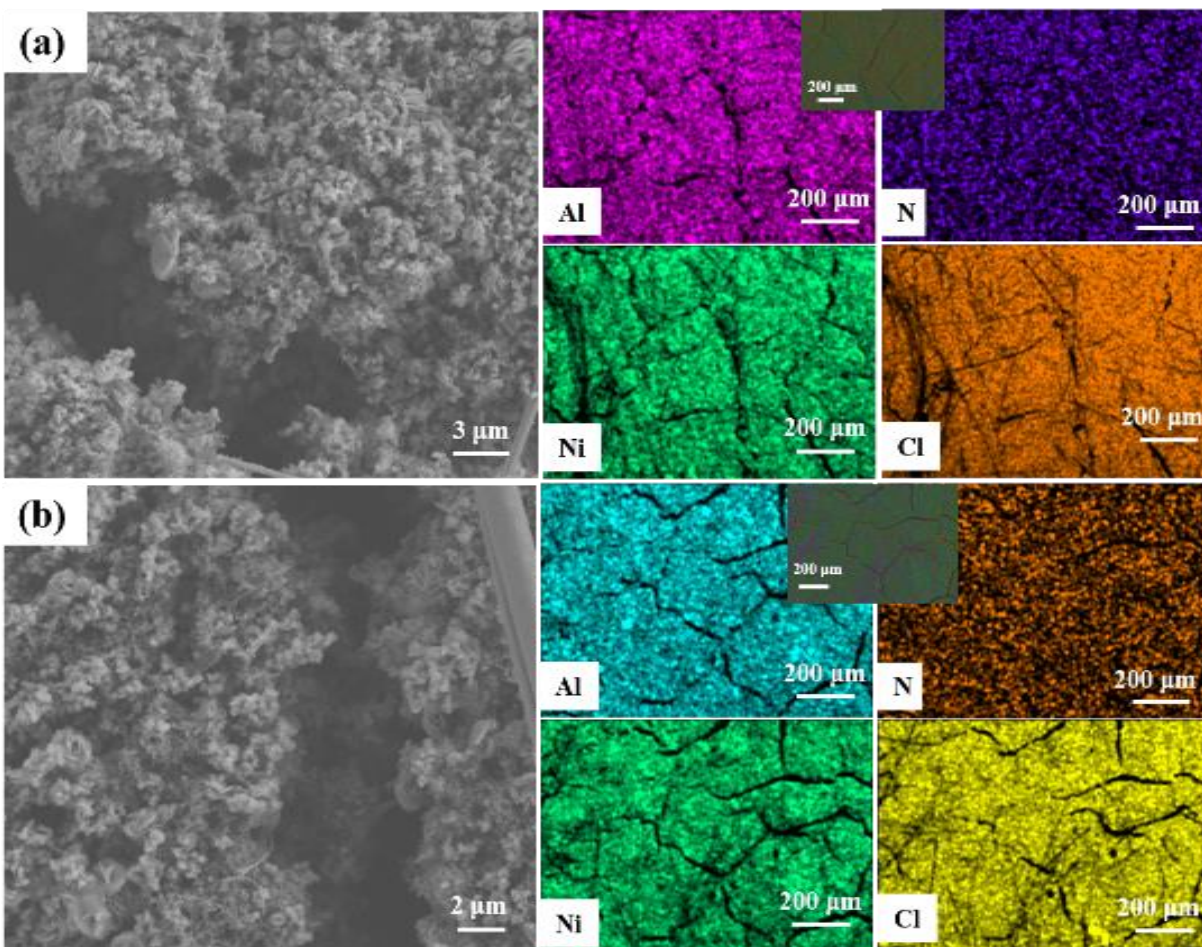


**Figure 6.5.** SEM and EDX mapping of NiAl LDH electrode: (a) discharged to 1.0 V (vs. Li); and (b) charged to 3.0 V (vs. Li).

Furthermore, post-mortem SEM and EDX mapping are applied to illustrate the morphology and homogeneity of the NiAl LDH electrode after the discharge and charge process, respectively (**Figure 6.5**). For the discharged electrode (**Figure 6.5 a**), a distribution of Cl-ion can be observed, ascribed from the chloride-containing electrolyte, and a potential CEI film can be formed during the discharge procedure. Besides, no disintegration nor dramatic morphology change is presented after the first discharge and charge cycle, suggesting the structure remains favorably supportive after discharge and charge cycles.

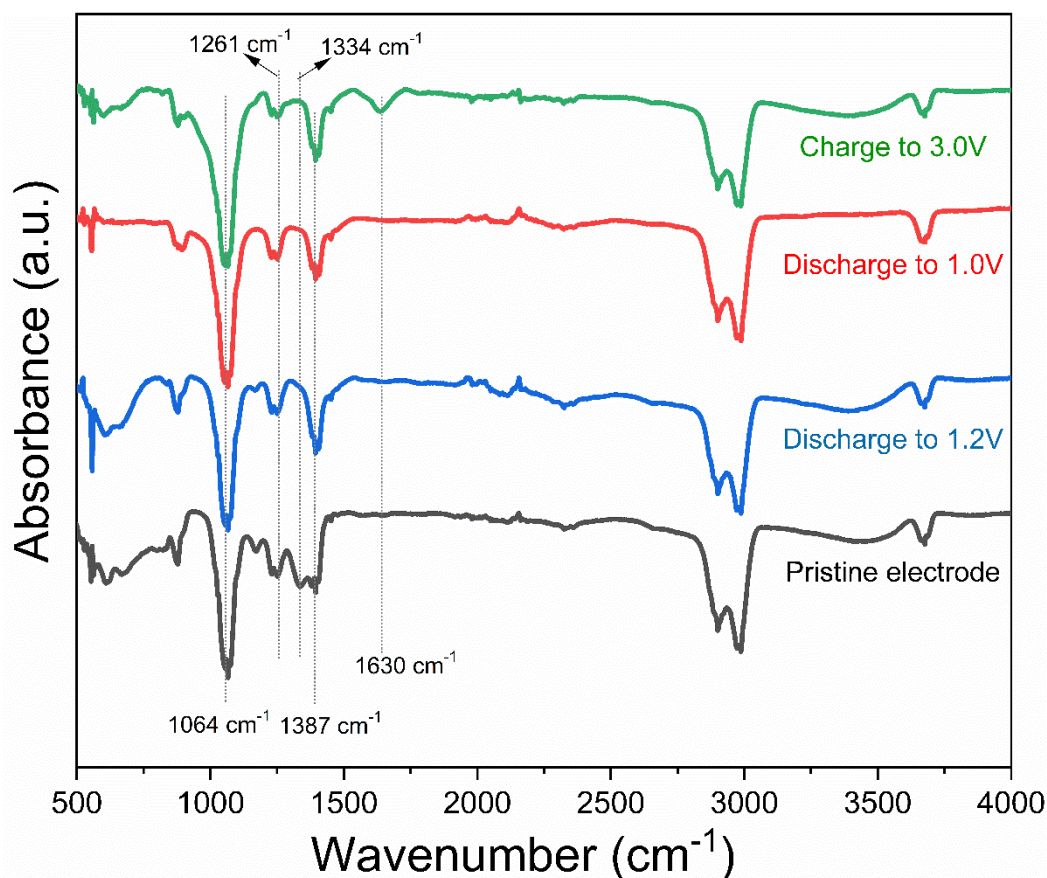


**Figure 6.6.** *Ex-situ* FT-IR of the NiAl LDH electrode for pristine, discharged to 1.2 V, discharged to 1.0 V, and charged to 3.0 V vs. Li, respectively.

*Ex situ* FT-IR measurements were performed further to investigate the insertion mechanism of the NiAl LDH electrode. As shown in **Figure 6.6**, the peak at  $3414\text{ cm}^{-1}$  corresponds to the O-H stretching mode for  $\text{OH}^-$  groups from the LDH layer and water molecules in the interlayer, which is consistent with the bonding vibration behavior of NiAl LDH material. The signal between  $2850\text{--}3050\text{ cm}^{-1}$  can be assigned to  $\text{CH}_3$  and  $\text{CH}_2$  stretching vibrations, possibly owing to the remaining binder solvent NMP during the electrode preparation [127]. The absorption mode at  $1630\text{ cm}^{-1}$  is ascribed to the O-H from the absorbed water molecules in the interlayer [249]. The peak at  $1064\text{ cm}^{-1}$  and  $1387\text{ cm}^{-1}$  correspond to the  $\text{CF}_2$  stretching and  $\text{CH}_2$  stretching bands, which are coming from the PVDF binder [120].

Interestingly, for the *ex-situ* discharged NiAl LDH electrode, the peak at 1334 cm<sup>-1</sup> (ascribed to the stretching modes of NO<sub>3</sub><sup>-</sup> ions (N=O at  $\nu = 1300\sim 1400$  cm<sup>-1</sup>) in the LDH interlayer) disappears, implying the extraction of NO<sub>3</sub><sup>-</sup> from the NiAl LDH structure after discharging[250][251]. Besides, for the electrode charged to 3.0 V, the NO<sub>3</sub><sup>-</sup> peak is not recovered, suggesting an irreversible shuttle of NO<sub>3</sub><sup>-</sup> from the NiAl LDH structure; this irreversible extraction could explain the low initial Coulombic efficiency during the charge-discharge cycling observed in **Figure 6.3**. Interestingly, a very weak band at 1261 cm<sup>-1</sup> corresponding to NO<sub>2</sub><sup>-</sup> [252][253][254], which comes from the reduction of NO<sub>3</sub><sup>-</sup>, anions can be observed. The intensity of this peak weakens observed in the charged electrode, indicating the occurrence of the absorption of NO<sub>2</sub><sup>-</sup> in the discharged electrode.

To get further insight into the anions (Cl<sup>-</sup> ion and NO<sub>3</sub><sup>-</sup> anion) storage mechanism and understanding of the capacity decay of the NiAl LDH electrode on CIBs, *ex-situ* XPS was applied and analyzed. Firstly, the stability of the NiAl LDH electrode in the electrolyte was evaluated by soaking in the 0.5 M Bpy<sub>14</sub>Cl/PC electrolyte for 72 hours. **Figure A 13** presents the XPS survey of the electrode and the one soaked in electrolytes, showing the presence of Ni(2s, 2p, 3p), Al(2s, 2p), O(1s, 2s) and N1s for the active NiAl LDH material, and F1s and C1s for the binder and conductive additive.

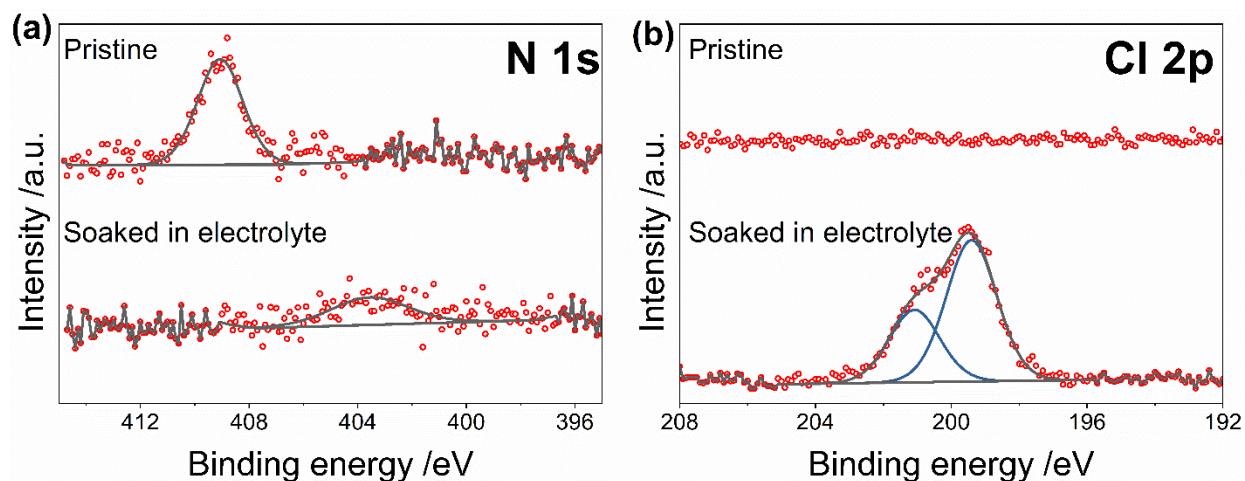


**Figure 6.7.** XPS spectra of: a) N1s and b) Cl2p for pristine and soaked NiAl LDH electrodes.

The XPS spectra of Cl2p and N1s for the pristine and immersed electrodes are shown in **Figure 6.7**. After soaking the electrode in the Cl<sup>-</sup>-containing electrolyte, a peak of Cl<sup>-</sup> appears, which is

fitted with a doublet with binding energy at 199.4 eV ( $2p_{3/2}$ ) and 201.1 eV ( $2p_{1/2}$ ). For the N1s spectrum, the peak at 409.1 eV disappears, while a peak at 403.6 eV appears. The N1s XPS peak at high binding energy (409.1 eV) can be assigned to the  $\text{NO}_3^-$  in the interlayers of the LDH structure, and the N1s peak at 403.1 eV possibly corresponding to the signal from quaternary nitrogen (owns four N–C bonds) [255], which corresponds to the N-containing cation  $\text{Bpy}_{14}^+$  in the electrolyte. After contact with the electrolyte on the NiAl LDH electrode, the electrolyte molecules can be observed. However, the N1s peak at 403.1 eV could also possibly correspond to the signal of  $\text{NO}_2^-$  anion, which is generated from the reduction of  $\text{NO}_3^-$  [243], as clarified in the previous work in chapter 5.3 when NiAl LDH was applied as an electrode on DIB. This indicates the partial dissolution of  $\text{NO}_3^-$  from the NiAl LDH in the 0.5 M  $\text{Bpy}_{14}\text{Cl}/\text{PC}$  electrolyte (forming  $\text{NO}_2^-$ ), which is corresponding to the FT-IR result shown in **Figure 6.6**.

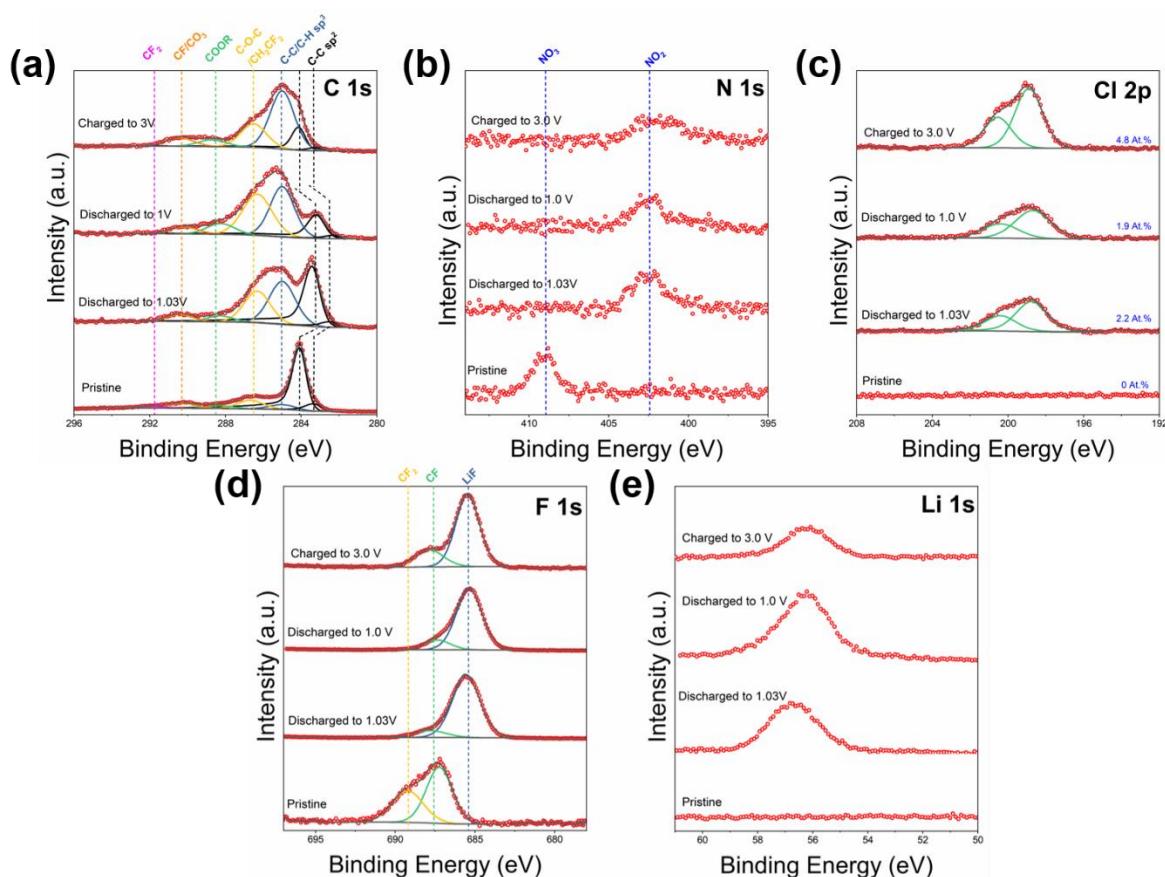


**Figure 6.8.** *Ex-situ* XPS spectra of (a) C1s, (b) N1s, (c) Cl2p, (d) F1s and (e) Li1s of the NiAl LDH electrodes after the discharge and charge process at 10 mA g<sup>-1</sup> within 1.0–3.0 V (*vs.* Li).

To further understand the chemical composition of the CEI film on the NiAl LDH electrode on CIB, *ex-situ* XPS was performed on discharged (to 1.03 V, to 1.00 V, respectively) and charged (to 3.0 V) NiAl LDH electrode at a current density of 10 mA g<sup>-1</sup>, as shown in **Figure 6.8**. For the pristine NiAl LDH electrode, the XPS spectrum of C1s (**Figure 6.8 a**) shows a main peak at 284.1 eV, which originated from the carbon black (C–C sp<sup>2</sup>), and another peak at 285 eV is attributed to the hydrocarbon contamination [210][256]. Besides, the peaks at 286.7, 290.2 and 291.9 eV can be assigned to CH<sub>2</sub>–CF<sub>2</sub>, CF, and CF<sub>2</sub> from the PVDF binder, respectively. Besides, **Figure 6.8 d** shows the F1s spectra of the pristine electrode. Two peaks at 687.2 eV and 689.2 eV correspond to the CF and CF<sub>2</sub> signals, respectively, implying a possible degradation of the PVDF binder [257].

For the electrode discharged to 1.03 V *vs.* Li (which is the potential where the second discharge plateau appears), a N1s peak at 409.1 eV that corresponds to the NO<sub>3</sub><sup>-</sup> from the NiAl LDH structure disappears with the appearance of a new peak at 402.5 eV (**Figure 6.8 b**), which can be ascribed to the NO<sub>2</sub><sup>-</sup> anion of the NiAl LDH electrode. This peak shows the signal of nitrate compound generated from the NO<sub>3</sub><sup>-</sup> irreversibly extracted from the LDH electrode based on the XPS N1s investigation of NiAl LDH on DIBs in chapter 5.3 [243]. The high solubility of NO<sub>2</sub><sup>-</sup> makes NO<sub>2</sub><sup>-</sup> easily migrate from the electrolyte to the NiAl LDH electrode surface. Furthermore, new peaks appear for Cl2p at 198.8 eV (2p<sub>3/2</sub>, **Figure 6.8 c**), for F1s at 685.6 eV (**Figure 6.8 d**) and for Li1s at 56.7 eV (**Figure 6.8 e**). It is worth noting that, based on the observed XPS spectra of Li1s, Li-ion are observed on the *ex-situ* discharged electrode, which comes from the dissolution of LiCl in the Bpy<sub>14</sub>Cl/PC electrolyte and subsequently shuttles to NiAl LDH electrode through electrolyte.

A new F1s peak appears at 685.6 eV, as shown in **Figure 6.8 d**, can be associated with the formation of LiF [248], resulting from a Li-ion shuttle effect from the Li metal electrode and form LiF on the NiAl LDH positive electrode during the discharging process. This is well-amplified in some reports the degradation of PVDF with the reaction with Li to form LiF on LIBs [258][259].

For the NiAl LDH electrode fully discharged to 1.0 V *vs.* Li, a further decrease of the C–C sp<sup>2</sup> peak, which corresponds to the carbon black, can be observed in **Figure 6.8 a**, indicating the cathodic interphase layer is thicker compared to the discharged to 1.03 V electrode [256]. In

addition, the intensity of N1s and Cl2p peaks decreases while the intensity of Li1s and F1s peaks at 56.3 and 685 eV increases compared to the electrode discharged to 1.03 V (*vs.* Li), suggesting a further degradation of PVDF binder and formation of LiF along with the reduction of NO<sub>3</sub><sup>-</sup> from the NiAl LDH structure.

For the charged electrode to 3.0 V (*vs.* Li), the XPS shows the atomic sp<sup>2</sup> C peak increases slightly; while the LiF from F1s spectrum decreases, suggesting a decomposition of the CEI film. On the other hand, the Cl<sup>-</sup> amount doubles in comparison to the fully-discharged electrode, indicating an insertion mechanism of Cl<sup>-</sup> on the LDH electrode. From the last chapter 5, it is investigated that the oxidation of NO<sub>3</sub><sup>-</sup> occurs at around 3.6V (*vs.* Li<sup>+</sup>/Li). NO<sub>3</sub><sup>-</sup> ions are extracted from the NiAl LDH structure and reduced in the electrolyte solution at around 1.6 V (*vs.* Li<sup>+</sup>/Li) from **Figure 5.1 a**. However, in this work, where the NiAl LDH electrode operates at 1.0-3.0 V (*vs.* Li), NO<sub>3</sub><sup>-</sup> oxidation is not reached due to a lower cut-off charge potential. Instead, Cl-ion is inserted into NiAl LDH, and a thick CEI layer is found without a pronounced oxidation process, which corresponds to the CV behavior from **Figure 6.2**.

The *ex-situ* XPS measurements show the surface chemistry for the electrode at different charge-discharge conditions. When the NiAl LDH is discharged to 1.03 V, where a distinctive second plateau starts, a dissolution of LiCl on the Li electrode occurs in the Bpy<sub>14</sub>Cl/PC electrolyte, subsequently causing a shuttle of Li<sup>+</sup> through the electrolyte. This can be the explanation for the long second discharge plateau contributing to a high initial discharge capacity. Besides, a degradation of PVDF and a reduction of NO<sub>3</sub><sup>-</sup> from the NiAl LDH is observed when the electrode is discharged to 1.03 V, which results in the irreversible capacity. The mechanism of the electrode during the charging process can be described as the shuttle of Cl<sup>-</sup> from the electrolyte to the NiAl LDH electrode, which contributes to the charging capacity. Nevertheless, an irreversible degradation of PVDF binder and irreversible NO<sub>3</sub><sup>-</sup> reduction of NiAl LDH material results in a fast capacity decay.

## 6.4 Conclusive aspects: anions storage of NiAl LDH electrode

NiAl LDH with  $\text{NO}_3^-$  interlayer anion was, for the first time, directly applied as a positive electrode on CIB in this work. To realize the feasibility of this system, firstly, a compatible configuration with suitable reference electrodes and stability potential window for the 0.5 M Bpy<sub>14</sub>Cl/PC electrolyte on CIBs was screened out by electrochemical methods. Ag was investigated as a stable reference electrode for the CIB system in the 0.5 M Bpy<sub>14</sub>Cl/PC electrolyte. The broader potential window of 1.0-3.0 V (vs. Li) was evaluated and adopted as a stable operating window for the Ag RE in the Bpy<sub>14</sub>Cl/PC electrolyte.

With the optimized configuration, the  $\text{NO}_3^-$ -containing NiAl LDH was applied as a positive electrode on CIB in 0.5 M Bpy<sub>14</sub>Cl/PC electrolyte at a potential window of 1.0-3.0 V (vs. Li). The NiAl LDH electrode gave a maximum initial discharge capacity of 695 mAh g<sup>-1</sup> with an ICE of 28.0% at a current density of 10 mA g<sup>-1</sup>, and the capacity decreased to 56.8 mAh g<sup>-1</sup> after 15 cycles. The elucidation of the irreversible behavior and the anion shuttle mechanism of the electrode on CIB during the first cycle has been further illustrated. *Ex-situ* SEM/EDX and FT-IR reveal the participation of Cl-ion and the extraction/insertion of  $\text{NO}_3^-$  from the NiAl LDH structure during the discharge/charge process. Furthermore, a shuttle of Li-ion and extraction of  $\text{NO}_3^-$  during the first discharging process and an insertion of Cl-ion during the charging process is elucidated by *ex-situ* XPS, which can be accounted for the high initial discharge capacity. While the degradation of PVDF binder and the reduction of the interlayer anion ( $\text{NO}_3^-$ ) from NiAl LDH structure within the Bpy<sub>14</sub>Cl/PC electrolyte need to be critically considered while developing new positive electrode materials for CIBs.

## 7 Conclusion

This thesis systematically focuses on the study of Ni-Al layered double hydroxide as electrode material for rechargeable LIBs and post-lithium ion batteries (DIBs and CIBs), from electrochemical performance investigation to energy storage mechanism elucidation. NiAl LDH material with  $\text{NO}_3^-$  as an interlayer anion was synthesized by a facile hydrothermal method. The NiAl LDH shows a flower-like structure arranged in a concentric form in a highly nanocrystallized arrangement with a large interlayer distance of 8.7 Å and a high specific surface area.

In **chapter 4** reported for the first time that NiAl LDH material with  $\text{NO}_3^-$  as the interlayer anion was applied as a negative electrode on LIBs. The electrochemical tests were conducted to understand further the effect of the binder (PVDF and SA) and the potential cut-off on the performance of LIBs. The results of electrochemical characterizations demonstrated that the NiAl LDH materials could work as negative electrodes with a very high specific capacity in the potential range of 0.01-3.0 V (*vs.*  $\text{Li}^+/\text{Li}$ ). The NiAl LDH electrode with SA binder shows a high capacity and more stable cycling ability than the electrode with PVDF binder, which delivers an initial discharge capacity of 2586  $\text{mAh g}^{-1}$  at 0.05  $\text{A g}^{-1}$  and a reversible capacity of 697  $\text{mAh g}^{-1}$  after 400 cycles at 0.5  $\text{A g}^{-1}$ . Under the same conditions, the PVDF-based electrode retains only 15.6% with a capacity of 182  $\text{mAh g}^{-1}$  and 8.5% with a capacity of 121  $\text{mAh g}^{-1}$ , respectively. To better understand the influence of binders on the electrochemical cycling ability, SEI is investigated through *in operando* synchrotron diffraction and X-ray photoelectron spectroscopy. The results show a higher amount of lithium oxide component at the surface of the NiAl LDH-SA electrode. Since  $\text{Li}_2\text{O}$  is less soluble in carbonate-based solvents than LiF (detected as a major SEI component in the PVDF-based electrode), the resulting SEI should be more stable and explains the better cycling ability of the SA-based electrode. To understand the redox processes occurring on the NiAl LDH electrode during the first cycle, XANES measurements were performed on *ex-situ* samples. *Ex-situ* XANES confirms that the NiAl LDH stores  $\text{Li}^+$  *via* a conversion mechanism ( $\text{Ni}^{2+}$  to  $\text{Ni}^0$ ) in the potential range of 0.01–3.0 V (*vs.*  $\text{Li}^+/\text{Li}$ ). The excellent  $\text{Li}^+$ -storage performance is attributed to the expanded interlayer space of the NiAl LDH pillared by the interlayer nitrates, providing effective paths for  $\text{Li}^+$  diffusion.

In **chapter 5**, a novel DIB was designed by a multi-ion co-shuttle strategy, in which the NiAl LDH as a positive electrode and Li metal as a negative electrode operating in a formulated bi-salts-

based electrolyte with LiTFSI and LiNO<sub>3</sub>. Electrochemical tests exhibit that the NiAl LDH electrode achieves an initial discharge capacity of 589 mAh g<sup>-1</sup> at 20 mA g<sup>-1</sup> within a working potential window of 0.7-4.0 V (*vs.* Li<sup>+</sup>/Li), and a 26.0% capacity retention at 50 mA g<sup>-1</sup> over 100 cycles. Based on the *ex-situ* FT-IR and *ex-situ* XPS characterization, a stepwise storage mechanism of Li<sup>+</sup> and NO<sub>3</sub><sup>-</sup> ions *via* insertion/extraction chemistry at different charge cut-off potentials was illustrated. Reversible oxidation and reduction of interlayer anion NO<sub>3</sub><sup>-</sup> from NiAl LDH structure in the electrolyte is elucidated. Furthermore, the redox chemistry in the NiAl LDH electrode was investigated by *in-situ* XAS. No dramatic Ni redox was observed during the first discharge-charge cycle of the NiAl LDH electrode, which is owing to compensation to insert Li-ion by NO<sub>3</sub><sup>-</sup> anion that exchanges between the NiAl LDH electrode and electrolyte during the charge-discharge process.

In **chapter 6**, a compatible and optimized configuration for a CIB system was screened for NiAl LDH electrode in the 0.5 M Bpy<sub>14</sub>Cl/PC electrolyte with a stable and broad potential window of 1.0-3.0 V (*vs.* Li). NiAl LDH with NO<sub>3</sub><sup>-</sup> as its interlayer is applied as the positive electrode on this optimized CIB system. The electrochemical performance was investigated. The NiAl LDH electrode delivers a maximum initial discharge capacity of 695 mAh g<sup>-1</sup> with an ICE of 28.0% at a current density of 10 mA g<sup>-1</sup>. Nevertheless, it shows an undesirable cycling instability with an irreversible capacity for 15 cycles. The understanding of the anion shuttle mechanism for the first cycle was subsequently revealed by means of *ex-situ* SEM/EDX and FT-IR. An irreversible reduction of NO<sub>3</sub><sup>-</sup> of NiAl LDH structure in the electrolyte mechanism is disclosed. During the first discharging process, NO<sub>3</sub><sup>-</sup> is extracted from the NiAl LDH electrode along with an unexpected Li-ion insertion, and during the following charging process, Cl-ion is inserted into the NiAl LDH electrode.

In summary, this thesis is dedicated to the direct application of NiAl LDH (with NO<sub>3</sub><sup>-</sup> anion in the interlayer) as electrode material for lithium and post-lithium storage systems (*i.e.*, LIBs, DIBs and CIBs). The electrochemical performance and corresponding storage mechanism of NiAl LDH electrode on the different three ion batteries were investigated and elucidated; the NiAl LDH electrode on LIBs shows different Li-ion storage mechanism when different cut-off discharge potential was implemented, and improved electrochemical performance was found when SA was introduced as binder compared to conventional PVDF binder. Besides, with the addition of LiNO<sub>3</sub> in the LiTFSI electrolyte, the NiAl LDH electrode shows prominent dual-ion storage performance,

which is enabled by a broad charge potential of 4.0 V (vs.  $\text{Li}^+/\text{Li}$ ). Furthermore, the NiAl LDH electrode shows a large initial discharge capacity on CIBs; such irreversible capacity was elucidated, which is owing to the irreversible reduction of  $\text{NO}_3^-$  from the NiAl LDH structure. The unexpected participation of Li-ion in the anion-shuttle system is revealed for the first time. Nevertheless, the cycling performance of LDH electrode material needs further improvement.

## 8 Outlook

In this thesis, the direct application of NiAl LDH material as the electrode on Li-ion and post-Li-ion batteries has proven to be highly feasible with high specific capacity and outstanding ion accommodation ability. In addition, the advantages of LDH materials, such as economical cost, readily available, and simple preparation, make LDHs a class of promising electrode materials.

Research based on the application of LDH electrode materials in the field of battery storage is still in its infancy. The overall battery performance of LDH electrodes calls for more investigation to be improved. Besides, electrolytes and electrode additives that are required in the battery preparation process also need in-depth research to be suitable for LDH. In addition, the study on the energy storage mechanism of LDH materials is limited to date. As the theoretical basis for improving performance, future research on the mechanism of LDH materials needs more effort.

Future studies of LDH electrode materials should focus on improving the overall battery performance from the structure design and modification of the LDH materials, the overall optimization of the battery configurations, to the understanding of the energy storage mechanism.

### 1. Modification of LDH materials

Future improvements to the structure of LDH materials should focus on solving the problem of irreversible capacity loss, which is an overall problem for LDH materials. For example, a combination with carbon-based materials for improved cyclic performance is worth to be taken into consideration. In addition, besides from the binary LDH materials, ternary LDH materials can be good candidates by introducing additional metals, which may lead to a smoother insertion/extraction of large-size anions with increased  $d$ -space, eventually improving the cyclic stability and energy density.

### 2. The overall design on batteries configuration

Good compatibility of the LDH electrode materials with the batteries' other components guarantees superior and stable battery performance. The choice of electrolyte is crucial to the battery's performance. However, no systematic research on electrolytes with LDH electrodes has been reported so far. Future research should emphasize investigating suitable electrolytes and studying the influence of electrolytes on LDH electrodes. Apart from this, research on selecting

other batteries' components, such as electrolyte additives, binders, and current collectors, is also valuable for improving the performance of LDH electrodes.

### 3. Research on the energy storage mechanism

The energy storage mechanism of LDH electrode materials, especially in post-Li batteries, has not been reported in detail. For example, the role of each metal in LDH materials should be revealed in future studies. Additionally, the energy storage mechanism of LDH during long cycling needs more research to disclose.

### 4. Other applications

Due to the distinct “memory effect” of LDH materials, they have been widely used in water purification. After pollutant removal, the recovering ability of the layered structure realizes LDH materials to be repeatedly used. A re-energy strategy using such kind of pre-used LDH materials on ion-storage batteries can open up a broad possibility of sustainable and environmentally friendly ion-storage batteries.

## 9 References

1. Walter M, Kovalenko M V., Kravchyk K V. (2020). *New J Chem* 44:1677–1683.
2. Winter M, Brodd RJ (2004). *Chem Rev* 104:4245–4270.
3. Manthiram A (2017). *ACS Cent Sci* 3:1063–1069.
4. Sui Y, Liu C, Masse RC, *et al.* (2020). *Energy Storage Mater* 25:1–32.
5. Gschwind F, Euchner H, Rodriguez-Garcia G (2017). *Eur J Inorg Chem* 2017:2784–2799.
6. Karkera G, Reddy MA, Fichtner M (2021). *J Power Sources* 481:228877.
7. Wang Q, O'Hare D (2012). *Chem Rev* 112:4124–4155.
8. Dunn B, Kamath H, Tarascon JM (2011). *Science* (80- ) 334:928–935.
9. Ricart JE, Rey C (2022). *Sustain* 14:1–11.
10. Steven C, Yi C, Nian L (2017). *Nature Materials* 16:16–22.
11. Green C (1992). *Clim Change* 22:265–291.
12. Crutzen PJ, Mosier AR, Smith KA, Winiwarter W (2016). 227–238.
13. Dorian JP, Franssen HT, Simbeck DR (2006). *Energy Policy* 34:1984–1991.
14. Douglas NG, Saluja GS (1995). *Renew Energy* 6:701–711.
15. Safaei Mohamadabadi H, Tichkowsky G, Kumar A (2009). *Energy* 34:112–125.
16. Qi J, Zhang W, Cao R, *Adv. Energy Mater* (2018). 8:1701620.
17. Armaroli N, Balzani V (2011). *Energy Environ Sci* 4:3193–3222.
18. Han S, Wu D, Li S, *et al.* (2014). *Adv Mater* 26:849-864.
19. Ouyang CY, Chen LQ (2013). *Sci China Physics, Mech Astron* 56:2278–2292.
20. Bernardes AM, Espinosa DCR, Tenório JAS (2004). *J Power Sources* 130:291–298.
21. Weber AZ, Mench MM, Meyers JP, *et al.* (2011). *J Appl Electrochem* 41:1137–1164.
22. Goodenough JB, Park KS (2013). *J Am Chem Soc* 135:1167–1176.
23. Brand MJ, Hofmann MH, Schuster SS, *et al.* (2018). *IEEE Trans Veh Technol* 67:10438–10445.
24. Li M, Lu J, Chen Z, Amine K (2018). *Adv Mater* 30:1800561.
25. Liu C, Li F, Lai-Peng M, Cheng HM (2010). *Adv Mater* 22:E28–E62.
26. Etacheri V, Marom R, Elazari R, *et al.* (2011). *Energy Environ Sci* 4:3243–3262.
27. Kubota K, Dahbi M, Hosaka T, *et al.* (2018). *Chem Rec* 18:459–479.
28. Mashtalir O, Nguyen M, Bodoïn E, *et al.* (2018). *ACS Omega* 3:181–187.
29. Anderman M (1994). *Proc Annu Batter Conf* 12–19.

30. Ouchi T, Young KH, Moghe D (2016). *Batteries* 2:21.
31. Ozawa K (1994). *Solid State Ionics* 69:212–221.
32. Delmas C, Carlier D, Guignard M (2021). *Adv Energy Mater* 11:001201.
33. Yang B, Tamirat AG, Bin D, *et al.* (2021). *Adv Funct Mater* 31:2104543.
34. Li G, Yang Z, Yin Z, *et al.* (2019). *J Mater Chem A* 7:15541–15563.
35. De Las Casas C, Li W (2012). *J Power Sources* 208:74–85.
36. Malini R, Uma U, Sheela T, *et al.* (2009). *Ionics (Kiel)* 15:301–307.
37. Li L, Meng F, Jin S (2012). *Nano Lett* 12:6030–6037.
38. Wakihara M (2001). *Mater Sci Eng R Reports* 33:109–134.
39. Fan H, Liu X, Luo L, *et al.* (2022). *ACS Appl Mater Interfaces* 14:574–580.
40. Smart MC, Ratnakumar B V., Whitcanack LD, *et al.* (2003). *J Power Sources* 119–121:349–358.
41. Moumouzias G, Ritzoulis G, Siapkias D, Terzidis D (2003). *J Power Sources* 122:57–66.
42. Lu J, Zhou C, Liu Z, *et al.* (2016). *Electrochim Acta* 212:553–560.
43. Daniel C, Mohanty D, Li J, Wood DL (2014). *AIP Conf Proc* 1597:26–43.
44. Liu S, Wang B, Zhang X, *et al.* (2021). *Matter* 4:1511–1527.
45. Zhang N, Li J, Li H, *et al.* (2018). *Chem Mater* 30:8852–8860.
46. Shizuka K, Kobayashi T, Okahara K, *et al.* (2005). *J Power Sources* 146:589–593.
47. Wang J, Qiu B, Cao H, *et al.* (2012). *J Power Sources* 218:128–133.
48. Liu H, Cao Q, Fu LJ, *et al.* (2006). *Electrochem commun* 8:1553–1557.
49. Striebel K, Shim J, Sierra A, *et al.* (2005). *J Power Sources* 146:33–38.
50. Li Z, Zhang D, Yang F (2009). *J Mater Sci* 44:2435–2443.
51. Islam MS, Fisher CAJ (2014). *Chem Soc Rev* 43:185–204.
52. Jia J, Li BJ, Duan S, *et al.* (2019). *Nanoscale* 11:20307–20314.
53. Kravchyk K V., Kovalenko M V. (2019). *Adv Energy Mater* 9:1901749.
54. Judez X, Eshetu GG, Li C, *et al.* (2018). *Joule* 2:2208–2224.
55. Winter M, Besenhard JO, Spahr ME, Novák P (1998). *Adv Mater* 10:725–763.
56. Kawata K (2001). *Chem Rec* 1:406–413.
57. Zhong Y, Yang M, Zhou X, Zhou Z (2015). *Mater Horizons* 2:553–566.
58. Palacín MR (2009). *Chem Soc Rev* 38:2565–2575.
59. Buiel E, Dahn JR (1999). *Electrochim Acta* 45:121–130.
60. Yu H, Dong X, Pang Y, *et al.* (2017). *Electrochim Acta* 228:251–258.

61. Ronci F, Reale P, Scrosati B, *et al.* (2002). *J Phys Chem B* 106:3082–3086.
62. Nitta N, Wu F, Lee JT, Yushin G (2015). *Mater Today* 18:252–264.
63. Toigo C, Arbizzani C, Pettinger KH, Biso M (2020). *Molecules* 25:2443.
64. Zhang H, Yang Y, Xu H, *et al.* (2022). *InfoMat* 4:1–29.
65. Geng Q, Cao L, Kong X, *et al.* (2016). *Mater Sci Eng B Solid-State Mater Adv Technol* 207:13–17.
66. Fu QW, Jiang XY (2016). *Mater Sci Forum* 847:29–32.
67. Piernas-Muñoz MJ, Trask SE, Dunlop AR, *et al.* (2019). *J Power Sources* 441:227080.
68. Song H, Wang HX, Lin Z, *et al.* (2016). *Adv Funct Mater* 26:524–531.
69. Zhao X, Lehto VP (2021). *Nanotechnology* 32:042002.
70. Lee SW, McDowell MT, Berla LA, *et al.* (2012). *Proc Natl Acad Sci U S A* 109:4080–4085.
71. Choi NS, Yew KH, Choi WU, Kim SS (2008). *J Power Sources* 177:590–594.
72. Laik B, Eude L, Pereira-Ramos JP, *et al.* (2008). *Electrochim Acta* 53:5528–5532.
73. Lu Y, Yu L, Lou XW (David) (2018). *Chem* 4:972–996.
74. McNulty D, Geaney H, O’Dwyer C (2017). *Sci Rep* 7:1–13.
75. Hendon CH, Tiana D, Walsh A (2012). *Phys Chem Chem Phys* 14:13120–13132.
76. Li Q, Zhang H, Lou S, *et al.* (2017). *Ceram Int* 43:11998–12004.
77. Li Z, Hu X, Shi Z, *et al.* (2020). *Appl Surf Sci* 531:147290.
78. Voskanyan AA, Ho CK, Chan KY (2019). *J Power Sources* 421:162–168.
79. Wang G, Wang H, Cai S, *et al.* (2013). *J Power Sources* 239:37–44.
80. Huang XL, Wang RZ, Xu D, *et al.* (2013). *Adv Funct Mater* 23:4345–4353.
81. Liang J, Li F, Cheng HM (2016). *Energy Storage Mater* 4:A1–A2.
82. Venkatraman S, Subramanian V, Gopu Kumar S, *et al.* (2000). *Electrochem commun* 2:18–22.
83. Christmann P, Gloaguen E, Labbé JF, *et al.* (2015). *Lithium Process Chemistry*. 1–40.
84. Sun X, Hao H, Zhao F, Liu Z (2018). *Environ Sci Technol* 52:2827–2834.
85. Liu T, Tan W, Tang X, *et al.* (2021). *Renew Sustain Energy Rev* 151:111521.
86. Zeng X, Li J (2013). *Resour Conserv Recycl* 80:58–63.
87. Friedman-Rudovsky J (2011). *Science (80- )* 334:896–897.
88. Yang K, Liu Q, Zheng Y, *et al.* (2021). *Angew Chemie - Int Ed* 60:6326–6332.
89. Sui Y, Liu C, Masse RC, *et al.* (2020). *Energy Storage Mater* 25:1–32.

90. Placke T, Heckmann A, Schmuck R, *et al.* (2018). *Joule* 2:2528–2550.
91. Rüdorff W, Hofmann U (1938). *Zeitschrift für Anorg und Allg Chemie* 238.
92. Fan L, Liu Q, Chen S, *et al.* (2017). *Adv Energy Mater* 7:1–8.
93. Ji B, Zhang F, Song X, Tang Y (2017). *Adv Mater* 29:1700519.
94. Jiang H, Wei Z, Ma L, *et al.* (2019). *Angew Chemie - Int Ed* 58:5286–5291.
95. Wang S, Jiao S, Tian D, *et al.* (2017). *Adv Mater* 29:1606349.
96. Liu Q, Wang Y, Yang X, *et al.* (2021). *Chem* 1–29.
97. Kravchyk K V., Kovalenko M V. (2019). *Adv Energy Mater* 9:1901749.
98. Wang H guo, Wang Y, Wu Q, Zhu G (2022). *Mater Today* 52:269–298.
99. Beltrop K, Meister P, Klein S, *et al.* (2016). *Electrochim Acta* 209:44–55.
100. Wang F, Liu Z, Zhang P, *et al.* (2017). *Small* 13:1–7.
101. Zhang X, Tang Y, Zhang F, Lee CS (2016). *Adv Energy Mater* 6:1502588.
102. Qin P, Wang M, Li N, *et al.* (2017). *Adv Mater* 29:1606805.
103. Qi X, Blizanac B, DuPasquier A, *et al.* (2014). *Phys Chem Chem Phys* 16:25306–25313.
104. Wang YY, Song X, Liu S, *et al.* (2021). *ACS Appl Mater Interfaces* 13:56233–56241.
105. Jiang H, Wei Z, Ma L, *et al.* (2019). *Angew Chemie* 131:5340–5345.
106. Wang K, Wang N, Li X, *et al.* (2019). *Carbon N Y* 142:401–410.
107. Chan CY, Lee PK, Xu Z, Yu DYW (2018). *Electrochim Acta* 263:34–39.
108. Liu Q, Wang H, Jiang C, Tang Y (2019). *Energy Storage Mater* 23:566–586.
109. Kim JK, Lee E, Kim H, *et al.* (2015). *ChemElectroChem* 2:328–332.
110. Zhao X, Ren S, Bruns M, Fichtner M (2014). *J Power Sources* 245:706–711.
111. Chen F, Leong ZY, Yang HY (2017). *Energy Storage Mater* 7:189–194.
112. Lan Y, Liu Y, Li J, *et al.* (2021). *Adv Sci* 8:1–25.
113. Gschwind F, Euchner H, Rodriguez-Garcia G (2017). *Eur J Inorg Chem* 2017:2784–2799.
114. Gür TM (2018). *Energy Environ Sci* 11:2696–2767.
115. Poullikkas A (2013). *Renew Sustain Energy Rev* 27:778–788.
116. Zhao X, Ren S, Bruns M, Fichtner M (2014). *J Power Sources* 245:706–711.
117. Zhao X, Li Q, Zhao-Karger Z, *et al.* (2014). *ACS Appl Mater Interfaces* 6:10997–11000.
118. Zhao X, Zhao-Karger Z, Wang D, Fichtner M (2013). *Angew Chemie* 125:13866–13869.
119. Gao P, Reddy MA, Mu X, *et al.* (2016). *Angew Chemie* 128:4357–4362.
120. Gao P, Zhao X, Zhao-Karger Z, *et al.* (2014). *ACS Appl Mater Interfaces* 6:22430–22435.
121. Zhao X, Zhao Z, Yang M, *et al.* (2017). *ACS Appl Mater Interfaces* 9:2535–2540.

## References

122. Gschwind F, Steinle D, Sandbeck D, *et al.* (2016). *ChemistryOpen* 5:525–530.
123. Gao P, Zhao X, Zhao-Karger Z, *et al.* (2014). *ACS Appl Mater Interfaces* 6:22430–22435.
124. Zhao X, Li Q, Zhao-Karger Z, *et al.* (2014). *ACS Appl Mater Interfaces* 6:10997–11000.
125. Zhao X, Zhao-Karger Z, Wang D, Fichtner M (2013). *Angew Chemie* 125:13866–13869.
126. Zhao X, Zhao-Karger Z, Wang D, Fichtner M (2013). *Angew Chemie - Int Ed* 52:13621–13624.
127. Yu T, Li Q, Zhao X, *et al.* (2017). *ACS Energy Lett* 2:2341–2348.
128. Xie J, Lu YC (2020). *Nat Commun* 11:9–12.
129. Manthiram A (2020). *Nat Commun* 11:1–9.
130. Long X, Wang Z, Xiao S, *et al.* (2016). *Mater Today* 19:213–226.
131. Shao M, Zhang R, Li Z, *et al.* (2015). *Chem Commun* 51:15880–15893.
132. Tan C, Cao X, Wu XJ, *et al.* (2017). *Chem Rev* 117:6225–6331.
133. Shao M, Zhang R, Li Z, *et al.* (2015). *Chem Commun* 51:15880–15893.
134. Feng J, He Y, Liu Y, *et al.* (2015). *Chem Soc Rev* 44:5291–5319.
135. Song F, Hu X (2014). *Nat Commun* 5:4477.
136. Mishra G, Dash B, Pandey S (2018). *Appl Clay Sci* 153:172–186.
137. Fan G, Li F, Evans DG, Duan X (2014). *Chem Soc Rev* 43:7040–7066.
138. Lai F, Miao YE, Zuo L, *et al.* (2016). *Small* 12:3235–3244.
139. Patel R, Park JT, Patel M, *et al.* (2017). *J Mater Chem A* 6:12–29.
140. Mishra G, Dash B, Sethi D, *et al.* (2017). *Environ Eng Sci* 34:516–527.
141. Zubair M, Daud M, McKay G, *et al.* (2017). *Appl Clay Sci* 143:279–292.
142. Li X, Fortunato M, Maria A, *et al.* (2021). *J Solid State Electrochem.* 26:49-61.
143. Li X, Du D, Zhang Y, *et al.* (2017). *J Mater Chem A* 5:15460–15485.
144. Zhou L, Shao M, Wei M, Duan X (2017). *J Energy Chem* 26:1094–1106.
145. Liao F, Zhao X, Yang G, *et al.* (2021). *J Alloys Compd* 872:159649.
146. Wang X, Li X, Du X, *et al.* (2017). *Electroanalysis* 29:1286–1293.
147. Zhao C, Tian S, Nie P, *et al.* (2020). *Ionics (Kiel)* 26:1389–1396.
148. Sanati S, Rezvani Z (2018). *Ultrason Sonochem* 48:199–206.
149. Li G, Zhang X, Qiu D, *et al.* (2019). *Adv Electron Mater* 5:1–10.
150. Loh PY, Lee KK, Ng Y, *et al.* (2014). *Electrochem commun* 43:9–12.
151. Liu N, Lin J, Wu J, *et al.* (2020). *Electrochim Acta* 336:135550.
152. Liu X, Zhang L, Gao X, *et al.* (2019). *ACS Appl Mater Interfaces* 11:23236–23243.

153. Li XD, Yang WS, Li F, *et al.* (2006). *J Phys Chem Solids* 67:1286–1290.
154. Shi L, Chen Y, He R, *et al.* (2018). *Phys Chem Chem Phys* 20:16437–16443.
155. Zhang S, Zhang L, Xu G-C, *et al.* (2020). *New J Chem* 0–5.
156. Li X, Guan C, Hu Y, Wang J (2017). *ACS Appl Mater Interfaces* 9:26008–26015.
157. Wang S, Duan X, Gao T, *et al.* (2020). *J Electrochem Soc* 167:160550.
158. Yin Q, Luo J, Zhang J, *et al.* (2020). *J Mater Chem A* 8:12548–12555.
159. Yin Q, Luo J, Zhang J, *et al.* (2020). 12548–12555.
160. Yin Q, Rao D, Zhang G, *et al.* (2019). *Adv Funct Mater* 29:1–9.
161. Yin Q, Luo J, Zhang J, *et al.* (2020). *Adv Funct Mater* 30:1907448.
162. Yin Q, Rao D, Zhang G, *et al.* (2019). *Adv Funct Mater* 29:1900983.
163. Petrovic S (2021). ISBN 978-3-030-61562-8.
164. Palacin MR (2021). *Accounts Mater Res* 2:319–326.
165. Guerfi A, Kaneko M, Petitclerc M, *et al.* (2007). *J Power Sources* 163:1047–1052.
166. Lestriez B (2010). *Comptes Rendus Chim* 13:1341–1350.
167. Lopez J, Mackanic DG, Cui Y, Bao Z (2019). *Nat Rev Mater* 4:312–330.
168. Chou SL, Pan Y, Wang JZ, *et al.* (2014). *Phys Chem Chem Phys* 16:20347–20359.
169. Shi Y, Zhou X, Yu G (2017). *Acc Chem Res* 50:2642–2652.
170. Yan X, Zhang Y, Zhu K, *et al.* (2014). *J Power Sources* 246:95–102.
171. Guo X, Wang Y, Qin Y, *et al.* (2020). *Int J Biol Macromol* 162:618–628.
172. Bigoni F, De Giorgio F, Soavi F, Arbizzani C (2017). *J Electrochem Soc* 164:A6171–A6177.
173. Kovalenko I, Zdyrko B, Magasinski A, *et al.* (2011). *Science* (80- ) 334:75–79.
174. Feng J, Wang L, Li D, *et al.* (2018). *Prog Nat Sci Mater Int* 28:205–211.
175. Ling L, Bai Y, Wang Z, *et al.* (2018). *ACS Appl Mater Interfaces* 10:5560–5568.
176. Mayer JK, Almar L, Asylbekov E, *et al.* (2020). *Energy Technol* 8:1–11.
177. Deng K, Zeng Q, Wang D, *et al.* (2020). *Energy Storage Mater* 32:425–447.
178. Bard AJ, Faulkner LR (2001). ISBN: 978-0-471-04372-0, 2nd ed.
179. Xu K (2004). *Chem Rev* 104:4303–4417.
180. Sylla S, Sanchez JY, Armand M (1992). *Electrochim Acta* 37:1699–1701.
181. Hu X, Chen F, Wang S, *et al.* (2019). *ACS Appl Mater Interfaces* 11:9144–9148.
182. Yu T, Zhao X, Ma L, Shen X (2017). *Mater Res Bull* 96:485–490.
183. Wu L, Chen Z, Ma X (2019). *Int J Electrochem Sci* 14:2414–2421.

## References

184. Chen C, Yu T, Yang M, *et al.* (2019). *Adv Sci* 6:1–12.
185. Karkera G, Reddy MA, Fichtner M (2021). *J Power Sources* 481:228877.
186. Yamada M, Watanabe T, Gunji T, *et al.* (2020). *Electrochem* 1:124–159.
187. Talha M, Behera CK, Sinha OP (2013). *Mater Sci Eng C* 33:3563–3575.
188. Myung ST, Hitoshi Y, Sun YK (2011). *J Mater Chem* 21:9891–9911.
189. Zhu P, Gastol D, Marshall J, *et al.* (2021). *J Power Sources* 485:229321.
190. AJ Torriero A (2019). *Med Anal Chem Int J* 3:2–4.
191. Snook GA, Best AS, Pandolfo AG, Hollenkamp AF (2006). *Electrochem commun* 8:1405–1411.
192. Gritzner G, Kůta J (1984). *Electrochim Acta* 29:869–873.
193. Liu H, Yu T, Su D, *et al.* (2017). *Ceram Int* 43:14395–14400.
194. Arquitectura EY, Introducci TI, 赫晓霞, *et al.* (2015). *Acta Univ Agric Silvic Mendelianae Brun* 53:1689–1699.
195. Scofield JH (1976). *J Electron Spectros Relat Phenomena* 8:129–137.
196. Li X, Yu L, Wang G, *et al.* (2017). *Electrochim Acta* 255:15–22.
197. Tyagi A, Myung Y, Tripathi KM, *et al.* (2020). *Electrochim Acta* 334:135590.
198. Shabanian M, Hajibeygi M, Raeisi A (2020). Elsevier Ltd 77-101.
199. Lim SY, Lee JH, Kim S, *et al.* (2017). *ACS Energy Lett* 2:998–1004.
200. Sai Gautam G, Canepa P, Richards WD, *et al.* (2016). *Nano Lett* 16:2426–2431.
201. Roberts MW, Smart RSC (1984). *J Chem Soc Faraday Trans 1 Phys Chem Condens Phases* 80:2957–2968.
202. Moroney LM, Smart RSC, Roberts MW (1983). *J Chem Soc Faraday Trans 1 Phys Chem Condens Phases* 79:1769–1778.
203. Liu S, Lee SC, Patil U, *et al.* (2017). *J Mater Chem A* 5:1043–1049.
204. Greczynski G, Hultman L (2020). *Angew Chemie* 132:5034–5038.
205. Zhang R, Xue Z, Qin J, *et al.* (2020). *J Energy Chem* 50:143–153.
206. Yao J, Li Y, Huang R, *et al.* (2020). *Ionics (Kiel)* 27:65–74.
207. Zhai Z, Liu Q, Zhu Y, *et al.* (2019). *J Alloys Compd* 775:1316–1323.
208. Bai Z, Ju Z, Guo C, *et al.* (2014). *Nanoscale* 6:3268–3273.
209. Sarkar J, Bhattacharyya S (2012). *Arch Thermodyn* 33:23–40.
210. Gieu JB, Courrèges C, El Ouatani L, *et al.* (2016). *J Power Sources* 318:291–301.
211. Leroy S, Blanchard F, Dedryvère R, *et al.* (2005). *Surf Interface Anal* 37:773–781.

212. Buqa H, Holzapfel M, Krumeich F, *et al.* (2006). *J Power Sources* 161:617–622.
213. Tasaki K, Goldberg A, Lian J-J, *et al.* (2009). *J Electrochem Soc* 156:A1019.
214. Zhang X, Liu K, Zhang S, *et al.* (2020). *J Power Sources* 458:228040.
215. Zhao Y, Sun T, Yin Q, *et al.* (2019). *J Mater Chem A* 7:15371–15377.
216. Rahman MM, Rani RA, Sadek AZ, *et al.* (2013). *J Mater Chem A* 1:11019–11025.
217. Ding Y, Yang Y, Shao H (2011). *Electrochim Acta* 56:9433–9438.
218. Ni S, Lv X, Li T, *et al.* (2013). *J Mater Chem A* 1:1544–1547.
219. Zhu X, Zhong Y, Zhai H, *et al.* (2014). *Electrochim Acta* 132:364–369.
220. Zhang S, Ren S, Han D, *et al.* (2019). *J Power Sources* 438:227007.
221. Zhou J, Li J, Liu K, *et al.* (2014). *J Mater Chem A* 2:20706–20713.
222. Luo XF, Yang CH, Peng YY, *et al.* (2015). *J Mater Chem A* 3:10320–10326.
223. Brezesinski T, Wang J, Tolbert SH, Dunn B (2010). *Nat Mater* 9:146–151.
224. Chao D, Zhu C, Yang P, *et al.* (2016). *Nat Commun* 7:1–8.
225. Pramanik A, Glass C, Maiti S, Glass C (2015). *Sci. Lett.* 4:104.
226. Soto FA, Ma Y, Martinez De La Hoz JM, *et al.* (2015). *Chem Mater* 27:7990–8000.
227. Ko S, Yamada Y, Yamada A (2021). *Joule* 5:998–1009.
228. Li A, Qian B, Zhong M, *et al.* (2019). *Mater Chem Front* 3:1398–1405.
229. Meng YF, Liang HJ, Zhao C De, *et al.* (2022). *J Energy Chem* 64:166–171.
230. Cardinale AM, Carbone C, Consani S, *et al.* (2020). *Crystals* 10(6):443.
231. Soltani R, Shahvar A, Dinari M, Saraji M (2018). *Ultrasonics Sonochemistry* 40(3):395-401.
232. Pathak AK, Mukherjee T, Maity DK (2008). *J Phys Chem A* 112:3399–3408.
233. Atif M, Bongiovanni R, Giorcelli M, *et al.* (2013). *Appl Surf Sci* 286:142–148.
234. Briggs D (2005). *Handb Adhes Second Ed* 621–622.
235. Gireaud L, Grugeon S, Laruelle S, *et al.* (2005). *J Electrochem Soc* 152:A850.
236. Philippe B, Dedryvère R, Allouche J, *et al.* (2012). *Chem Mater* 24:1107–1115.
237. Zhang H, Shen C, Huang Y, Liu Z (2021). *Appl Surf Sci* 537:147983.
238. Xu K, Zhuang G V., Allen JL, *et al.* (2006). *J Phys Chem B* 110:7708–7719.
239. Lang SY, Shen ZZ, Hu XC, *et al.* (2020). *Nano Energy* 75:104967.
240. May R, Fritzsche KJ, Livitz D, *et al.* (2021). *ACS Energy Lett* 6:1162–1169.
241. Dedryvère R, Leroy S, Martinez H, *et al.* (2006). *J Phys Chem B* 110:12986–12992.
242. Zhang H, Zhou L, Du X, *et al.* (2022). *Carbon Energy* 1–14.

## References

243. Hayashi Y, Yamada S, Ishikawa T, *et al.* (2020). *J Electrochem Soc* 167:020542.
244. Hou LP, Yao N, Xie J, *et al.* (2022). *Angew Chemie - Int Ed* 61:e202201406.
245. Chen Y, Jing C, Zhang X, *et al.* (2019). *J Colloid Interface Sci* 548:100–109.
246. Kalambate PK, Dar R a., Karna SP, Srivastava AK (2015). *J Power Sources* 276:262–270.
247. Kurzweil P (2020). In: *Angewandte Elektrochemie*, 1st ed. Springer Vieweg Wiesbaden, pp 5–31.
248. Li X, Fortunato M, Cardinale AM, *et al.* (2022). *J Solid State Electrochem* 26:49–61.
249. Abdolmohammad-Zadeh H, Tavarid K, Talleb Z (2012). *Sci World J* 2012:2356-6140.
250. Meng H, Yuan L, Gao J, *et al.* (2017). *RSC Adv* 7:10407–10414.
251. Thompson JM (2018). Jenny Stanford Publishing, Milton. ISBN 9781351206037.
252. Raki L, Beaudoin JJ, Mitchell L (2004). *Cem Concr Res* 34:1717–1724.
253. Wu Y, Xu J, Mei Y (2022). *J Wuhan Univ Technol Mater Sci Ed* 37:399–409.
254. Thomas N, Pradeep Kumar G, Rajamathi M (2009). *J Solid State Chem* 182:592–596.
255. Artyushkova K (2020). *J Vac Sci Technol A* 38:031002.
256. Bodenes L, Dedryvère R, Martinez H, *et al.* (2012). *J Electrochem Soc* 159:A1739–A1746.
257. Militello MC, Gaarenstroom SW (1999). *Surf Sci Spectra* 6:141–145.
258. Leanza D, Vaz C a. F, Novák P, El Kazzi M (2021). *Helv Chim Acta* 104:e2000183.
259. Lang J, Long Y, Qu J, *et al.* (2019). *Energy Storage Mater* 16:85–90.

## 10 Appendix

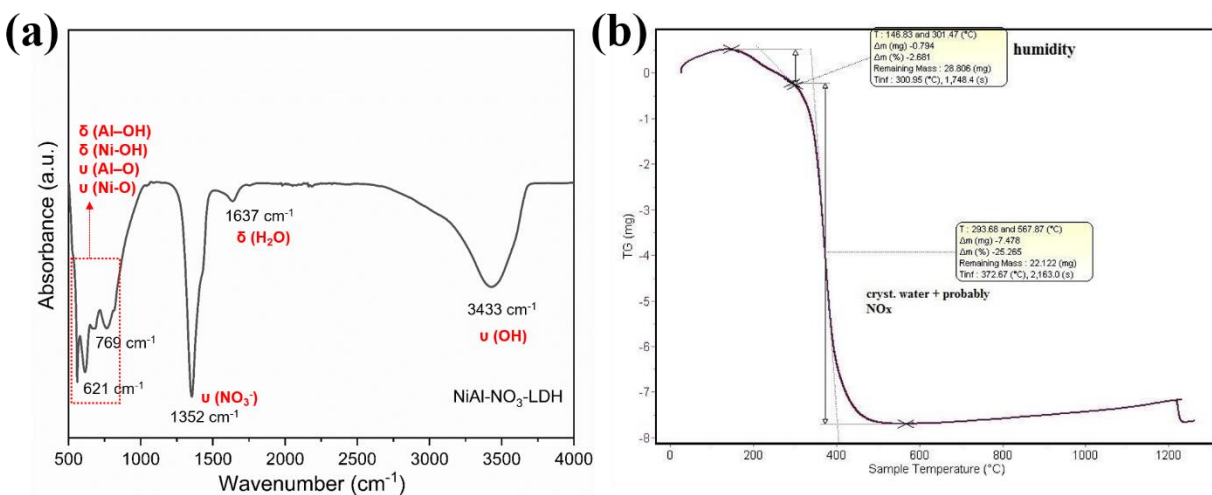


**Figure A 1.** a) FT IR spectra, and b) the thermogravimetric curve of NiAl LDH with NO<sub>3</sub><sup>-</sup> as the interlayer.

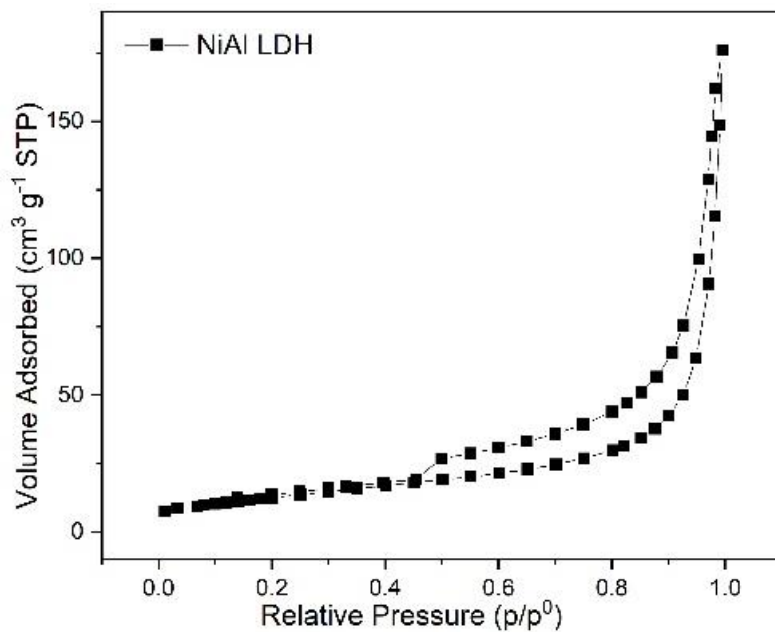


**Figure A 2.** Nitrogen adsorption and desorption isotherms of NiAl LDH.

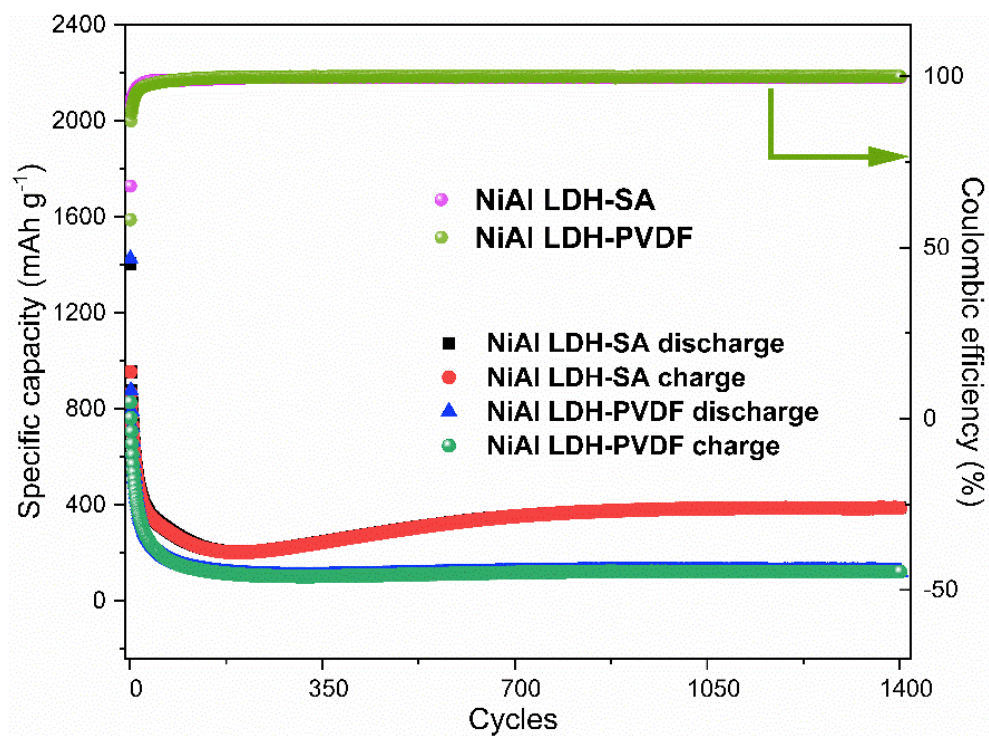


**Figure A 3.** Long cycling performance of NiAl LDH electrode with SA and PVDF binders at a potential window of 0.01–3.0 V (vs. Li<sup>+</sup>/Li) at a current density of 1.0 A g<sup>-1</sup>.

**Table A 1.** Binding energies (BE) and atomic concentrations (at%) of the different chemical environments identified by XPS at the surface of the NiAl LDH-PVDF electrode cycled for the full cycle (only P2p<sub>3/2</sub> binding energies are specified).

Orbital	Active material (NiAl LDH)		Discharge to 0.59V		Discharge to 0.22V		Full cycle		Assignments
	BE(eV)	at%	BE (eV)	at%	BE (eV)	at%	BE (eV)	at%	
Li 1s			55.4	24.7	55.6	35.8	55.7	32.0	Lithiated species
Ni 3s	114.1	9.7	nd	nd	nd	nd	nd	nd	Ni (NiAl LDH)
Al 3s	119.7	12.5	nd	nd	nd	nd	nd	nd	Al (NiAl LDH)
P 2p			133.6	0.7	133.7	1.1	133.6	0.9	P-O <sub>x</sub>
			136.7	0.2	137.0	0.2	136.3	0.2	LiPF <sub>6</sub>
C 1s			283.4	6.6	283.5	2.5	283.4	4.3	Carbon black
	285	10.1	284.9	10.5	285.0	7.3	284.9	8.5	C-C/C-H
			286.1	2.3	286.1	1.7	286.1	1.5	CF <sub>2</sub> -CH <sub>2</sub> (PVDF)
	286.4	1.5	286.8	4.4	286.8	2.7	286.7	4.3	C-O-C/ROLi
	288.8	2.2	288.7	1.5	288.3	1.0	288.6	1.1	O-C=O
			289.9	5.3	289.7	1.0	290.0	1.7	Li <sub>2</sub> CO <sub>3</sub>
			290.7	2.3	290.7	1.7	290.7	1.5	CF <sub>2</sub> -CH <sub>2</sub> (PVDF)
		291.8	0.4	292.4	0.1	291.8	0.3	CF <sub>2</sub> -CF <sub>2</sub> (PVDF)	
N 1s	407.1	2.9							
O 1s			528.2	0.5	528.2	0.1	528.4	0.2	Li <sub>2</sub> O
	530	2.1	530.7	6.2	530.7	3.7	530.8	5.4	ROLi/LiOH
			531.7	18.7	531.7	6.1	531.7	6.2	O-C/Li <sub>2</sub> CO <sub>3</sub>
	532	58.4	533.1	4.5	533.4	2.3	533.2	3.1	O (NiAl LDH) O-C-O-P O (water crystal)
534.6	0.6								
F 1s			684.8	5.1	685.2	28.2	685.0	22.9	Li-F
			687.7	5.5	687.6	4.7	687.7	5.6	F (PVDF, LiPF <sub>6</sub> )

**Table A 2.** Binding energies (BE) and atomic concentrations (at%) of the different chemical environments identified by XPS at the surface of the NiAl LDH-SA electrode cycled until the full cycle (only P2p<sub>3/2</sub> binding energies are specified).

Orbital	Active material (NiAl LDH)		Discharge to 0.65V		Discharge to 0.34V		Full cycle		Assignments
	BE(eV)	at%	BE (eV)	at%	BE (eV)	at%	BE (eV)	at%	
Li 1s			55.1	33.9	55.4	33.7	55.2	37.7	Lithiated species
Ni 3s	114.1	9.7	nd	nd	nd	nd	nd	nd	Ni (NiAl LDH)
Al 3s	119.7	12.5	nd	nd	nd	nd	nd	nd	Al (NiAl LDH)
P 2p	285	10.1	283.0	4.1	283.1	2.6	283.2	2.2	Carbon black C-C/C-H
	286.4 288.8	1.5 2.2	133.2 137.1	1.5 0.1	133.4 136.5	1.1 0.1	133.4 137.6	0.8 0.1	
C 1s			286.3	4.7	286.7	3.7	286.5	3.9	C-O-C/ROLi O-C=O Li <sub>2</sub> CO <sub>3</sub>
			287.9 290.0	1.8 4.1	288.5 290.1	1.0 5.0	288.5 290.1	0.8 2.4	
N 1s	407.1	2.9							
			528.4	3.8	528.4	1.7	528.5	2.8	Li <sub>2</sub> O
O 1s	530	2.1	530.8	11.2	530.8	11.1	530.8	9.7	ROLi/LiOH
	532	58.4	531.7	15.4	531.8	17.0	531.8	10.0	O=C/Li <sub>2</sub> CO <sub>3</sub>
	534.6	0.6	533.5	3.8	533.2	3.0	533.0	1.8	O (NiAl LDH)
			535.3	-	535.5	-	535.5	-	O (water crystal) Na KLL (SA binder)
F 1s			684.9	5.5	684.9	5.9	685.2	14.2	Li-F
			687.2	1.6	687.6	0.7	687.4	0.5	F (LiPF <sub>6</sub> )
Na 1s			1071.8	0.2	1071.6	0.1	Nd	nd	Na (SA binder)

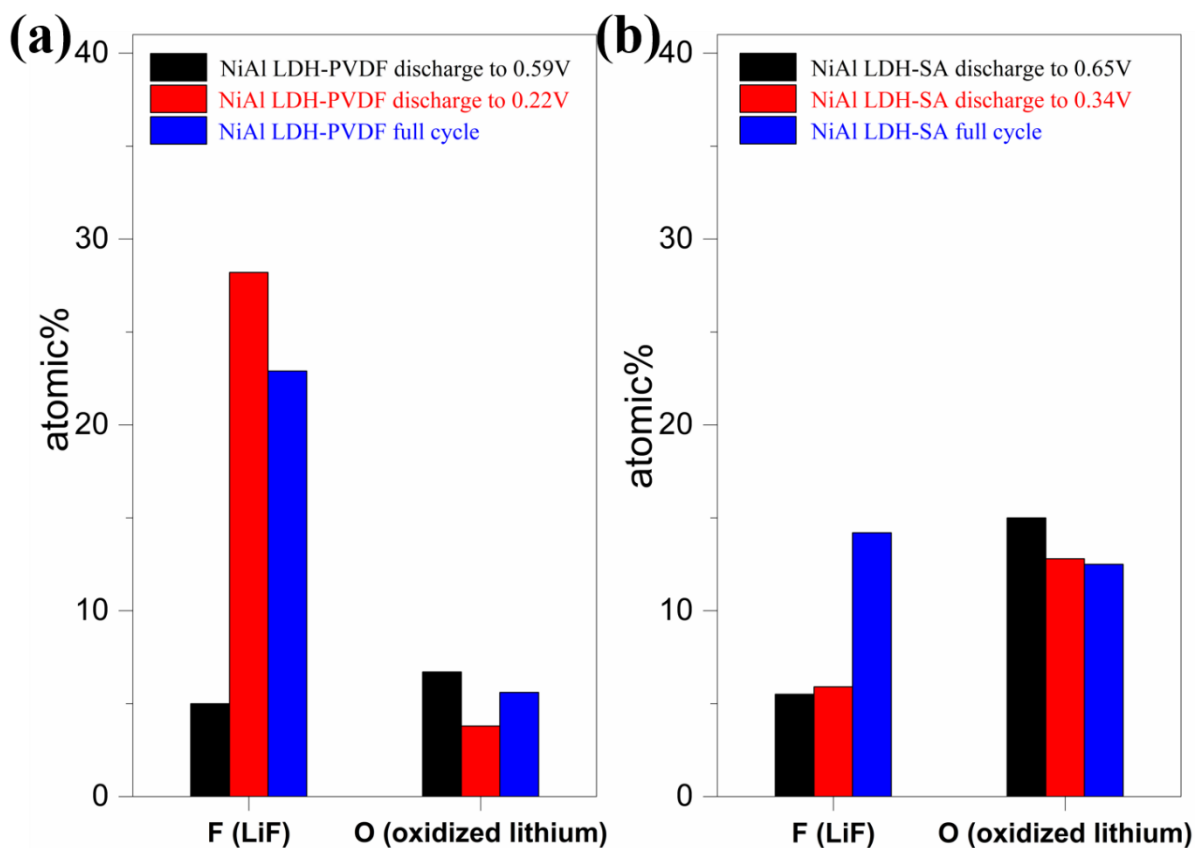


**Figure A 4.** Amount variation of fluorine from LiF and oxygen from oxidized lithium (ROLi, LiOH and Li<sub>2</sub>O) species on the electrode with a) PVDF binder, and b) SA binder.

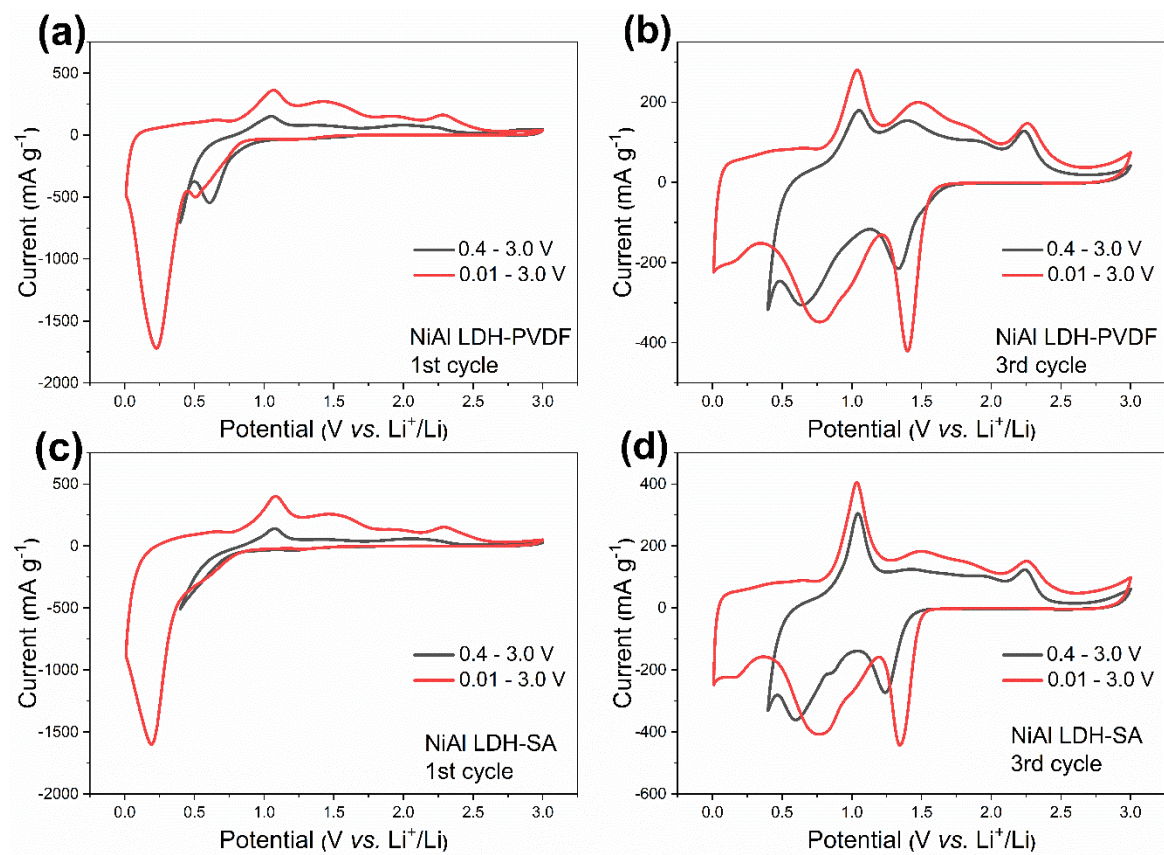


**Figure A 5.** Comparison of two potential ranges for NiAl LDH-SA and NiAl LDH-PVDF electrodes.

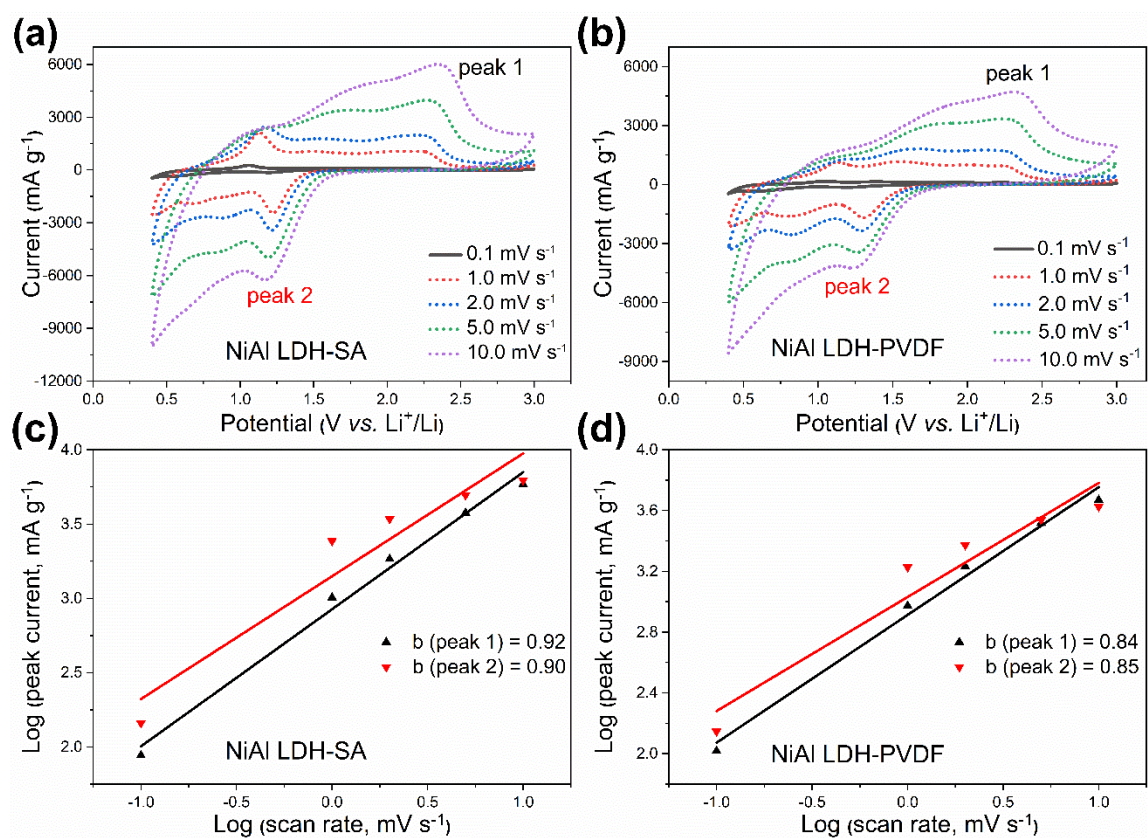


**Figure A 6.** Kinetic investigation of the NiAl LDH electrode at a potential window of 0.4–3.0 V (vs. Li<sup>+</sup>/Li). CV curves at various scan rates of that a) with SA binder, and b) with PVDF binder; *b*-value determined by the slopes of the logarithm relationship of scan rates and peak current for the electrode c) with SA binder, and d) with PVDF binder.

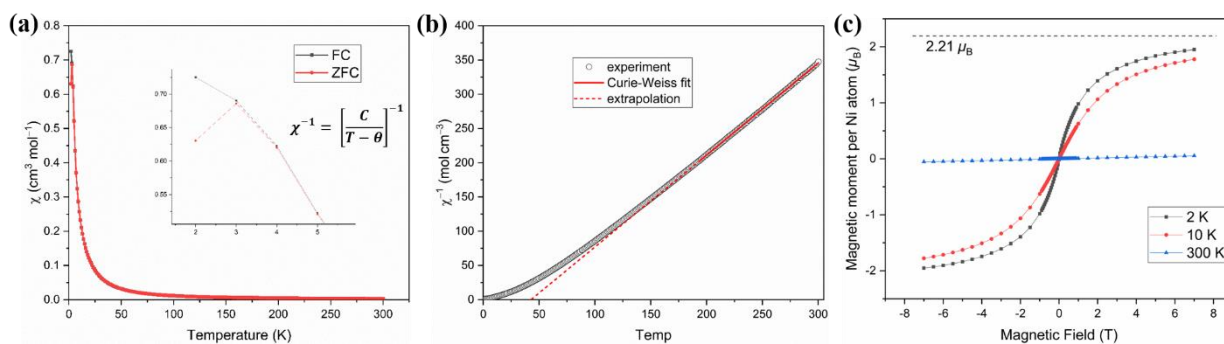


**Figure A 7.** Magnetic measurement. a). ZFC/FC susceptibility vs. temperature curves for  $\text{Ni}_{0.66}\text{Al}_{0.33}(\text{OH})_2(\text{NO}_3)_{0.33} \cdot 0.16 \text{H}_2\text{O}$  obtained at a field of 500 Oe, and the inserted fit: with the Curie constant  $C$ , temperature  $T$  and Curie-Weiss temperature. b). Inverse susceptibility vs. temperature curve as derived from the FC susceptibility curve. The solid line shows the Curie-Weiss fit from 200 to 300 K and its extrapolation (dashed line). c). Magnetic moment vs. magnetic field for various temperatures. The saturation magnetization as predicted from the Curie-Weiss fit is almost reached at 2 K and 7 T.

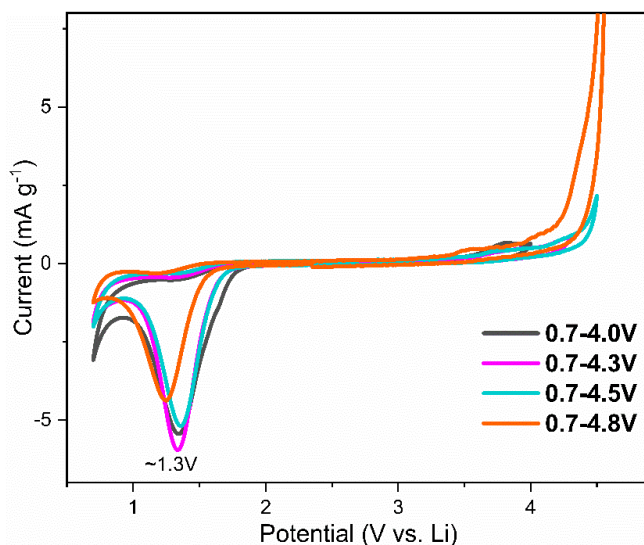


**Figure A 8.** Electrochemical stability of the  $\text{LiTFSI}/\text{LiNO}_3$  electrolyte on CV curves at  $1.0 \text{mV s}^{-1}$  at different potential windows (vs. Li).

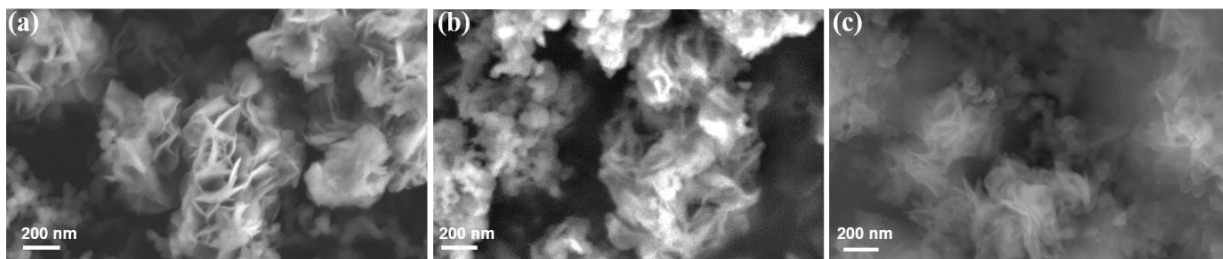


**Figure A 9.** SEM images of NiAl LDH electrodes in LiTFSI/LiNO<sub>3</sub> electrolyte: a) pristine electrode, b) discharge to 0.7 V and, c) charge to 4.0 V.

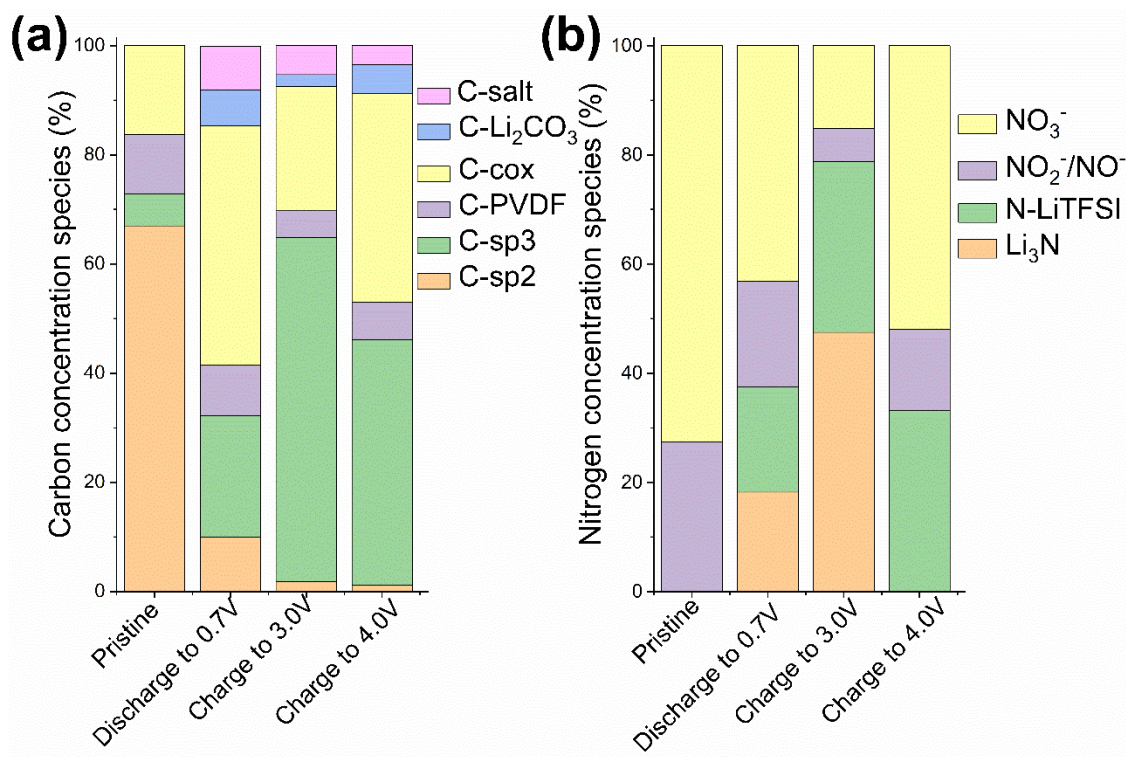


**Figure A 10** The concentration of compositions during the discharge-charge process of the NiAl LDH electrodes: a) carbon, b) nitrogen.

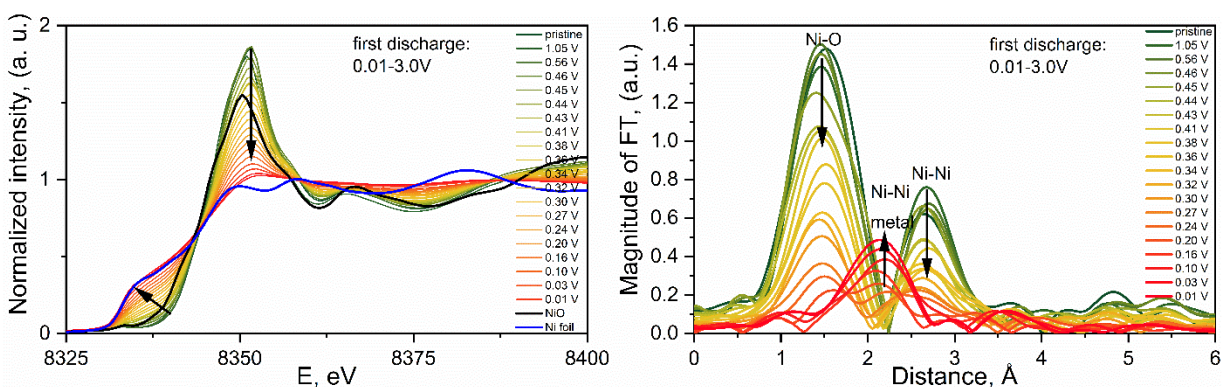


**Figure A 11** *In-situ* normalized XANES spectra at Ni K-edge and Fourier transform of the recorded EXAFS spectra of the discharge process of NiAl LDH on LP30 at a potential window of 0.01-3.0 V (vs.  $\text{Li}^+/\text{Li}$ ).

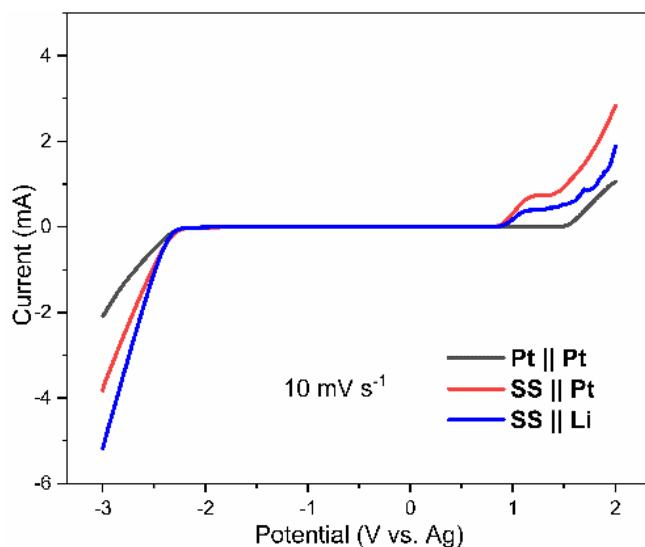


**Figure A 12.** The electrochemical stability window of different cell configurations based on Ag QRE in glass cell.

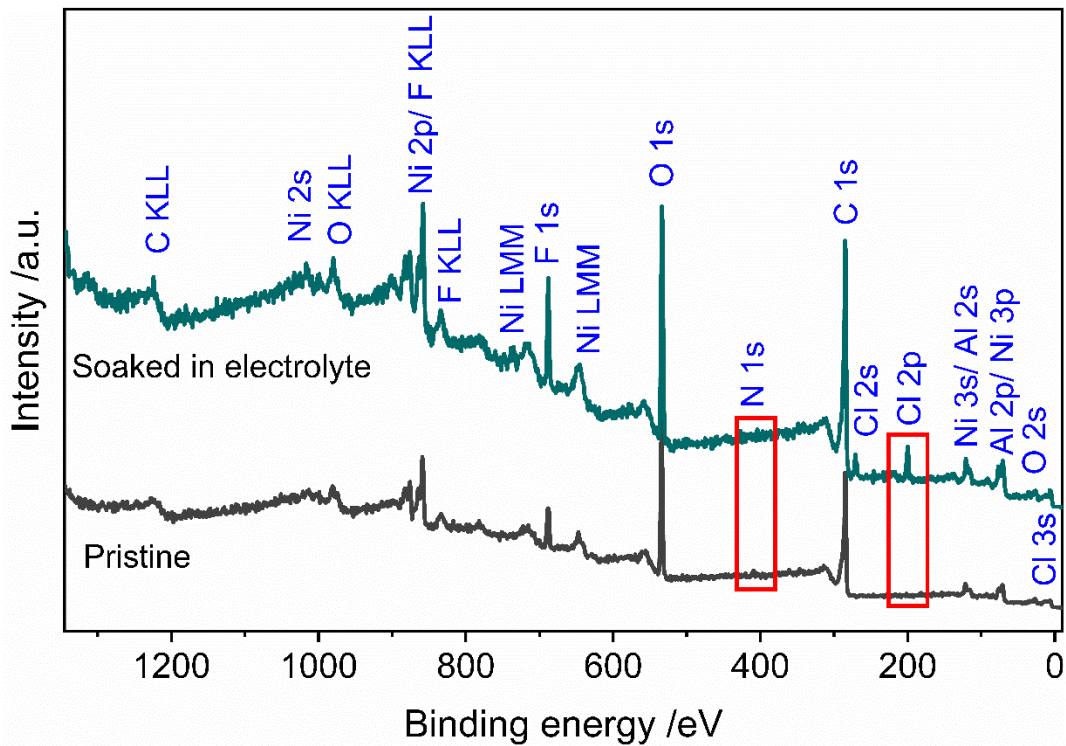


**Figure A 13.** XPS survey of the NiAl LDH electrode and the electrode soaked in Bpy<sub>14</sub>Cl/PC electrolyte.